UNIVERSIDAD DE ANTIOQUIA

STUDIES ON CHABAZITE ZEOLITES FOR THE SELECTIVE CATALYTIC REDUCTION (SCR) OF NOx

JUAN MIGUEL GONZÁLEZ MARTÍNEZ

Universidad de Antioquia
Facultad de Ingeniería, Departamento de Ingeniería Química
Medellín, Colombia
2020

STUDIES ON CHABAZITE ZEOLITES FOR THE SELECTIVE CATALYTIC REDUCTION (SCR) OF NOx

By

JUAN MIGUEL GONZÁLEZ MARTÍNEZ

Research work presented in partial fulfillment of the requirements for the PhD in Chemical Engineering degree

Advisor:

AÍDA LUZ VILLA HOLGUÍN
Ph.D. Biological Sciences, Universite Catholique De Louvain
Full professor at Universidad de Antioquia

Co-advisor:

FABIO H. RIBEIRO
Ph.D. Chemical Engineering, Stanford University
R. Norris and Eleanor Shreve Professor of Chemical Engineering at Purdue University

Universidad de Antioquia
Facultad de Ingeniería, Departamento de Ingeniería Química
Medellín, Colombia
2020

To Mom and Dad

Abstract

Selective catalytic reduction (SCR) over Cu-SSZ-13 catalyst is one of the most promising methods to withdraw NOx emissions from diesel engines. The process consists in reducing NOx, at the highly oxidative ambient presented in diesel exhaust gases, to produce harmless N_2 and H_2O. This occurs in the presence of a reducing gas, usually ammonia, and the catalyst. Even though the use of Cu-SSZ-13 catalyst for SCR is a well-studied process, being identified its active sites ($[CuOH]^{1+}$ and Cu^{2+}) and having a widely accepted reaction mechanism for both sites; several aspects might be studied to improve SCR performance.

In this work, we studied if the continuous exposure of Cu-SSZ-13 catalyst to sulfur species, presented as impurities in diesel fuels, may have a poisoning effect on its active sites, therefore decreasing its activity for SCR reaction. Cu-SSZ-13 samples with isolated $[CuOH]^{1+}$ and Cu^{2+} sites were saturated with SO_2, then used to perform a kinetic study, *in-situ* UV-vis characterizations and *operando* XAS characterizations. It was observed by kinetics experiments that sulfur caused a reduction in NO consumption rate in both Cu sites, evidencing a poisoning effect. Only $[CuOH]^{1+}$ site presented changes in the activation energy, therefore in this site a change in reaction mechanism was presented. *in-situ* UV-Vis-NIR characterizations and *operando* X-ray absorption characterizations where used to analyze how Cu sites where affected by sulfur at reaction conditions, information that was used to propose a reaction mechanism for each site.

In addition, we studied how high temperatures may affect the activity of $[CuOH]^{1+}$ and Cu^{2+} sites for SCR, and if the presence of iron in the catalyst may improve the catalyst performance at such conditions. SCR catalysts can be exposed to periods of high temperatures during the regeneration of particulate matter filters, located prior to SCR unit in diesels exhaust gas treatment systems, therefore it is important to know if Cu-SSZ-13 sites can withstand such temperature increases. SCR, NH_3 oxidation and NO oxidation reactions were tested over Cu-SSZ-13 and Fe-Cu-SSZ-13 catalysts at 200 to 600°C. It was observed that when the temperature was higher than 350°C during SCR experiments, NO consumption rates decreased in Cu-SSZ-13 catalysts with higher intensity in a sample with mostly $[CuOH]^{1+}$ sites. In opposite, Fe-Cu-SSZ-13 samples maintained higher NO consumption rates. However NH_3 oxidation and NO oxidation reactions demonstrated that higher NO rates in Fe-Cu-SSZ-13 samples were not caused by NO reduction to N_2 but the result of its oxidation to other nitrogen oxides.

Finally, it was studied the synthesis of SAPO-34, a silicoaluminophosphate with the same chabazite structure of SSZ-13 but potentially with a lower production cost. The main challenge during the synthesis of SAPO-34 consists in obtaining the highest availability of Brönsted acid sites to be exchanged by the active species (usually Cu). This can be affected, among several factors, by the selection of the structure directing agent and by changing the composition of Si, Al or P during the synthesis. Several silicon composition in the initial synthesis gel along with the use of several structure directing agents were evaluated. The effect of these changes on the Brönsted acidity of the final SAPO-34 materials was tested by NH_3-TPD characterizations, and textural properties were studied by SEM and XRD charac-

terizations. Comparing the materials synthesized in this work, a silicon : morpholine molar ratio of 0.6 mol allowed to obtain SAPO-34 without other structures and higher Brönsted acidity.

Contents

List of Figures

List of Tables

List of Symbols

$\dot{n}_{NO}$	Mols of NO consumed per second	$mol \cdot s^{-1}$
$\dot{V}_{total}$	Total flow rate	$mL \cdot min^{-1}$
λ	Wavelength of the x-rays	Å
μ_{ν}	Linear absorption coefficient	cm^{-1}
ν	Frequency	Hz
ω	Wavenumber	cm^{-1}
τ	Crystallite size	Å
θ	Diffraction angle	°
A_0	Pre-exponential factor	$kJ \cdot mol^{1-} \cdot s^{-1}$
C_{NO}	Molar concentration of NO	$mol \cdot L^{-1}$
d_{hkl}	Lattice spacing	nm
$E_{a,app}$	Apparent activation energy	$kJ \cdot mol^{1-} \cdot s^{-1}$
$E_{binding}$	Binding energy	kJ
E_F	Fermi energy	kJ
k_{eff}	Kinetic constant	$mol \cdot mL^{1-} \cdot s^{-1}$
P	Pressure	atm
R	Gas constant	$8.314\ J \cdot mol^{1-} \cdot K^{-1}$
R_{∞}	Reflectance	%
R_{SCR}	SCR reaction rate	$mol \cdot gcat^{-1} \cdot s^{-1}$
Rate	Rate of consumption	$mol \cdot gcat^{-1} \cdot s^{-1}$
S_r	Sum of integral peak intensities for the reference	Dimensionless

S_x	Sum of integral peak intensities for the sample	Dimensionless
T	Temperature	K
a	Absorption constant	$mol^{-1} \cdot cm^{-1}$
b	Thickness of the absorbing layer	cm
c	Concentration of the analyte atoms	mol
h	Plank constant	$6.62607004 \times 10^{-34}$ $m^2 \cdot kg \cdot s$
I	Intensity	a.u.
K	Apparent absorption	Dimensionless
k	Dimensionless shape factor	Dimensionless
L	Full width at half maximum (FWHM)	Dimensionless
S	Apparent scattering coefficient	Dimensionless
T	Transmitance	a.u.
t	Time	s

Chapter 1

Introduction

1.1 Selective Catalytic reduction of NOx

1.1.1 NOx from diesel engines and methods for its abatement

Diesel engines are widely used for driving power generators and for mobile applications in cars, light and heavy commercial vehicles, railway locomotives, ships, construction and agricultural equipment. Therefore, they are important contributors to environmental pollution worldwide, which will increase because of the large rising expected in vehicle population [1, 2]. Emissions from diesel engines are complex mixtures that includes carbon oxides, nitrogen oxides (NOx), sulfur dioxide, particulate matter and a broad range of aliphatic and aromatic hydrocarbons, Figure 1.1 [3, 4, 5].
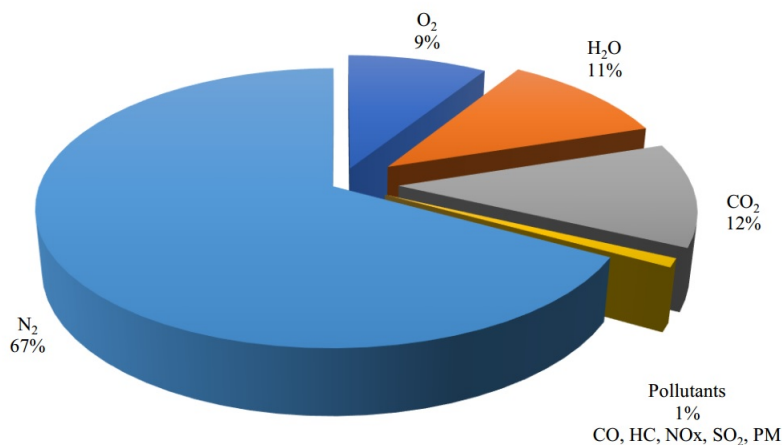
Figure 1.1: Diesel gas composition [5]

NOx consists in a mixture of nitrogen oxides that includes nitrous oxide (N_2O), nitric oxide (NO), nitrogen dioxide (NO_2), nitrogen trioxide (N_2O_3) and nitrogen pentoxide (N_2O_5)

[2]. These compounds are produced mainly during the combustion of fossil fuels and are serious air pollutants. Typically, NOx gas produced during the combustion of fuels consists in 95% NO and 5% NO_2. NO, a colorless gas, is a precursor of NO_2 and is an active compound in photochemical reactions that produce smog. NO_2 is a precursor to nitric acid, HNO_3, in the atmosphere and is a major contributor to acid rain [6, 7].

Methods for abating NOx emission can be classified into three main categories: pre-combustion control, combustion modification and post-combustion control. Pre-combustion control consists in reducing the nitrogen content in the fuel. Combustion modification implies changes in the operational conditions to avoid N_2 oxidation. Both pre-combustion and combustion controls are helpful, but can only achieve a modest reduction in NOx emissions, usually less than 50%. For applications required to achieve higher NOx reductions, it is necessary to use post-combustion control, which is able to withdraw NOx from exhaust gases and are able to withdraw near 100% of it [8].

The most commonly used post-combustion NOx abating technologies are selective non-catalytic reduction (SNCR) and selective catalytic reduction (SCR). The aim of both technologies is to reduce NOx in the flue gas to harmless N_2 and H_2O, by injecting a reducing gas in the NOx containing stream, usually ammonia and the use of a catalyst for the case of SCR. SNCR reactors are typically operated at 870 - 980°C, making this process infeasible for mobile applications, while SCR takes places at lower temperatures (200 - 400°C), facilitating its use in diesel exhaust systems [8].

1.1.2 The SCR reaction

During selective catalytic reduction (SCR), NOx gases are reduced with ammonia in the presence of oxygen to form harmless nitrogen and water, Equation (1.1). This process involves the injection of ammonia into the NOx containing gas flow, which then, passes through an heterogeneous catalyst [9, 10].

$$4NO + 4NH_3 + O_2 \rightarrow 4N_2 + 6H_2O \tag{1.1}$$
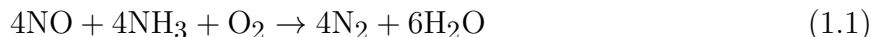
Standard SCR involves a 1:1 stoichiometry for NH_3 and NO and the consumption of some oxygen. In the absence of oxygen, Equation (1.2), the NO reduction has a much slower rate than reaction in Equation (1.1), therefore is not relevant in lean combustion gases, typically found on diesel engines exhausts [9].

$$6NO + 4NH_3 \rightarrow 5N_2 + 6H_2O \tag{1.2}$$

On the other hand, The so-called "fast SCR" occurs when equimolar amounts of NO and NO_2 are presented, Equation (1.3). This reaction is much faster than the standard SCR reaction, Equation (1.1) [11, 12]. Additionally, SCR of pure NO_2, Equation (1.4), is slower than Equations (1.2) and (1.3) [9].

$$2NO_2 + 2NO + 4NH_3 \rightarrow 4N_2 + 6H_2O \tag{1.3}$$

$$6NO_2 + 8NH_3 \rightarrow 7N_2 + 12H_2O \tag{1.4}$$
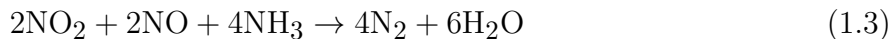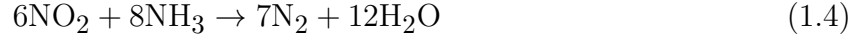
High temperatures affect standard SCR reaction by the occurrence of side reactions. At temperatures higher than 400°C, nitrous oxide (N_2O) is formed, Equation (1.5) . Also, at temperatures higher than 500 °C the oxidation of NH_3 to NO takes place, thus limiting the maximum NOx conversion, Equation (1.6) [9, 13].

$$4NO + 4NH_3 + 3O_2 \rightarrow 4N_2O + 6H_2O \tag{1.5}$$

$$4NH_3 + 5O_2 \rightarrow 4NO + 6H_2O \tag{1.6}$$
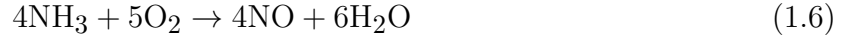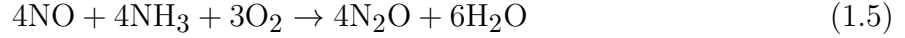
Low temperatures can also disturb SCR reaction. At temperatures below 200°C in the NOx feed containing NO_2, solid ammonium nitrate (NH_4NO_3) is formed according to Equation (1.7), leading to flow blockages [9, 11].

$$2NO_2 + 2NH_3 \rightarrow NH_4NO_3 + N_2 + H_2O \tag{1.7}$$
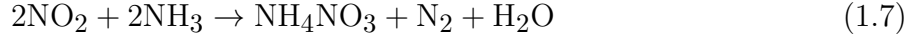
1.1.3 Characteristics of chabazite (CHA) type zeolites

1.1.3.1 ABC-6 family of zeolites

Zeolites are natural or synthetic silicoaluminates, characterized by a three-dimensional and regular microporous crystal structure and formed by basic building units (BBU) of interconnected tetrahedrons (TO_4, T = Si, Al, ...). BBU are linked together, forming composite building units (CBUs), such as rings, cavities and channels that can be occupied by ions, water and other molecules. The topology of zeolites framework defines a structure type, or zeotipe, that are symbolized by a group of three letters [14, 15].
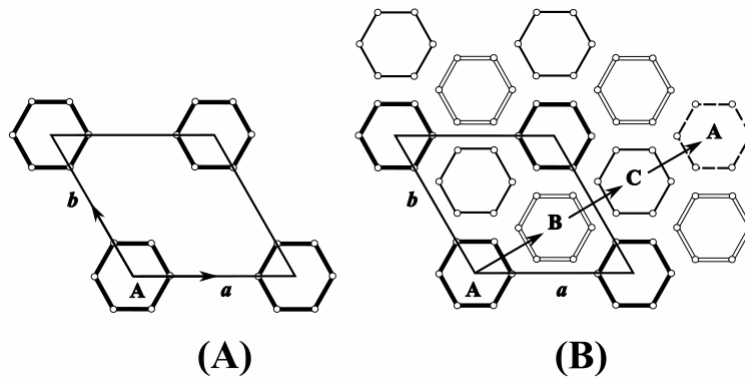
Figure 1.2: Arrangement of single 6-member rings in the ab-plane of a hexagonal unit cell. In (A) a single layer, and in (B) a projection of a 3-layer stacking sequence ABC is shown [16].

3

Zeolite frameworks can be classified according to the composite building units (CBUs) of basic building units (BBUs) that form them. We are particularly interested in the ABC-6 family of zeolites, that corresponds to a large group of frameworks, formed by staking layers of 6-member rings in three different ways. In Figure 1.2, position A does not have any shift, in position B there is a shift of 2/3a or 1/3b, and position C a shift of 1/3a or 2/3b. Different combinations of the A, B and C layers generate infinite possibilities of stacking sequences [14, 16].

1.1.3.2 CHA framework

CHA framework was named after the mineral chabazite, $NaAlSi_2O_6.H_2O$, first described by von Born and Bosc d'Antic [17]. CHA is a member of the ABC-6 family and has as an AABBCC stacking sequence that forms a cavity with eight-membered ring (8MR) pores. Figure 1.3 shows the CHA structure of SSZ-13, a synthetic zeolite first patented by Zones [18].
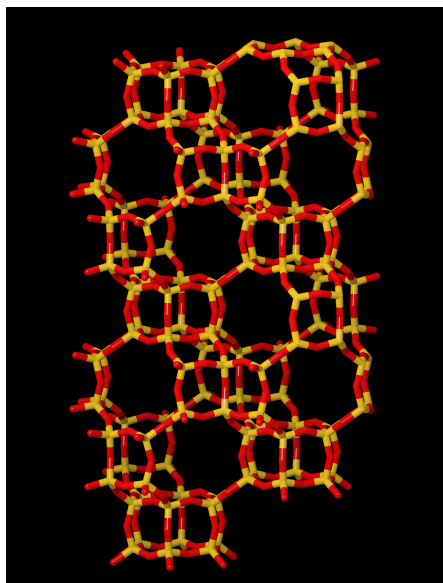
Figure 1.3: CHA structure showing silicon atoms (yellow sticks) and oxygen atoms (red sticks) [16].

CHA framework is not limited to zeolites. Figure 1.4 shows SAPO-34, a silicoaluminophosphate molecular sieve that also presents CHA structure. SAPOs framework are formed by PO_4, AlO_4 and SiO_4 BBUs and have similar catalytic activity to their analogous zeolites [19, 20].
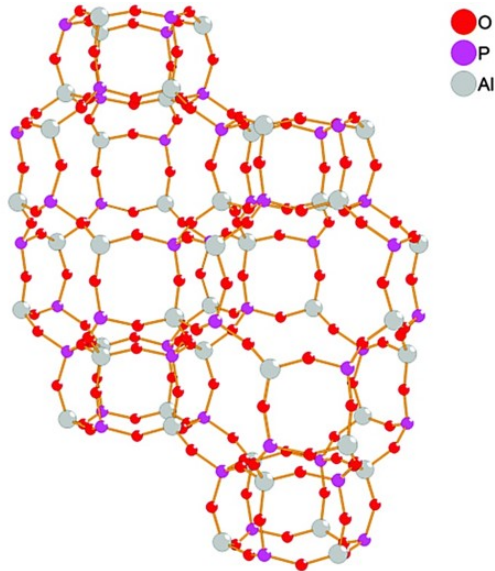
Figure 1.4: SAPO-34 structure [21].

1.1.4 Cu-chabazite as catalysts for SCR reaction

The use of SCR to control NOx emissions started in Japan in the 1970s with the introduction of vanadia-titania catalytic system for NOx treatment in coal plants [22]. Those SCR systems were transferred to mobile applications in Europe in the 1980s and were able to achieve NOx conversions in the 90 - 95% range [23]. Nevertheless, concerns about the emission of volatile toxic vanadia species at temperatures above 650°C forced a ban on their use [24].

Metal-zeolite catalysts began to be used for SCR in 1986, with the work of Iwamoto *et al* [25] with Cu-ZSM-5, and it has continued through the last three decades [22]. One of the most studied aspect of metal-zeolites for SCR has been their durability at practical vehicle applications, since zeolites suffer structure damage by dealumination at hydrothermal conditions, or the presence of water at high temperatures [26]. In 2000s small-pore zeolites, as SSZ-13, gained attention due to its higher resistance to those conditions [27]. Another advantage of small-pore zeolites is that they have reduced diffusion of bulky uncombusted hydrocarbons that can degrade the zeolite internal structure by their highly exothermic combustion [22].

Another important aspect when selecting a catalyst for SCR is the working temperature is relevant when selecting the active transition metal. Low temperature is desired to avoid the need of heating process. So far, Cu seems to be the optimal since Cu-CHA catalyst can obtain near 100% NOx conversion at 200°C [20]. However, it is also desired that the catalyst resist high temperatures to resists periodical regeneration of upstream soot filters in diesel gas treatment systems. For this case, Fe-SSZ-13 have shown to maintain NOx conversion near 100% at 550°C [28, 29, 30].

In 2010 Cu-SAPO-14 became the first commercial SCR Cu-CHA catalyst to appear, thanks to its hydrothermal stability at temperatures up to $1000°C$ [20]. In recent years there is a tendency of preferring Cu-SSZ-13 over SAPO-34 since it has been observed that SAPO-34 undergoes deactivation by framework Si atoms rearrangement, to form charge neutral Si "islands", in the presence of liquid water [31, 32].

1.1.5 Brönsted acid sites in CHA and its role in SCR of NOx

1.1.5.1 BA in SSZ-13

Bönsted acidity (BA) is the most relevant property of a zeolite in terms of catalytic activity. It is generated when a framework Si^{4+} BBU is replaced by Al^{3+} during the synthesis. Since Al has a 3+ oxidation state, tetrahedrons formed by its bonding to four oxygen atoms will have a negative charge, that need to be balanced with a cation (H^{1+} in the case of BA) [33]. Consequently, there is a direct relationship between Al content and BA distribution in a zeolite.

Depending on its Si/Al ratio, a zeolite can have isolated $(Al - O(-Si - O)_x - Al, x \geq 3)$ or paired $(Al - O(-Si - O)_x - Al, x = 1, 2)$ BA. In SSZ-13 it has been observed that $Si/Al = 4.5$ will generate materials with mostly paired BA on its 6-member ring, and $Si/Al = 25$ will generate materials with mostly isolated BA on its 8-member ring [34]. These Si/Al ratios have been used to isolate the type of Cu species formed in Cu-SSZ-13 that are active for SCR, Cu^{2+} and $[CuOH]^{1+}$, since Cu^{2+} sites are exchanged in paired BA, and $[CuOH]^{1+}$ sites occur when Cu is exchanged in a isolated BA and charge balanced by an OH^{1-} anion [35].

1.1.5.2 BA in SAPO-34

BA in SAPO materials are generate by framework atoms substitution and charge compensation with H^{1+} cations, in a analogue way as in zeolites. But in this case, the charge unbalances that generate BA occur by the substitution of framework P or Al by Si. Since SAPOs have three different species (Si, Al and P), several substitution mechanisms can take place [19, 7, 36, 37]:

- Si for framework Al (SM1) and would lead to the formation of Si-O-P bridges, which are energetically unfavorable and have not been observed experimentally so far.

- Si for framework P(SM2), with a subsequent formation of a BA.

- Two Si for neighboring framework P and Al (SM3), causing the formation of neutral (and therefore catalytically inactive) silicon islands.

The presence of Cu^{2+} and $[CuOH]^{1+}$ sites, already seen in Cu-SSZ-13, have been identified in SAPO-34 samples [38, 39]. However, unlike Cu-SSZ-13, specific Si/(P+Al) ratios to obtain samples with isolated Cu^{2+} and $[CuOH]^{1+}$ (and therefore with only isolated or paired BA) have not been reported yet.

1.1.6 Reaction mechanism for SCR over Cu-SSZ-13
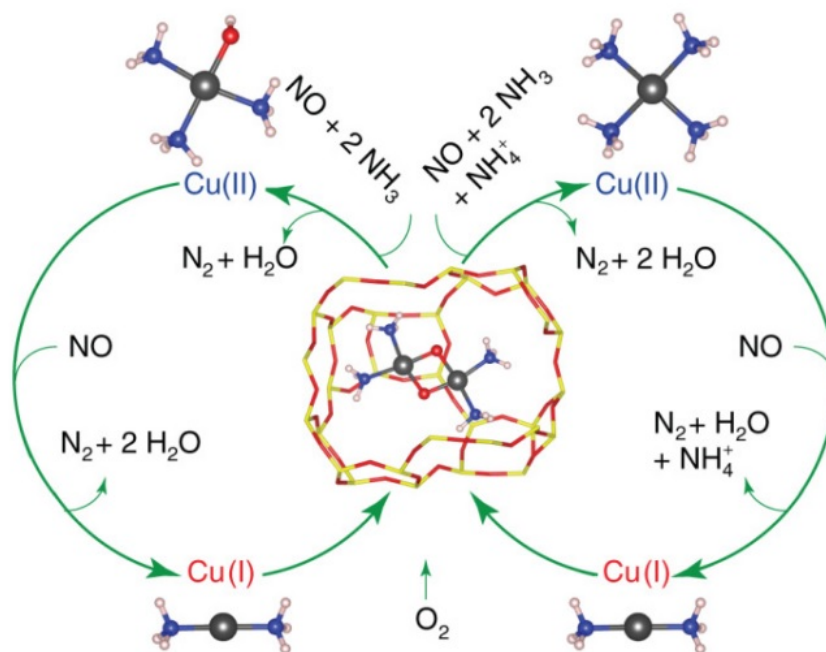
Figure 1.5: NH$_3$-SCR reaction mechanism [20]. Where the balls correspond to copper (black), nitrogen (blue), hydrogen (white) and oxygen (red) atoms

A reaction mechanism for SCR reaction over Cu-SSZ-13 was proposed for the range 150 - 250°C by Paolucci *et al* [40, 41, 42], Figure 1.5. Kinetic measurements along with *operando* and transient X-ray absorption characterizations and DFT calculations were carried out to provide information for this purpose, as follows:

- *Operando* X-ray absorption near edge (XANES) experiments performed on Cu-SSZ-13 samples during steady-state SCR were used to quantify the oxidation state of copper species. It was observed that site-isolated Cu^{2+} ions evolved in a mixture of Cu^{1+} and Cu^{2+}, evidencing a redox cycle mechanism [42]. Both reduction and oxidation half cycles were reported to form N$_2$ and water [43, 42].

- Density functional theory-based models were used to show that NH$_3$ displaces the other gases presented in SCR reaction and binds to Cu^{1+} and Cu^{2+} ions, forming two- and four-fold coordinated species, respectively [40, 41].

- Transient XANES characterizations were performed on Cu-CHA-15, Cu-CHA-20, and Cu-CHA-29 to identify the role of O$_2$ and Cu density in the oxidation SCR half-cycle. During the experiments, the active sites were reduced to Cu^{2+} using a flow of NO and NH$_3$. Then the samples were oxidized using flows of either O$_2$ or NO$_2$, while XANES spectra were collected. The quantification of Cu^{1+} fraction during transient experiments lead to the proposal of a pseudo-bimolecular reaction between

$Cu^{1+}(NH_3)_2$ ions and O_2 during the oxidation cycle, to form oxygen-bridged copper dimers. The formation of these dimers was later confirmed by DFT calculations [40].

- Exposure of samples to NO and NH_3 after the transient O_2 oxidation experiments, reduced all sites to Cu^{1+}, demonstrating that the redox cycle can be closed through sequential reactions [40, 42].

1.2 Thesis objectives

1.2.1 General objective

To identify the effect of reaction conditions, alternative active phases and different chabazite supports on the selective catalytic reduction of NOx over Cu-SSZ-13.

1.2.2 Specific objectives

- To study the effect of sulfur poisoning on Cu-SSZ-13 active sites during selective catalytic reduction of NOx with ammonia.

- To compare the catalytic activity of Fe-Cu-SSZ-13 and Cu-SSZ-13 for the selective catalytic reduction of NOx at high temperatures (200 - 600°C).

- To improve Brönsted acidity in SAPO-34 for its potential use as alternative chabazite catalyst support for the selective catalytic reduction on NOx.

1.3 Thesis overview

Even though the SCR reaction mechanism over Cu-SSZ-13 is now well understood [42, 41, 20, 40], contributions can be still made to enhance the performance of SCR catalysts. The main goal of this work is to improve SCR reaction over Cu-CHA catalysts by exploring several fields of the catalysis. In Chapter 2, kinetics experiments and *in-situ* characterizations were used to study the effect of the presence of sulfur in SCR mechanism over Cu-SSZ-13. In Chapter 3, a catalytic activity analysis was performed to identify if doping with Fe may improve the performance of Cu-SSZ-13 at temperatures were SCR with only Cu as active phase did not presented a good performance. In Chapter 4, a synthesis study was carried out to determine the conditions at which SAPO-34, a cheaper alternative molecular sieve for SSZ-13, would present higher Bronsted acidity as a way to improve its catalytic activity during SCR. A more specific description of this work is listed as follows:

Chapter 2. Kinetic and Spectroscopic study of Selective Catalytic Reduction of NOx on SO₂ exposed Cu-SSZ-13: One of the main interest about Cu-SSZ-13 catalyst is knowing the effect that diesel exhaust pollutants different from NOx have on its catalytic activity for SCR. Such is the case of sulfur oxides, SOx, which are presented in diesel fuels even with strict regulations nowadays. It has been reported that sulfur oxides

inhibits the ability of Cu-SSZ-13 in reducing NOx, however a deeper understanding of the specific effect of those compounds on copper active sites from Cu-SSZ-13 is still to be determined. In this chapter the effect of adsorbed SO_2 on Cu-SSZ-13 and its consequences for SCR of NOx are studied. For this, SSZ-13 zeolite was prepared via hydrothermal synthesis with Si/Al ratios of 4.5 and 25, to generate paired and isolated Brönsted active sites. Subsequently, copper was ion-exchanged into SSZ-13 using $Cu(NO_3)_2$ solutions, generating materials differentiated in the type of active site (Cu^{2+} or $[CuOH]^{1+}$ sites) depending on the Si/Al ratios obtained previously. Then, the catalysts were post-treated with SO_2 at 200 and 400°C, then characterized by AAS, XRD, SEM, ICP-OES, *in-situ* UV-Vis and *operando* XAS. Finally, Kinetics experiments for SCR were performed.

Chapter 3. Promoting effect of iron on high temperature Selective Catalytic Reduction of NOx over Cu-SSZ-13*:* SCR systems usually operates at 200°C, an optimal low temperature for the performance of Cu-SSZ-13. However, during regeneration of the particulate matter filter in a typical diesel exhaust system, the temperature is raised, leading to a decrease in NOx conversion caused mainly by NH_3 and NO side reactions. Fortunately, it has been observed that Fe supported zeolites, even though presents poor SCR activity at low temperatures, have showed higher activity than Cu-zeolites at higher temperatures (near 500°C), by limiting to some extent the ocurrence of side reactions, such as NH_3 oxidation. We studied the use of a combined iron and copper supported SSZ-13 for SCR of NOx in the 200 - 600°C range, expecting to maintain high conversions at low temperatures from the use of copper and at high temperatures from the use of iron. During the experiments, Cu and Fe were exchanged onto SSZ-13 (independently and then mixed), then characterized by AAS and NH_3-TPD. Later, NO and NH_3 reaction rates were measured for standard SCR, NH_3 oxidation and NO oxidation, over Cu-SSZ-13 (Z-CuOH and Z2Cu), Fe-SSZ-13 and Fe-Cu-SSZ-13 catalysts in the 200 - 600°C range.

Chapter 4. Simultaneous effect of silicon content and the structure directing agent in improving Brönsted acidity of SAPO-34*:* To obtain SSZ-13, it is necessary a hydrothermal synthesis that can take up to 10 days in autoclaves at 160°C, a subsequent ion exchange process to generate Brönsted acidity and several calcination steps at temperatures from 550 to 600°C. Part of this time and energy consuming processes can be avoided when SAPO-34 is used as copper support instead of SSZ-13 for SCR of NOx. SAPO-34 is a silicoaluminophosphate molecular sieve with the same chabazite structure as SSZ-13 that only needs a 1-3 days hydrothermal synthesis and a single calcination process to be obtained. Albeit its use is limited to NOx elimination in fixed applications since it suffers disilication by the presence of water, SAPO-34 is still an important catalyst support for SCR reaction. In this work we analyze the effect of using different structure directing agents (tetraethylammonium hydroxide and morpholine) and varying the silicon content in the initial gel composition on SAPO-34 Brönsted acidity. Obtained samples were characterized by scanning electron microscopy (SEM), inducted coupled plasma optical emission spectrometry (ICP-OES), atomic absorption spectroscopy (AAS) and ammonia temperature programmed desorption (NH_3-TPD).

Chapter 2

Kinetic and Spectroscopic study of Selective Catalytic Reduction of NOx on SO$_2$ exposed Cu-SSZ-13

Chapter 2 contains the results of a 1.5 year stay in the research group of Professor Fabio Ribeiro at Purdue University, USA. This study was performed in collaboration with Arthur Shih, a PhD student at Purdue University and Hui Li, a PhD student at Notre Dame University, USA.

2.1 Introduction

Sulfur species are commonly found in diesel exhaust gases, being the fuel their major source. These compounds remain as important pollutants in exhaust gases from mobile-applications diesel engines, despite the introduction of ultra low sulfur diesel fuels (ULSD), which contain less than 15 ppm sulfur, and the implementation of stringent regulations. In a typical diesel exhaust, sulfur is presented predominantly in the form of SO_2 and small amounts of SO_3, since most of sulfur species are oxidized during the combustion process [44].

Sulfur oxides besides being precursor to greenhouse effect gases in the atmosphere, causes the emission of other pollutant gases since they are reported to cause catalyst deactivation in diesel exhaust gas treatment systems. In the specific case of SCR of NOx over Cu-CHA catalysts, several researchers have observed that sulfur induces a decrease in the NOx consumption rate [45, 46, 47]. Two main mechanisms have been proposed to explain this phenomenon. A first mechanism indicates, based on surface area studies, that pore blocking is produced by the formation of NH_4SOx-like species, thus causing mass transfer limitations. And the second mechanism includes the formation of sulfur intermediates in the copper active sites, inhibiting their catalytic activity [48, 45, 46, 47].

The effect of SO_2 exposure at SCR conditions in Cu-SSZ-13 surface area was studied by Wijayanti *et al* [47]. BET results indicated that Cu-SSZ-13 surface area decreased after SO_2 treatment under SCR gas compositions at temperatures from $100°C$ to $600°C$. Also, a decline in Cu-SSZ-13 SCR activity to reduce NO after sulfur exposing evidenced, according to the authors, that site-blocking effect made Cu-SSZ-13 copper sites less available. The decrease in surface area in the presence of SO_2 was also observed in a Cu supported mordenite catalyst, suggesting that the pore blocking is not caused by the morphology of the zeolite, instead is more dependent on the type of sulfur-Cu species formed [49].

There are evidences that SO_2 causes a decrease in the number of Cu-SSZ-13 active sites. Luo *et al* [46] performed DRIFTS measurements during ammonia adsorption over Cu-SSZ-13 and observed that two features (900 and 950 cm^{-1}) related to copper species were highly diminished after sulfur exposure. Additionally, NO conversion declined from 90% to less than 20% during SCR over sulfated Cu-SSZ-13. Jangjou *et al* [50] performed SCR kinetics experiments (Arrhenius plots) on sulfated Cu-SSZ-13 catalysts differentiated in the type of active site (Cu^{2+} and $[CuOH]^{1+}$), observing that the catalytic activity was severely inhibited by the presence of sulfur, independently on the active site. Shen *et al* [45] carried out kinetic experiments on sulfur exposed Cu-SAPO-34 catalyst during SCR. The apparent activation energy ($E_{a,app} = 33.99$ kJ mol^{-1}) was the same for fresh and sulfated Cu-SAPO-34, indicating that SO_2 poisoning does not change the reaction mechanism. However, DRIFTS, TPR and EPR characterizations indicated that the amount of Cu^{2+} active sites in Cu-SAPO-34 declined when exposed to sulfur, possibly by the formation of cupric sulfates/sulfites.

Furthermore, it is possible that Cu active sites in Cu-SSZ-13 behave different when exposed to SO_2. Jangjou *et al* [50] using DRIFTS, observed that SO_2 absorbs on a Cu-SSZ-13

11

sample with mostly Cu^{2+} only if ammonia is presented while interacts easily with a smple with mostly $[CuOH]^{1+}$ sites. A different Cu active site behavior was also observed on Cu-SAPO-34, Jangjou *et al* [38] used DRIFTS and NH_3-TPD to study the specific effect of sulfur exposing on the proposed Cu active sites on Cu-SAPO-34 [35]. Their results revealed that both pore blocking and Cu site poisoning can occur simultaneously depending on the type of copper site. Cu^{2+} sites inside the six-membered rings were completely blocked by sulfur and the nature of $[CuOH]^{1+}$ sites at the eight membered ring changed.

In this work, kinetics measurements were performed to identify the effect of sulfur on SCR of NOx over Cu-SSZ-13. Although, as mentioned above, Jangjou *et al* [50] already reported a similar work, we were more interested in analyzing the effect of sulfur on SCR reaction mechanism over Cu-SSZ-13. Therefore, we carried out kinetics experiments not only at SCR conditions, but also at conditions that simulate the oxidation SCR half-cycle observed in Figure 1.5. Additionally, the formation of sulfur intermediates and their effect on the formation of copper dimers in SCR mechanism was studied by in-situ UV-Vis-NIR. Furthermore, *operando* Cu K-edge XAS characterization were performed to identify changes in copper oxidation state and coordination in order to have more insights about the interaction of Cu actives sites in Cu-SSZ-13 with sulfur. Finally, *ex-situ* sulfur K-edge experiments were performed to identify the type of sulfur species absorbed in Cu-SSZ-13 samples during the adsorption of SO_2.

This work also involves a collaborative research, in which our experimental results were used by Li *et al* [51, 52] to perform computational studies. They used density functional theory (DFT) calculations to simulate possible Cu-sulfur species at Cu-SSZ-13 copper sites. First principle thermodynamic models were used to compare the thermodynamic stability of these species at SCR conditions. Moreover, DFT-based *ab initio* molecular dynamics (AIMD) was used to probe SOx mechanisms of adsorption and desorption. Results indicated that sulfur poisoning of Cu-SSZ-13 was not the result of molecular SO_2 or SO_3 adsorption onto the active site, but the result of formation of intermediate species such as ammonium sulfate and ammonium bisulfate, agreeing with Shen *et al* experimental results for sulfated SAPO-34 [45, 51].

2.2 Theoretical framework

2.2.1 Kinetic study of a catalytic reaction

2.2.1.1 Considerations regarding a kinetic study

In a most general way, a kinetic study provides information for the understanding of a chemical reaction at molecular level, through measuring and interpretation of reaction rates. Hence, it is essential in the design, operation and optimization of a chemical reactor. Several tasks are performed during a kinetic study [53]:

(a) Description of reaction pathways and their coherent involvement in an overall reaction

mechanism.

(b) Identification of elementary reactions steps (and their intermediate species) that does not appear in the reaction equation, because of their short lifetime. This will give information about the nature and reactivity of the active centers.

(c) Finding directly or indirectly the rate of the reaction steps.

Being SCR over Cu-CHA catalysts a well documented reaction mechanism, we used reported information to calculate rates in SO_2 saturated Cu-SSZ-13, to obtain evidences on the effect of sulfur on SCR over this catalyst. As we further explain in Sections 2.4.3 and 2.4.4, we complement kinetics findings by using *ex-situ*, *in-situ* and *operando* characterizations, along with reported computational studies.

2.2.1.2 Calculating reaction rates

NO reaction (consumption) rates (R_{SCR}) were calculated for standard and oxidation SCR on clean and sulfated ZCuOH and Z2Cu samples, as the flow of NO moles consumption ($\dot{n}_{NO}$) using Equation (2.1). All experiments were carried out at differential conditions (NO conversion less than 20%), which assures that products concentration during the reaction is very low, then its influence in the adsorption of reactants on the active sites is negligible [54].

$$R_{SCR} = \dot{n}_{NO} = C_{NO\ consumed} * \dot{V}_{total} * \frac{P}{RT} \tag{2.1}$$

Where, the concentration of NO consumed ($C_{NO\ consumed}$) is calculated as NO reduced by SCR minus NO oxidized to NO_2, Equation (2.2).

$$C_{NO\ consumed} = (C_{NO,in} - C_{NO,out}) - (C_{NO_2,in} - C_{NO_2,out}) \tag{2.2}$$

For more accurate comparison with reported data, all reaction rates were expressed in terms of grams of active specie (gcat), Equation (2.3) [55, 54].

$$Rate = \frac{\dot{n}_{NO}}{\text{weight or mols of active material}} \tag{2.3}$$

2.2.2 Catalyst characterizations used in this study

2.2.2.1 Powder X-ray diffraction (XRD)

X-ray diffraction (XRD) takes advantage on the ability of crystals to diffract X-rays in a characteristic way, allowing gather information about their structure, crystalline phase and composition [56]. When X-ray photons reach a sample, several absorption and scattering phenomena take place. One of these effects is called Rayleigh scattering, and occurs between the photons and the electrons surrounding the atomic nuclei. In this case, the energy of the scattered wave is unchanged then retaining its phase relationship to the incident wave,

Figure 2.1. Due to the periodic nature of a crystalline structure, constructive or destructive scattered radiation will result, leading to characteristic diffraction phenomena which can be studied to investigate the crystal structure of materials [57]. The principle of XRD method is based then, on the diffraction of X-rays by periodic atomic planes and the angle of the diffracted signal. The geometrical interpretation of XRD phenomenon is given by Bragg's Law, Equation (2.4) [58]. In this chapter, XRD was used to confirm that the synthesized SSZ-13 materials presented the crystalline planes characteristic of the reported chabazite fingerprint diffractogram. Also, XRD analysis was performed on SSZ-13 after copper ion-exchanges and after sulfur saturation with the aim of analyzing the effect of such procedures on the catalyst structure.
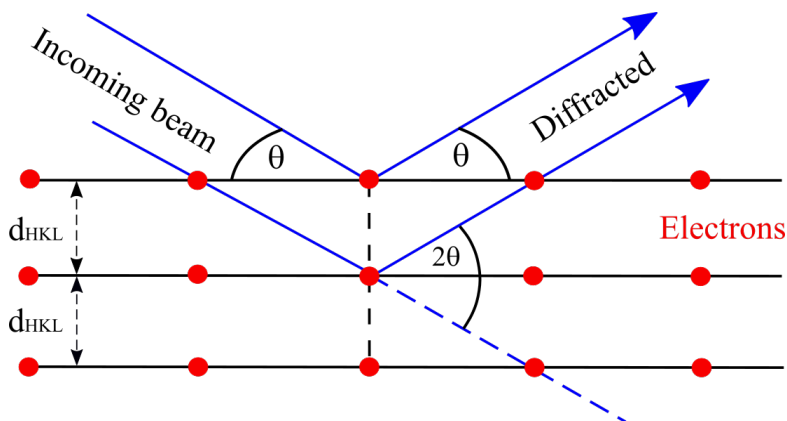
Figure 2.1: Geometrical condition for diffraction from lattice planes, modified from Hübshen *et al* [57].

$$n\lambda = 2d_{hkl}\sin(\theta) \tag{2.4}$$

In Equation (2.4) n is the order of diffraction, λ the wavelength of the incident beam in nm, d_{hkl} the lattice spacing in nm and θ the angle of the diffracted beam in degree.

2.2.2.2 Atomic absorption spectroscopy (AAS)

Atomic absorption spectroscopy is used to determine the concentration of an specific element in a gas-phase sample, making use of the relationship between absorption of light and concentration [59]. This is, when a parallel beam of continuous radiation of intensity I_0 passes through a cell containing atomic species of an element, the intensity of the transmitted radiation I_t (depicted in Figure 2.2) can be described by Bouguer-Lambert-Beer law (usually called Beer's law), Equation (2.5) [60, 59]. In this chapter AAS was used first to quantify the concentration of silicon and aluminum after synthesizing SSZ-13 samples; and later, to measure the composition of copper after ion-exchanging it in SSZ-13.

$$T_\nu = \frac{I_t}{I_0} = e^{-\mu_\nu b} \tag{2.5}$$
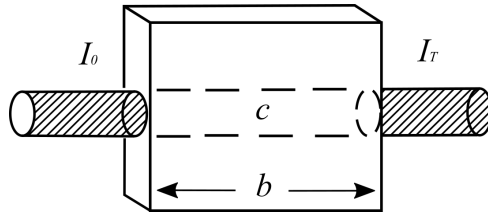
Figure 2.2: Atomic absorption cell of length b [59].

Where T corresponds to the transmitance, b thickness of the absorbing layer, ν the frequency of the transmitted radiation and μ_v is the linear absorption coefficient that is function of the incident energy and depends on the type of atoms and the density of the material. For monochromatic beams (with a specific single wavelength), Equation (2.5) can be rearranged to Equation (2.6) [59].

$$A = \log_{10}\left(\frac{I_0}{I_T}\right) = abc \tag{2.6}$$

Where A is the absorbance, a is the absorption constant for a given system and c is the concentration of the analyte atoms. Equation (2.6) predicts a linear relationship between absorbance and concentration as long as a and b remain constant.

2.2.2.3 Inductively coupled plasma - optical emission spectrometry (ICP-OES)
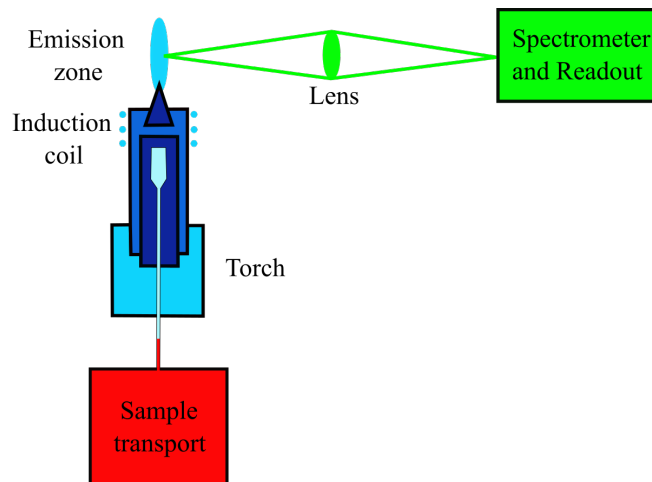
Figure 2.3: Schematic diagram of the core components of a typical ICP-OES [62].

ICP-OES is used in the quantification of trace elements and is based on the emission of photons from atoms and ions, after being excited by a radiofrequency (RF) discharge. During the analysis (Figure 2.3), a liquid sample is sprayed on a RF-induced argon plasma torch that vaporizes and energizes it through collisional excitation at very high temperature (approximately 10000 K). Some of the emitted photons are collected with a lens and imaged

15

onto the entrance slit of a wavelength selection device such a monochromator. The particular wavelength exiting the monochromator is then converted to an electrical signal by a photodetector. Finally, the signal is amplified and processed by the detector electronics [61].

2.2.2.4   Scanning electron microscopy (SEM)

Scanning electron microscopy, SEM, is used to examine the microscopic structure of materials by focusing an electron beam that scans over the surface area of the sample. A SEM consists in an electron gun (electron source and accelerating anode) and a series of electromagnetic lenses to focus the electrons, a vacuum chamber housing the sample stage, and a selection of detector, Figure 2.4. The main feature of SEM is the accurate measurement of the surface topography. Advanced SEM methods are capable of determining chemical composition of materials, the distribution of different phases and the local crystal structure at the surface of a sample [57]. In this work, we were interested in observing the formation if sulfur species in Cu-SSZ-13 samples after saturating them with SO_2.
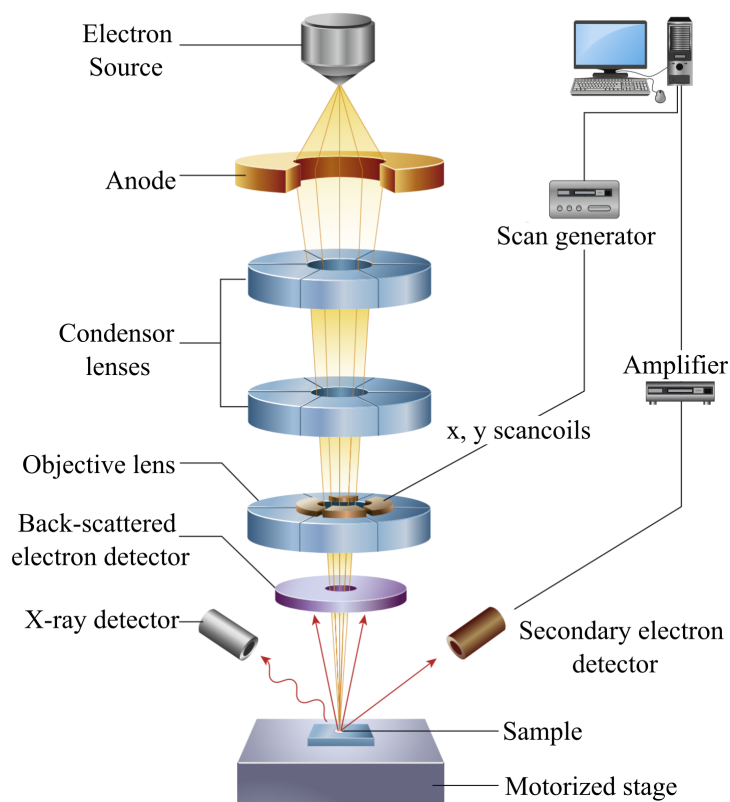
Figure 2.4: Schematic diagram of the core components of an SEM microscope [57].

2.2.2.5   Determination of acid site density by NH$_3$-TPD

Temperature-programmed desorption characterization, TPD, consists in measuring the desorption of a probe molecule from a sample while the temperature is increased linearly in

time. The quantification of the desorption is generally performed using a thermal conductivity detector (TCD) or a mass spectrometer (MS). The selection of the probe molecule depends on the characteristic of the material from which information is desired. For the characterization of acid site density in zeolites, usually ammonia or pyridine are used [60]. In microporous materials such as SSZ-13, NH_3 is preferred over pyridine, since the latter is not able to enter in the material small cavities, leading to an incorrect TPD analysis [63].

The desorption of ammonia in zeolites usually have two different characteristic peaks (preferable to be confirmed by a symultaneous characterization, e.g. *in-situ* FTIR). A low temperature peak, related to NH_3 physisorbed and adsorbed on Lewis acid sites, and a high temperature feature related to NH_3 adsorbed on Brönsted acid sites [64]. In zeolites, the amount of NH_3 molecules adsorbed on Brönsted acid sites is directly related to the amount of aluminum atoms in the zeolite structure, therefore, NH_3-TPD can be used to identify if aluminum atoms presented in a sample are part of the zeolite framework or correspond to extraframework aluminum (usually in the form of Al oxides) [63, 65].

2.2.2.6 Vibrational spectroscopy characterizations

Vibrational spectroscopy characterization methods are used to analyze the structure of molecules by examining the interaction between electromagnetic radiation and nuclear vibrations in molecules. These methods are based on the fact that, when submitted to radiation, the atoms in a molecule (capable of suffer dipole-moment changes), vibrate within frequencies characteristic of the molecule, therefore vibrational spectroscopy can be used in compound identification. Vibrational techniques are usually named after the spectrum region they study, thereby infrared spectroscopy (IR) is focused on infrared region. There are three basic types of molecular vibration, stretch, bending and torsion [66].

2.2.2.6.1 Fourier transformed infrared spectroscopy (FTIR)

FTIR is an infrared spectroscopy in which the Fourier transform method is used to obtain an infrared spectrum in a whole range of wavenumbers simultaneously. The key component in the FTIR system is the Michelson interferometer, as illustrated in Figure 2.5. The interferometer is composed of one beam-splitter and two mirrors. The beam-splitter transmits half of the infrared (IR) beam from the source and reflects the other half. The two split beams strike a fixed mirror and a moving mirror, respectively. After reflecting from the mirrors, the two split beams combine at the beam-splitter again in order to irradiate the sample before the beams are received by a detector. The function of the moving mirror is to change the optical path lengths in order to generate periodical light interference between the two split beams. As result the signal coming out an interferometer (called interferogram) is composed by every infrared frequency that comes from the source. This way, ever measurement in the interferogram contains information from all frequencies simultaneously.

Fourier transformation is necessary to convert an interferogram into an infrared spectrum, which is a plot of the light intensity versus wavenumber. The Fourier transform is based on a fact that any mathematical function can be expressed as a sum of sinusoidal waves. Fourier
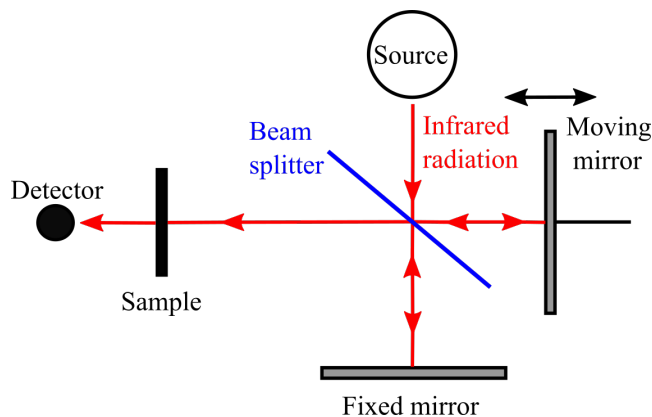
Figure 2.5: Schematic diagram of a Michelson interferometer

transform, Equation (2.7), converts the intensity versus optical path difference from the interferogram to intensity versus wavenumber. The optical path difference can be considered to be in the time (t) domain because it is obtained by multiplying time with the speed of a moving mirror. The wavenumber (ω) can be considered in the frequency domain because it is equal to frequency divided by the light speed.

$$F(\omega) = \frac{1}{\sqrt{2\pi}} \int_{-\infty}^{\infty} f(t)e^{-I\omega t}dt \tag{2.7}$$

Quantification in FTIR is based on the linear relationship between absorbance and concentration stated by Beer's law, Equation (2.6). However, in the practice there can be disturbances to this linearity. Therefore, several numerical methods have been developed to obtain a more precise estimation of concentrations from FTIR spectra. For the compounds quantified by FTIR in this study (NO, and NH_3), empirically it was observed a better fit with a partial least-square based regression method [67].

2.2.2.6.2 Ultraviolet-visible-near infrared spectroscopy (UV-Vis-NIR)

Ultraviolet-visible-near infrared spectroscopy (UV-Vis-NIR) corresponds to the wavenumber range of 50000-4000 cm^{-1}, which is usually divided in three regions:

UV: 50000 - 25000 cm^{-1}

Vis: 25000 - 12500 cm^{-1}

NIR: 12500 - 4000 cm^{-1}

For applications in heterogeneous catalysis, the near infrared (NIR) can provide information about CH, OH and NH groups from overtones and combinations of their fundamental stretching frequencies. The ultraviolet and visible regions of the spectrum provide information related to transition metal ion (TMI) centers, adsorbed molecules and the support which can be amorphous metal oxides or porous crystalline materials such as zeolites [68].

Light scattering caused by the size of particles from solid samples may reduce the amount of light transmitted through these materials, being insufficient for transmission spectroscopy in the UV-Vis-NIR range. Therefore, a difussive reflectance spectroscopy (DRS) cell has to be adapted to the UV-Vis-NIR equipment. In DRS the scattered light from the sample are concentrated in a sphere and detected by a photomultiplier (UV, Vis) or a PbS cell (NIR). For a better analysis of the results, the measured diffuse reflectance (R_∞) most be expressed in terms of Kubelka-Munk function, using Equation (2.8), which is approximately proportional to the concentration of the studied species [68, 69].

$$F(R_\infty) = \frac{(1 - R_\infty)^2}{2R_\infty} = \frac{K}{S} \tag{2.8}$$

Where the apparent absorption (K) and the apparent scattering coefficient (S) are characteristic of the sample. R_∞ is experimentally measured as the light intensity reflected from the powdered sample divided by the light intensity reflected from an ideally white reference standard [69].

2.2.2.7 X-ray absorption spectroscopy (XAS)

When a collimated X-rays beam passes through a material, its intensity will be decreased by cause of several energy adsorption and scattering phenomenon depicted in Figure 2.6 and listed as follows [70, 60, 71]:

(a) An atom is ionized by the absorption of a photon from the beam. This consists in the excitation of a deep-core electron from the absorbing atom, which is then promoted to an unoccupied state above the Fermi energy level (E_F) and propagated away as a photoelectron (leaving an electron vacancy), with a kinetic energy given by the photoelectric effect, Equation (2.9).

$$E_k = h\nu - E_{binding} \tag{2.9}$$

Where h corresponds to the Plank constant, ν is the frequency of the incident photon and $E_{binding}$ is the binding energy of the propagated photoelectron.

(b) The vacancy generated after the emission of a photoelectron is filled with a lower-energy-shell electron, which needs to release energy in the form of a fluorescent photon.

(c) The energy liberated from an electron filling a lower energy vacancy, instead of being released as a fluorescent photon, is absorbed by another electron that in turn is emitted as an Euger electron.

(d) Low energy X-ray radiation is scattered from electrons in the sample.
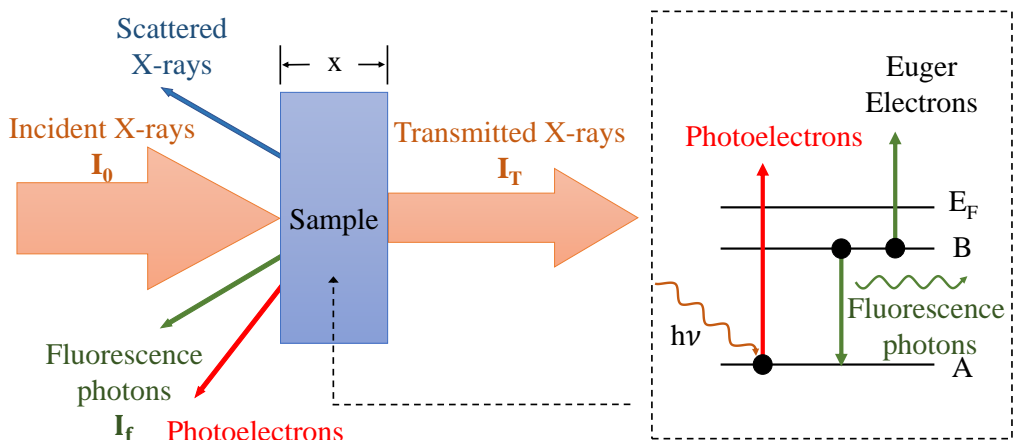
Figure 2.6: Depiction of X-rays absorption in a sample, adapted from [70]. A and B are arbitrary energy levels, while E_V correspond to the Fermi energy level

During an XAS experiment, the decrease in the intensity of a X-ray beam with a thickness b, as it passes through a sample is determined by the absorption characteristics of the sample and can be described by Lambert's law, Equation (2.5) [60]. When the photon energy is sufficient to cause the excitation of a core electron of the absorbing atom, producing a photoelectron (as explained in Figure 2.6), the energy absorption increases drastically and gives rise to an adsorption edge, Figure 2.7. In other words, the adsorbed energy in an edge corresponds to the binding energy of electrons (in the K, L, M, etc shells) of the absorbing atoms. As depicted in Figure 2.6, XAS spectra are generally divided into three different sections: pre-edge, X-ray absorption near edge structure (XANES) and x-ray absorption fine structure (EXAFS) [70, 60, 72].

(a) *Pre-edge*: the small features observed in this region are usually due to the electron transitions from the core level to the higher unfilled or half-filled orbitals (e.g, s → p, or p → d) [70].

(b) *XANES*: X-ray absorption near edge structure lies close to the absorption edge, with an upper limit usually set arbitrarily at 50 eV above the edge. XANES have been used to obtain information about the oxidation state of on an element as a catalyst is subjected to treatments such as reduction, oxidation or exposure to some reactant [73]. The features of a XANES spectrum that are typically used to determine the average oxidation state of an element are the absorption edge position [73, 72]. For the case of copper, McEwen *et al* [73] have reported that Cu species with a 2+ oxidation state have edge energies ranging from 8983.7 to 8988.5 eV, while Cu(1+) species have an edge energy of 8980.6 eV.

(c) *EXAFS*: when the photoelectron leaves the absorbing atom during XAS, its wave is backscattered by the neighboring atoms, causing the oscillations observed after XANES in Figure 2.7 [71]. As a result, EXAFS is used to determine the coordination atoms under reaction conditions and to measure interatomic bond distances [72]. EXAFS

spectrum most be refined by post-edge background removal and normalization followed by a Fourier transformation [60]. There are several available software packages to carry out this fitting, the most common are WinXAS® and freeware-based DEMETER [74, 75].
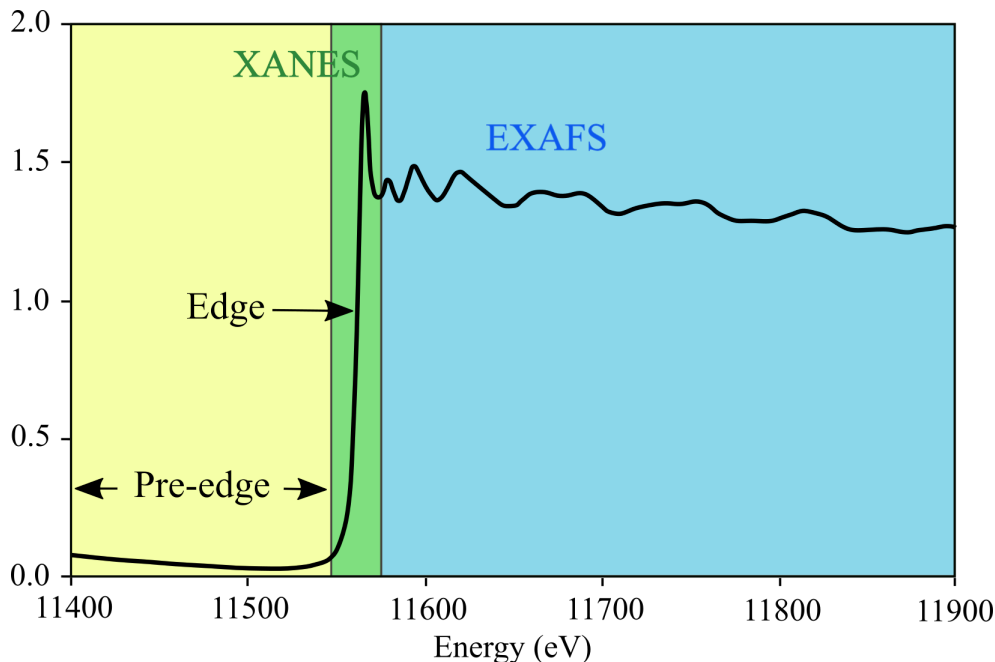
Figure 2.7: Depiction of the regions of an XAS spectrum

2.2.3   *In-situ* characterizations

Characterizations of an heterogeneous catalyst at reaction conditions or *in-situ* characterizations are performed to obtain information about the nature of its active sites, and its interaction with reactants, products and intermediate species. Catalyst-ambient interactions may change the structural and electronic properties of the catalyst and would be very difficult to detect in the absence on an *in-situ* study [76]. In the literature is commonly to find the terms *cut-off* and *operando*. They are essentially modified *in-situ* characterization and usually are performed in the same experimental setup.

A *cut-off* experiment is an *in-situ* characterization in which one or several reactants are suddenly cut-off from being in contact with the catalyst. This is used generally to identify intermediate reactions while elucidating a reaction mechanism. On the other hand, during an *operando* characterization, besides submitting the sample to reaction condition, the composition of exiting gases is measured. The aim of this is to guarantee that the characterization was performed under catalytic condition and complement the analysis with kinetic measurements [77].

2.3 Experimental methods

2.3.1 Synthesis of Cu-SSZ-13

H-SSZ-13 form of SSZ-13 was obtained by a hydrothermal synthesis reported by Fickel *et al* [78] which is based on a patent developed by Zones [18]. Materials with Si:Al ratios of 4.5, and 25 were synthesized. The first step consisted in obtaining a sodium form of the zeolite (Na-SSZ-13). For this, $Al(OH)_3$ (100%, SPI Pharma), NaOH (38% in water, Mallinckrodt), N,N,N-trimethyl-1-adamantyl ammonium hydroxide (25% in water, Sachem) and water (Millipore, Synergy UV water Purification System) were mixed and stirred for 15 min. Later, fumed silica (100% Cab-o-sil M5®, CABOT) was added to the mixture and the stirring continued for 2 h. Then, the mixture was placed into 75 mL autoclaves in a rotating oven at 160°C, Figure 2.8.

Figure 2.8: Rotating oven for the synthesis of SSZ-13

As-synthesized materials were washed with water and acetone then centrifuged repeatedly until reaching a pH near 7. Subsequently, the samples were dried overnight at 100°C and calcined in 100 mL min^{-1} air at 600°C for 10 h (1°C min^{-1} ramp). The resulting Na-SSZ-13 form was converted in NH_4-SSZ-13 by ion exchange with 0.1 M NH_4NO_3 (>99%, Aldrich) (100g solution per gram of catalyst) at 80°C for 10 h. The H-SSZ-13 form was obtained by calcining NH_4-SSZ-13 at 550°C for 6 h under 100 mL min^{-1} air (1°C min^{-1} ramp).

Copper was ion-exchanged on H-SSZ-13 Si/Al = 4.5 and 25, expecting to obtain samples with ~100% $[CuOH]^{1+}$ and ~80% Cu^{2+} (from now on, denoted ZCuOH and Z2Cu, respectively) using aqueous solutions of $Cu(NO_3)_2$ (>99.99%, Aldrich) at 25°C . During this process, the pH was controlled to a value of 5 by drop-wise additions of NH_4OH (30% NH_3 in H_2O, Aldrich) 1 M, to avoid the precipitation of copper oxide cluster into the zeolite and to mitigate Al structural changes [41].

Cu-SSZ-13 samples were saturated with sulfur (SO$_2$) at 200 and 400°C by Cummins$^®$, a diesel engine manufacturer, as part of a joint research project between this company and Purdue University. It was decided to saturate the catalyst with SO$_2$ instead of having a SO$_2$ flow during SCR tests because the usual concentration of sulfur in diesel exhaust gases is above 15 ppm, and it would be difficult to detect its effect on the catalysts at such low concentrations [44]. Typically, 600 mL min^{-1} of N$_2$ containing 100 ppm SO$_2$ at 200 or 400°C flowed through 0.5 g of sieved catalyst, for a pre-determined time until obtaining a cumulative molar exposure was S:Cu = 5 (in this work, SO$_2$ treated samples are named preceded by 200CSO2 or 400CSO2 for saturation at 200 or 400°C, respectively). Saturation temperatures were selected to avoid regeneration of the catalyst by SO$_2$ desorption [79].

2.3.2 Characterization of Cu-SSZ-13

2.3.2.1 Atomic absorption spectroscopy

Elemental analysis of all Cu-SSZ-13 samples was performed on a Perkin-elmer AAnalyst$^®$ 300 atomic absorption spectrometer. The procedure consisted in analyzing the sample and at least three different standard solutions of the element of interest to make calibration curves (Si, Al or Cu).

Samples were prepared on 125 mL high density polyethylene bottles by dissolving 20 mg of the catalyst in 2.0 g of 40% HF (>99.9%, Aldrich) for 8 h. Then, the acid concentration is reduced by adding 120 mL of ultrapure water (Millipore, Synergy UV Water Purification System). For calibration purposes, standard solutions of Si, Al and Cu were prepared by diluting 1000 ppm commercial solutions in known amounts of ultrapure water.

2.3.2.2 SEM

To observe changes in SSZ-13 structure after sulfation, scanning electron microscopy images for Z-CuOH and 400°C SO$_2$ Z-CuOH were collected on a FEI Quanta 3D FEG$^®$ scanning electron microscope. The samples were not pre-treated before the analysis.

2.3.2.3 ICP-OES

Composition of sulfur in sulfated samples was measured using an iCAP 7400 ICP-OES analyzer. Before the analysis, all the samples were microwave digested. Typically, ∼0.15 g of the sample were transferred to 80 mL teflon liners, then digested using 9 mL HNO$_3$ and 3 mL HF at 230°C for 20 min. Next, the sample was allowed to cool to ambient temperature for 1 h, after which point 10 mL of 4% boric acid was added. The sample was heated while stirring to 180°C and held for 15 min. Once cooled, the resulting liquid was diluted to 100mL with deionized water.

2.3.2.4 Powder X-ray diffraction

X-ray powder diffraction patterns for H-SSZ-13, Cu-SSZ-13 and sulfated Cu-SSZ-13 samples were obtained using a Rigaku Smart Lab® X-ray diffractometer with Cu K(α) radiation source operated at 1.76 kW. The diffraction patterns were measured from 4-40° 2θ at a scan rate of 2.4° min^{-1}.

2.3.2.5 NH$_3$-TPD of H-SSZ-13

An ammonia temperature programmed desorption process developed at Purdue University was used to quantify the number of Brönsted acid sites in H-SSZ-13 samples. The aim of this process was to confirm that the composition of aluminum quantified by atomic absorption corresponded to framework attached aluminum atoms [65, 34]. First, Cu-SSZ-13 samples ($\sim$50 mg) were supported between two quartz wool plugs inside an U-shaped quartz flow-thru sample tube Figure 2.9. Then, the tube was held within a clam-shell furnace in a flow of NH$_3$ (3% NH$_3$ in argon, Praxair) diluted to 500 ppm with ultrahigh purity He (UHP, 99.99 %) at 160°C for 2 h and a total flow rate of 350 cm^3 min^{-1}. Later, the now NH$_3$-saturated samples were purged in flowing UHP helium (350 cm^3 min^{-1}) containing $\sim$10% ultrapure water at 160°C for 8 h, to desorb all NH$_3$ molecules from the sample except those bound to Brönsted acid sites.
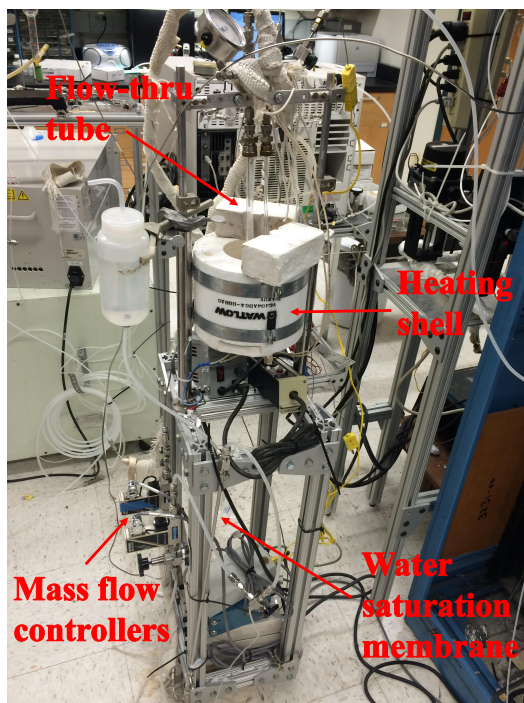
Figure 2.9: Ammonia saturation unit for TPD experiments

TPD measurements were performed by placing the same tube used in the saturation unit in a Micromeritics® Autochem II 2920 Chemisorption analyzer equipped with an Agilent® 5975C mass selective detector (MSD). During the analysis, 50 cm^3 min^{-1} helium (UHP, Praxair) flew through the sample at ambient temperature for 1 h. Later, a temperature ramp was settled from 24 to 1000°C at a rate of 0.167°C s^{-1}. The effluent stream from the quartz cell was sent to the MSD for quantification.

After each TPD experiment, an injection of argon was used as a reference standard to correct instrument drift between TPD experiments. Typically, a 0.5 cm^3 sample loop was filled with argon (UHP, Praxair) and injected into a 50 cm^3 min^{-1} flow of UHP helium heading toward the mass spectrometer detector (MSD) [65].

2.3.3 SCR kinetics

Kinetic measurements for standard SCR reaction over fresh and sulfated Cu-SSZ-13 were performed on a 2.5 cm ID bench top tubular glass reactor, with a quartz frit located in the middle of the tube to hold a 2 - 8 mg catalyst bed. The catalyst (sieved to a nominal size of 125 - 250 μm) was placed between two layers of quartz wool layer and diluted in silica gel. Thermocouples were placed just above and below the catalyst bed to guarantee constant temperature and quartz beads were placed on a mesh above the catalyst to ensure a proper gas mixing. Complete reaction rig is presented in Figure 2.10
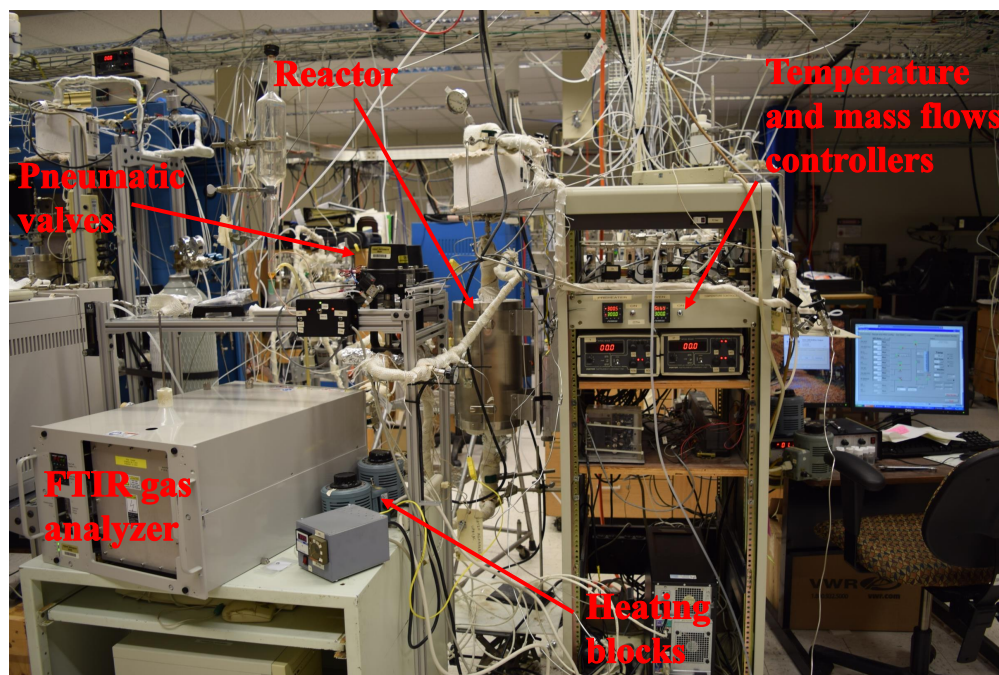
Figure 2.10: Reaction rig for measuring standard SCR reaction on Cu-SSZ-13 catalyst

The gas composition corresponded to the standard NH_3-SCR reaction (300 ppm NO, 300 ppm NH_3, 8% CO_2, 10% O_2 (60% for kinetics at oxidative conditions), ~3% H_2O and balance N_2 for an overall flowrate of ~1000 mL min^{-1} (and GHSV of 3000000h^{-1})) [35, 42]. Water was added by flowing balance N_2 through a Perma Pure MH$^®$ humidifier. Before entering the reactor all gases were pre-heated to 200°C (except NH_3 to avoid side reactions). NH_3 (3000 ppm in He, Matheson Tri-gas) was added just at the reactor inlet to avoid formation of NH_4NO_3. Effluent gases were analyzed by a MKS Multigas$^®$ 2030 gas phase FT-IR spectrometer.

SCR gas compositions were selected according to the following considerations [20]:

- H_2O, NO, CO_2 and O_2 compositions correspond to a diesel engine exhaust gases. Particulate material, unburned hydrocarbons and CO were not included because it is assumed that those gases are removed in a pre-SCR treatment stage.

- NH_3/NO ratio is usually 1:1 to avoid ammonia slip, as it would become another pollutant [23].

- CO_2 is inert for the SCR reaction .Therefore, some authors have decide to replace it by an inert carrier gas (Ar, He, etc.) [80].

2.3.4 UV-Vis-NIR

2.3.4.1 *In-situ* UV-Vis-NIR
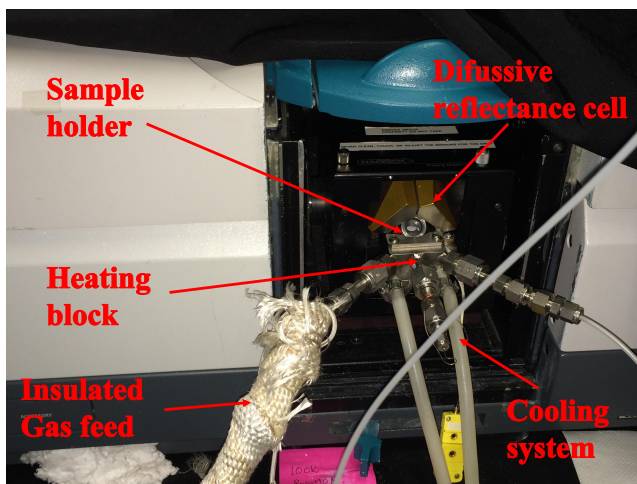
Figure 2.11: *In-situ* cell installed on Varian Cary 5000$^®$ FIG-UV-Vis-NIR spectrophotometer

In-situ UV-Vis-NIR Spectrum from clean and sulfated Cu-SSZ-13 samples were collected on a Cary 5000$^®$ UV-Vis-NIR spectrophotometer equipped with a Harrick-Scientific

Praying-Mantis$^\circledR$ diffuse reflectance optics and accessories, Figure 2.11. Spectra were collected from 7000 to 50000 cm^{-1} with a scan speed of 2000 cm^{-1} min^{-1}. BaSO$_4$ (99%, Sigma-Aldrich) and H-SSZ-13 with Si/Al = 4.5 and 25 spectra were used as background correction.

All H-SSZ-13 and Cu-SSZ-13 samples were dehydrated with 100 mL min^{-1} air (99.99%, Indiana Oxygen) at 250°C for 8 h before analysis. The relatively low dehydration temperature of 250°C was selected to avoid desorption of sulfur species. Later, the samples were saturated with 500 ppm NH$_3$ (3000 ppm in He, Matheson Tri-gas) in 100 mL min^{-1} UHP helium (99.999 %, Indiana Oxygen) at room temperature (24°C). Finally, the temperature was increased to 200°C while flowing NH$_3$. Spectra were collected in all steps of the procedure.

2.3.4.2   *Ex-situ* UV-Vis-NIR in several commercial Cu salts

Ex-situ UV-Vis-NIR was collected at ambient conditions from commercial sulfur-and-ammonium-containing copper salts, using an *ex-situ* accessory (Figure 2.12) in the UV-Vis-NIR spectrophotometer and diffuse reflectance cell described in Section 2.3.4.1. Spectra were collected from 7000 to 50000 cm^{-1} with a scan speed of 2000 cm^{-1} min^{-1} and BaSO$_4$ (99%, Sigma-Aldrich) spectrum was used as background correction.

Figure 2.12: *Ex-situ* accessory installed on Varian Cary 5000$^\circledR$ UV-Vis-NIR spectrophotometer

2.3.5   X-ray absorption spectroscopy

2.3.5.1   *Operando* Cu K-edge XAS on Cu-SSZ-13

Cu K-edge X-ray absorption experiments on unsulfated and sulfated Cu-SSZ-13 samples at *operando* SCR and reducing-SCR (in a flow of NH$_3$ and NO) conditions were performed at sector 10-ID of the Advanced Photon Source at Argonne National Laboratory, USA. A mixture of carbon beads and 8-20 mg of catalyst was held inside a 4 mm ID carbon reactor

within two layers of quartz wool. The reactor was then secured inside an aluminum heating block which had a 25.4 x 2 mm wide slit in the center to allow an X-ray beam to pass through the reactor, Figure 2.13.
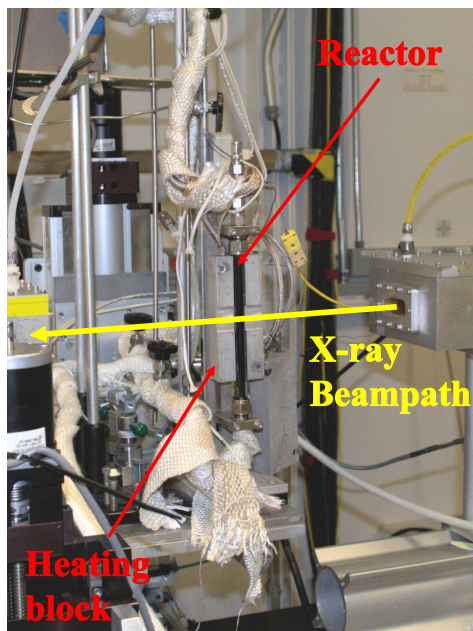
Figure 2.13: Carbon reactor used during *Operando* XAS experiments. Note: The heating block was intentionally left open to make the reactor visible

A standard SCR gas mixture consisting in 320 ppm NO, 320 ppm NH_3, 8% CO_2, 10% O_2, 6% H_2O and balance N_2 for an overall flowrate of ~500 mL min^{-1} (adjusted to ensure differential conditions (<20% NO conversion) was used. first, N_2 was humidified through a Perma Pure MH$^®$ humidifier. Following, NO (3000 ppm in N_2, Matheson Tri-Gas), O_2 (20% in He, Airgas) and CO_2 (100%, Airgas) were fed. The reacting flow was allowed to reach stable concentration by flowing it through a bypass for 1 h before entering the reactor, and at the same time, it was preheated to 200°C by heat tracing and covering the gas tubing with heating tape. NH_3 (3000 ppm in He, Matheson Tri-gas) was the last added gas to avoid the formation of NH_4NO_3. XAS spectra were taken each ~2 min until stabilization in two consecutive spectra was observed. At the same time, compositions at the reactor outlet were measured using a Multi-Gas 2030$^®$ FTIR gas analyzer. *Operando* XAS reaction setup is showed in Figure 2.14.
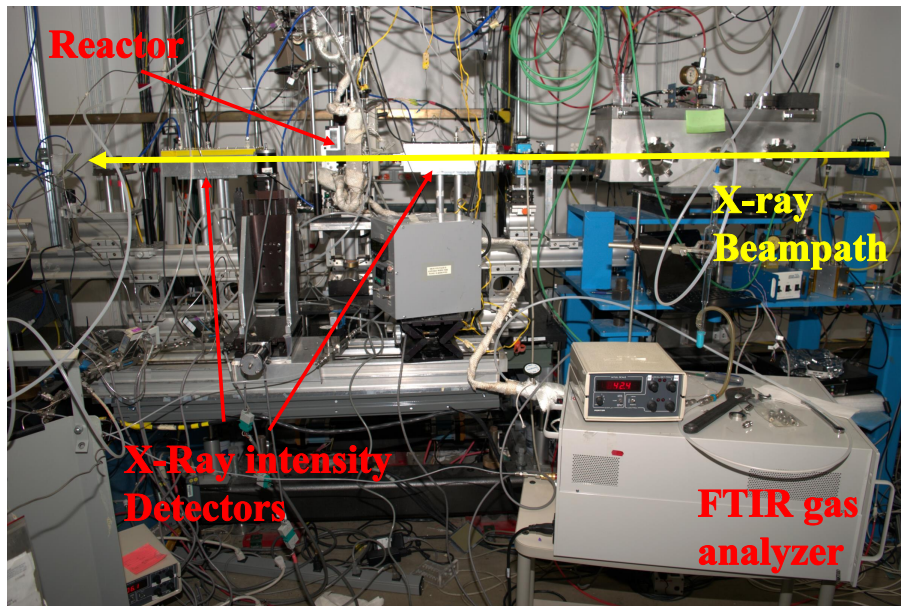
Figure 2.14: Experimental setup for *Operando* XAS experiments

2.3.5.2 *ex-situ* Sulfur K-edge XAS on sulfated Cu-SSZ-13 and several copper and sulfur salts

Ex-situ Sulfur K-edge XANES spectra from sulfated Cu-SSZ-13 samples, $Cu(NH_3)_4SO_4.H_2O$ (98%, Sigma-Aldrich) and $CuSO_4.5H_2O$ (99.9%, Sigma-Aldrich), were collected at sector 9-BM of the Advanced Photon Source at Argonne National Laboratory, USA. Typically, 8-20 mg of the sample was held on a the sample holder showed in Figure 2.15, then placed in the cell observed in Figure 2.16. Two XAS spectrum were collected from each sample.
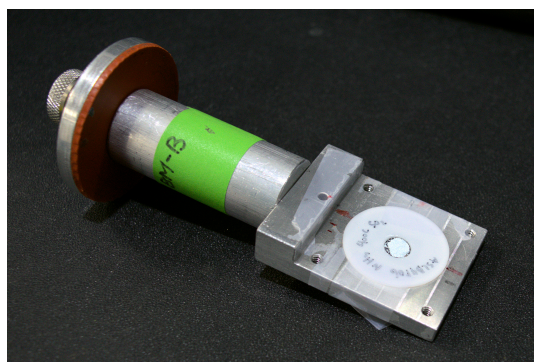
Figure 2.15: Sample holder for *ex-situ* sulfur K-edge experiments
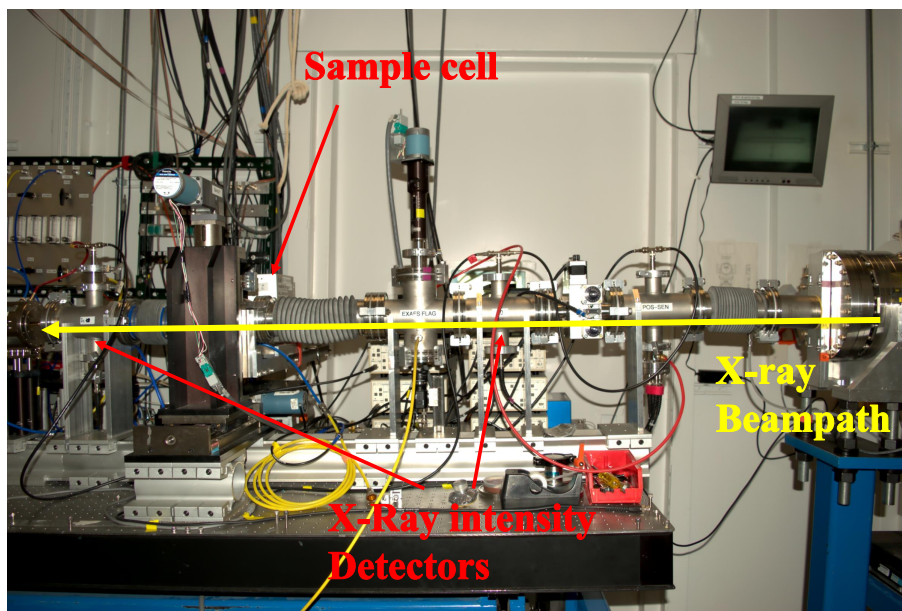
Figure 2.16: Experimental setup for carrying out *ex-situ* sulfur K-edge experiments

2.4 Results and discussion

2.4.1 Characterization of Cu-SSZ-13 catalyst

2.4.1.1 Atomic absorption

Si:Al ratios of 4.5 and 25 were defined for the synthesis of SSZ-13, considering procedures already reported that generate materials with paired and isolated Brönsted active sites, respectively [20]. This is important, since Cu^{2+} sites need two paired Brönsted sites for its formation, which are expected to be formed exclusively in the material with Si:Al 4.5. In the same way, $[CuOH]^{1+}$ sites are expected to be formed only in the material with Si:Al 25, as they only occur in the presence of isolated Brönsted sites.

Table 2.1: Atomic absorption results for ZCuOH and Z2Cu. Si/Al and Cu/Al are presented as molar ratio. Si, Al and Cu composition are presented as mass percent. Si and Al percent were measured before incorporating Cu

Sample name	Si/Al	%Si	%Al	Cu/Al	%Cu
Z2Cu	4.620	0.8314	0.1729	0.21	3.86
ZCuOH	24.673	0.9528	0.0371	0.37	1.50

Silicon and aluminum molar ratios in Cu-SSZ-13 samples, obtained by atomic absorption, and presented in Table 2.1 show that the expected Si:Al ratios of 4.5 and 25 were obtained. In addition, Cu content in both ZCuOH and Z2Cu guarantee that no Cu oxides were formed. This is further discussed in Section 2.4.2.1.

2.4.1.2 SEM

Scanning electron microscopy was used to identify the formation of sulfur species on Cu-SSZ-13 structure after exposition to SO_2, Figure 2.17. No differences were observed in Cu-SSZ-13 images taken before and after sulfation.
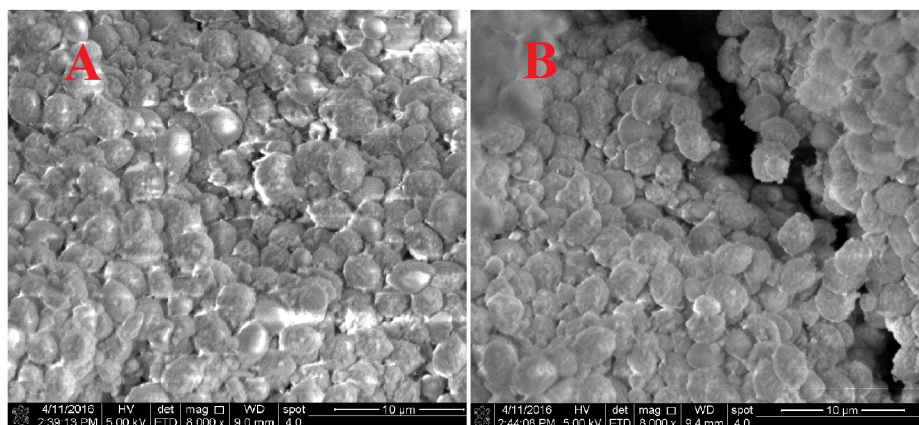
Figure 2.17: SEM images for (A) ZCuOH and (B) 400CSO2 ZCuOH

2.4.1.3 ICP-OES

Elemental analysis of sulfur in Cu-SSZ-13 samples by ICP-OES is presented on Table 2.2. It is observed that ZCuOH presented more sulfur absorption than Z2Cu, with the same expositions to SO_2 and O_2. This is consistent with DFT results that show a stronger binding energy of SO_2 in $[CuOH]^{1+}$ [81]. It can be also observed that higher temperatures caused more sulfur absorption in both Z2Cu and ZCuOH.

Table 2.2: ICP-OES results for Z2Cu and ZCuOH

Sample	S %wt
200C SO_2 Z2Cu	0.36
200C SO_2 ZCuOH	0.75
400C SO_2 Z2Cu	0.51
400C SO_2 ZCuOH	1.52

2.4.1.4 X-ray diffraction
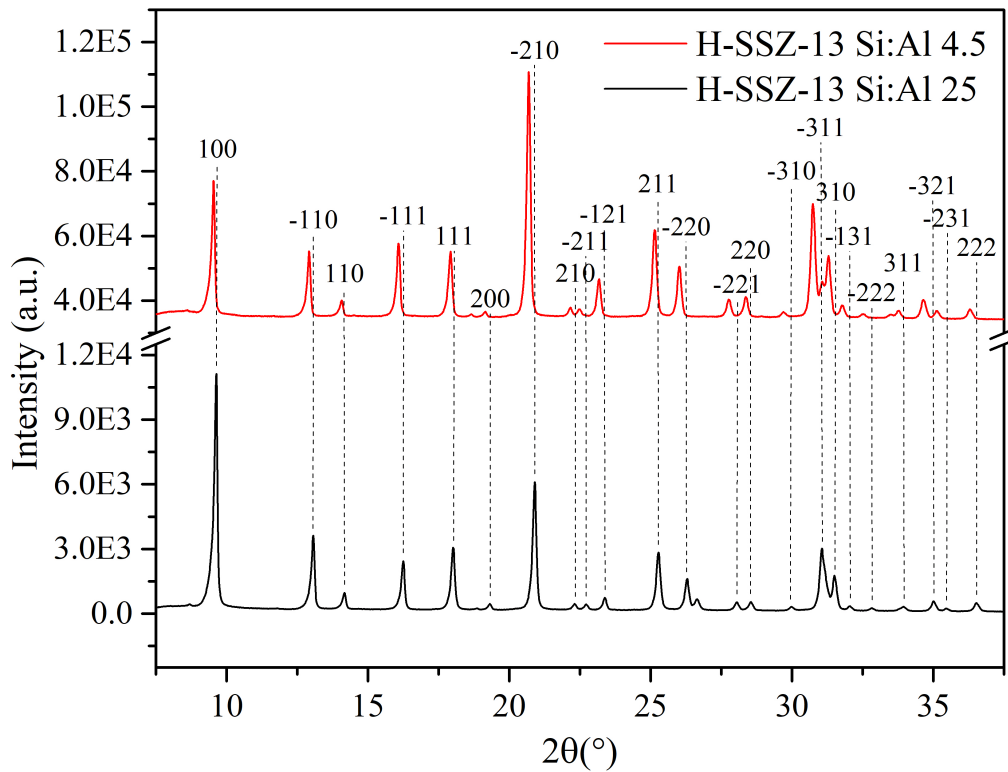
Figure 2.18: Unit cell parameters for H-SSZ-13 Si:Al = 4.5 and 25

Powder X-ray diffractograms for synthesized H-SSZ-13 samples, in Figure 2.18, presented all the expected crystal phases for CHA framework [16]. The differences in the intensity of some reflections are related to the different Si:Al ratio of ZCuOH and Z2Cu [82, 83]. Figure 2.19 shows that the incorporation of Cu did not cause additional peaks, that would be related to other crystalline phases such as Cu oxides [82].
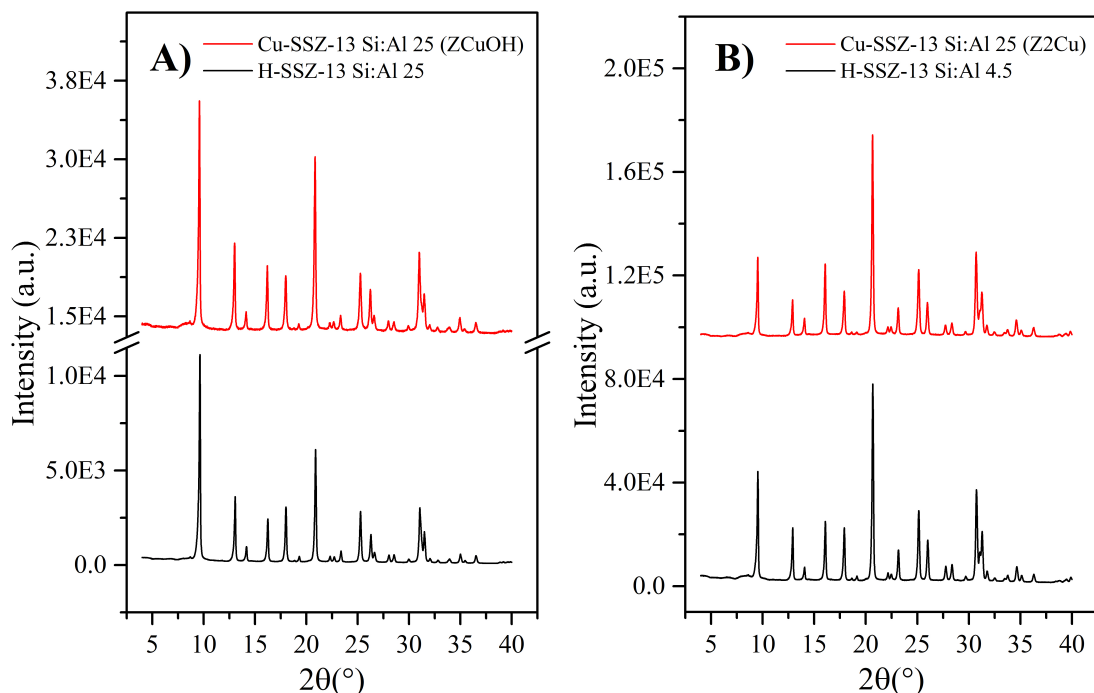
Figure 2.19: XRD results for H-SSZ-13 and Cu-SSZ-13 samples

Figure 2.20 shows XRD diffractograms for ZCuOH and Z2Cu before and after sulfation, where it is evident that the presence of sulfur did not generate new reflections in neither ZCuOH nor Z2Cu, hence the sulfation process did not caused structural damage to the zeolites. To verify these results, the full width at half the maximum intensity (FWHM) and crystallite size (τ) were estimated by Gaussian peak fitting and Scherrer equation (Equation (2.10)), respectively. Peaks at low diffraction angle were selected during τ calculation, to reduce the possible influence of lattice strain [83]. Results presented in Table 2.3 confirm that there were not significant structural changes in ZCuOH and Z2Cu after sulfation.

$$\tau = \frac{K\lambda}{L\cos\theta} \tag{2.10}$$

Where:

τ: crystallite size (Å)

λ: wavelength of the x-rays used (Cu in this case)

k: dimensionless shape factor

L: full width at half the maximum intensity (FWHM) of the selected band θ: diffraction angle

33
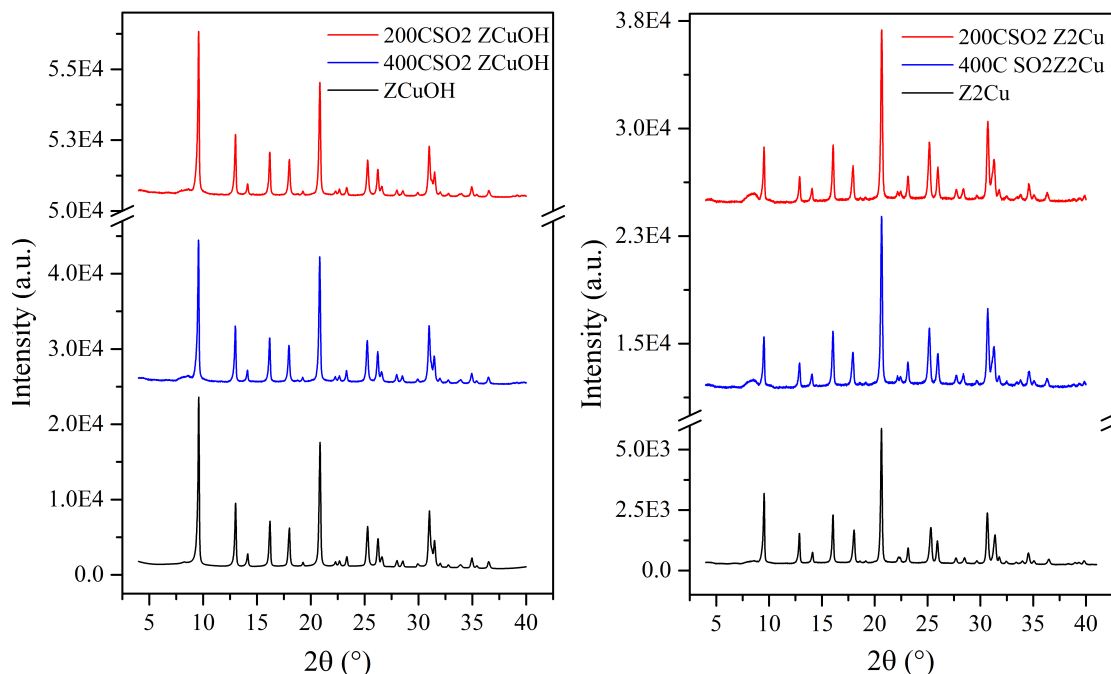
Figure 2.20: XRD results for ZCuOH and Z2Cu, before and after sulfation

Table 2.3: FWMH and crystalite size for Z2Cu and ZCuOH

Sample	2θ	FWMH	τ (Å)
ZCuOH	9.5805	0.19751	7.8325
200C SO_2 ZCuOH	9.5505	0.18402	8.4066
400C SO_2 ZCuOH	9.5567	0.18152	8.5224
Z2Cu	20.633	0.19027	8.1298
200C SO_2 Z2Cu	20.656	0.20722	7.4649
400C SO_2 Z2Cu	20.647	0.21253	7.2784

2.4.1.5 NH$_3$-TPD of H-SSZ-13

The number of Brönsted acid sites (BA) formed into a zeolite is given by the number of aluminum atoms presented in its framework, since BA are formed when Al generates anionic unbalances that are compensated with protons, as discussed in Section 1.1.5.1. For that reason, the aluminum content (in this work quantified by atomic absorption) should give an estimated of the number of BA for a given amount of H-SSZ-13. However, sometimes during the synthesis process, part of the Al precursor do not take part in the structure formation of the zeolite and stay inside the material voids as alumina. This means that it is necessary to differentiate between framework and extra-framework Al, to have an accurate estimation

of BA. In this work we used an ammonia temperature programmed desorption process developed by Di Iorio *et al* to quantify framework Al and the number of BA sites in H-SSZ-13 samples [65].

After obtaining the NH_3 desorption profiles for H-SSZ-13 with Si/Al 4.5 and 25, a quantification process was carried out. First, the total NH_3 desorbed was quantified from the m/z = 17 MSD signal after subtraction of the contributing fragments of water (also m/z = 17), which appears in constant proportion to the m/z = 18 MSD signal for its parent ion. Following, NH_3 peak intensity was normalized using the signal of an Ar pulse as standard and the water content was subtracted thereafter performed thermogravimetric analysis (TGA) before and after the saturation process. The now free from external contributions NH_3 peak was used to quantify the amount of BA and subsequently to estimate the amount of Al in the framework. Finally, results from a comparison between the number of Al atoms obtained by this method and by atomic absorption are presented in Table 2.4, according to which, in both Si/Al = 25 and 4.5, approximately 90% of the total amount of Al is part of their framework.

Table 2.4: NH_3-TPD results

Sample	NH_3/Al
ZCuOH	0.9 ± 0.1
Z2Cu	0.9 ± 0.1

2.4.2 SCR Kinetics over sulfated Cu-SSZ-13

2.4.2.1 Diffusional limitations during SCR

Every kinetic experiment must be free from mass transfer limitations to assure correct catalytic activity data. For this purpose, the Koros-Nowak experimental criterion modified by Madon and Boudart was used [84, 85]. According to this theory, the turnover rate (TOR) or the moles reacted per second per surface mole must not change as the concentration of the active material changes. For the case of SCR over Cu-SSZ-13, the plot of TOR vs concentration of Cu should present a constant trend in the region where Madon-Boudart criterion is accomplished [35].

The selected copper content for both ZCuOH and Z2Cu (see Table 2.1) and the total gas flow ($\sim$1200 mL min^{-1}) for SCR kinetic experiments were defined considering a region where the standard SCR rate increases constantly with Cu wt% and therefore Madon-Boudart criteria was ensured, Figure 2.21.

On the other hand, as can be noticed in Figure 2.21, copper weight concentrations higher than 4.5% induce a reduction in the TOR. This is explained in the formation of copper
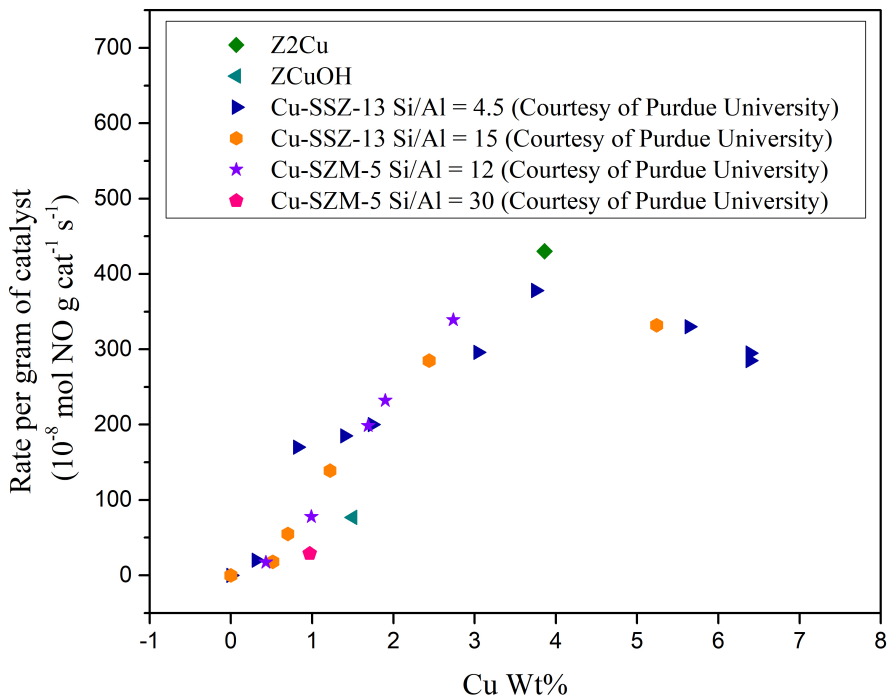
Figure 2.21: Standard SCR rates as function of copper content, obtained in this work and courtesy of Ribeiro research group from Purdue University, USA.

oxide clusters which are inactive for SCR reaction [86]. ZCuOH (Cu-SSZ-13 Si/Al = 25) and Z2Cu (Cu-SSZ-13 Si/Al = 4.5) catalysts used in this work presented lower Cu Wt% contents, which guaranteed their uniformity in copper species.

2.4.2.2 SCR kinetics

SCR reaction was studied over sulfated Cu-SSZ-13 (Z2Cu and ZCuOH) catalyst at the so-called standard conditions that simulate a real diesel engine exhaust, as described in Section 2.3.3. However, as shown in Figure 1.5, SCR presents a redox cycle reaction mechanism. Therefore, to have a better understanding of its changes (if occur) in the presence of sulfur, kinetic experiments were also performed on its oxidation half-cycle (here called oxidative SCR) by isolating it via an increase in the concentration of oxygen in the reactor feed gases from 10% to 60%, as done previously by Paolucci et al [42]. Results are presented in Tables 2.5 and 2.6.

Table 2.5: Kinetics results for standard and oxidative SCR over ZCuOH samples. Uncertainties: $E_{app} = \pm 6$, orders $= \pm 0.1$

Reaction	Item	ZCuOH	200CSO2 ZCuOH	400CSO2 ZCuOH
Standard SCR	S/Cu	0	0.3	0.85
	$E_{a,app}$ (kJ mol^{-1})	50	42	13
	TOR (10^{-8} mol NO gcat^{-1} s^{-1})	77	32	11
	O$_2$ order	0.3	0.6	0.9
	NO order	0.6	0.9	1.7
	NH$_3$ order	-0.4	-0.25	0.0
Oxidative SCR	S/Cu	0	0.3	0.85
	$E_{a,app}$ (kJ mol^{-1})	59	41	8
	TOR (10^{-8} mol NO gcat^{-1} s^{-1})	100	31	11
	O$_2$ order	0.1	0.6	0.9
	NO order	0.9	1.2	2.0
	NH$_3$ order	-0.6	-0.13	0.0

Table 2.6: Kinetics results for standard and oxidative SCR over Z2Cu samples. Uncertainties: $E_{app} = \pm 6$, orders $= \pm 0.1$

Reaction	Item	Z2Cu	200CSO2 Z2Cu	400CSO2 Z2Cu
Standard SCR	S/Cu	0	0.19	0.4
	$E_{a,app}$ (kJ mol^{-1})	58	60	56
	Rate (10^{-8} mol NO gcat^{-1} s^{-1})	430	280	165
	O$_2$ order	0.3	0.3	0.3
	NO order	0.9	0.8	0.8
	NH$_3$ order	0.0	-0.1	-0.1
Oxidative SCR	S:Cu	0	0.19	0.4
	$E_{a,app}$ (kJ mol^{-1})	54	64	65
	Rate (10^{-8} mol NO gcat^{-1} s^{-1})	563	319	241
	O$_2$ order	0.0	0.2	0.0
	NO order	0.9	1.0	1.0
	NH$_3$ order	0.0	-0.2	-0.2

To facilitate the interpretation of kinetic results, data from Tables 2.5 and 2.6 were arranged as presented in Figures 2.22 and 2.23, Where it is evident that SCR turn-over rates declined for ZCuOH and Z2Cu as result of increasing the amount of sulfur, indicating that both Cu^{2+} and [CuOH]$^{1+}$ active sites in Cu-SSZ-13 were poisoned by sulfur, then lost significantly their catalytic activity for SCR.
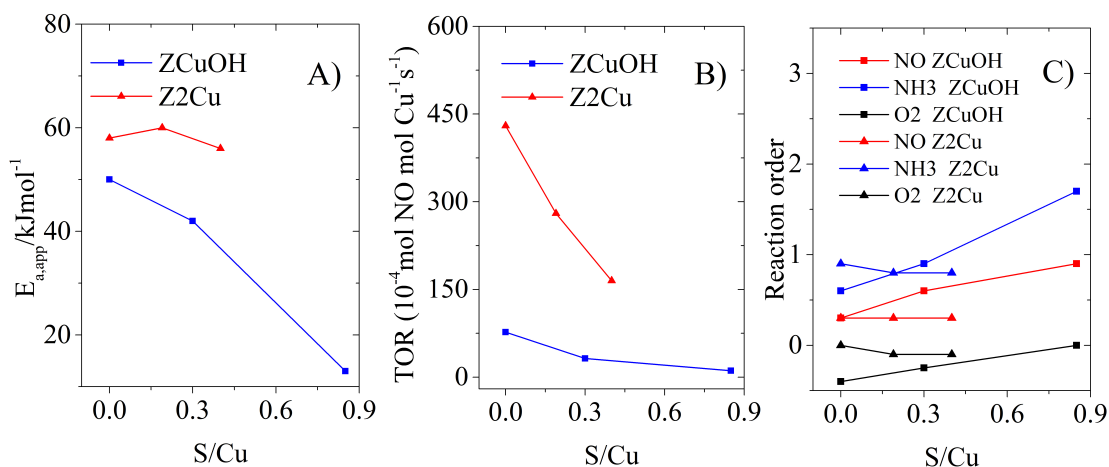
Figure 2.22: Kinetics results for standard SCR over ZCuOH and Z2Cu (Apparent activation energy (A), TOR (B), reaction order (C)), as function of sulfur content
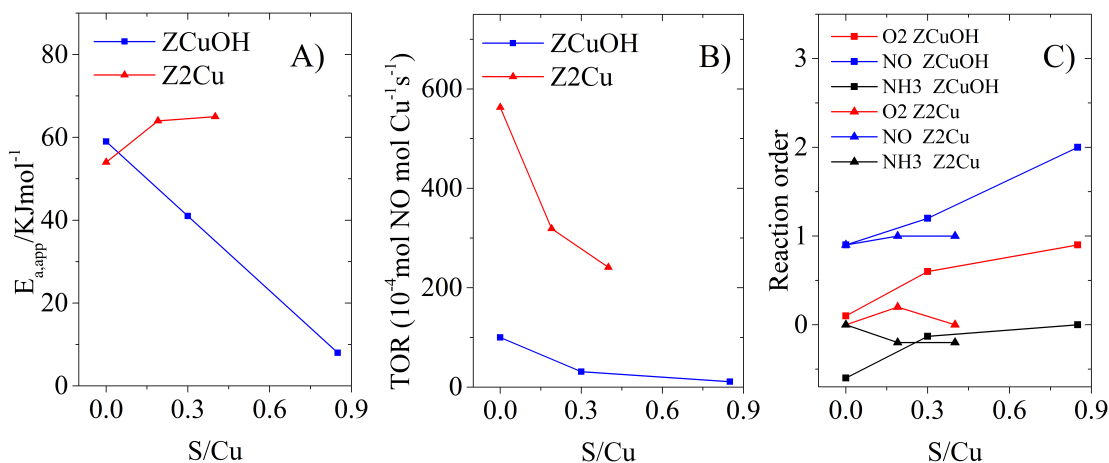
Figure 2.23: Kinetics results for oxidating SCR over ZCuOH and Z2Cu (Apparent activation energy (A), TOR (B), reaction order (C)), as function of sulfur content

Changes in SCR mechanism caused by the presence of sulfur were also evidenced when estimating the apparent activation energy ($E_{a,app}$) for unsulfated and sulfated Z2Cu and ZCuOH at standard and oxidative conditions, using Arrhenius plots (Equation (2.11)). To illustrate this, Figure 2.24 shows the Arrhenius plot for standard SCR over ZCuOH and Z2Cu. The reliability of our results for ($E_{a,app}$) from unsulfated samples was confirmed by comparison with previously reported values [35, 42, 87], Table 2.7. In figures 2.22 and 2.23 it is observed that $E_{a,app}$ changes in sulfated ZCuOH samples during both standard and oxidating SCR, while in Z2Cu samples no significant changes were observed, which suggests different poisoning effect of sulfur depending on the active site.

$$k_{\text{eff}} = A_0 \exp\left(\frac{-E_{\text{a,app}}}{RT}\right) \tag{2.11}$$
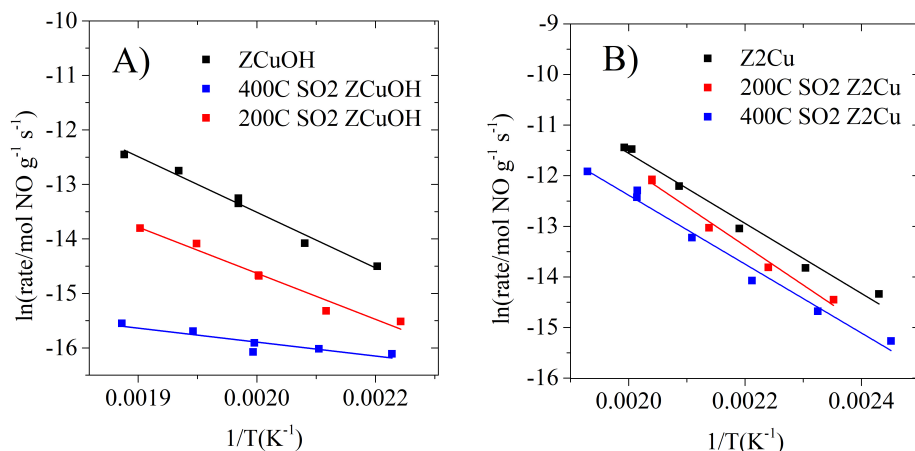
Figure 2.24: Arrhenius plot for standard SCR over unsulfated and sulfated ZCuOH (A) and Z2Cu (B)

Table 2.7: Apparent activation energy for SCR over Cu-SSZ-13 from literature reports.

Authors	Si/Al	Cu/Al	$E_{\text{a,app}}$ (kJ mol^{-1})
Bates et al [35, 42].	4.5	0.09	64
Albarracín-Caballero et al [87].	15	0.37	62
This work (Table 2.6)	4.5	0.21	58

Note: $E_{\text{a,app}}$ obtained with the same gas compositions used in this work (320 ppm NO, 320 ppm NH$_3$, 8% CO$_2$, 10% O$_2$).

Reactions orders for NH$_3$, NO and O$_2$ were obtained using the initial rates method in a power law reaction rate expression used elsewhere, Equation (2.12) [35, 87, 41]. As the concentration of sulfur increased, in ZCuOH, both standard and oxidative SCR underwent an increment in the reaction orders for O$_2$ and NO. Although this is consistent with a higher relevancy of NO and NH$_3$ oxidation reactions, due to the complexity of side reactions occurring along with SCR, kinetics data do not provide conclusive information to identify a sulfur promoted reaction pathway in ZCuOH. For the case of Z2Cu, similar as $E_{\text{a,app}}$, no change were observed in reaction orders, confirming a different poisoning effect of sulfur in this active site.

$$R_{\text{SCR}} = K[\text{NO}]^{\alpha}[\text{NH}_3]^{\beta}[\text{O}_2]^{\gamma} \tag{2.12}$$

The different behavior of $[CuOH]^{1+}$ and Cu^{2+} active sites in the presence of sulfur observed in our kinetic experiments have also been identified through *in-situ* diffuse reflectance infrared spectroscopy (DRIFTS). Authors have reported that sulfur has a severe poisoning interaction with $[CuOH]^{1+}$ active sites while with Cu^{2+} sites a sulfur-site interaction needs the presence of ammonia (to form ammonium sulfate) and is less likely to occur [50, 38].

According to literature information and our own kinetic results, the poisoning of Cu^{2+} sites by sulfur is in most of its extent the result of a site-blocking effect caused by the formation of bulky species instead of a direct sulfur-active site interaction (or at least this interaction is less severe as in the case of $[CuOH]^{1+}$ sites). Reported BET results show a decreased in Cu-SSZ-13 surface area after SO_2 treatment under SCR conditions at temperatures from $100°C$ to $600°C$ [47]. The nature of sulfur-active site interaction and species formation is discussed in Sections 2.4.3 and 2.4.4.

Kinetics results for oxidative SCR showed tendencies similar to those observed during standard SCR when the concentration of sulfur on the catalyst was incremented. Nevertheless, it was observed a slight increase in the activation energy of Z2Cu (Figure 2.23), suggesting a mild interaction between Cu^{2+} sites and sulfur in SCR oxidation half-cycle.

It is important to mention that we did not perform studies to determine changes in absorption energies of SCR species onto Z2Cu and ZCuOH, caused by sulfation. Therefore, we could not include their contribution in apparent activation energy that we reported in Tables 2.5 and 2.5.

2.4.3   UV-Vis-NIR

2.4.3.1   O$_2$ activation of Cu-SSZ-13 and the presence of copper dimers

At the beginning of this research there was not a fully understanding of how the formation of copper-oxo dimers in Cu-SSZ-13 after O_2 activation were involved in the oxidation half cycle of SCR reaction. To approach this lack of information and later analyze its relationship with the presence of sulfur, we performed UV-Vis-NIR measurements after treating unsulfated Z2Cu and ZCuOH with a flow of O_2 at 300 °C in a difussive reflectance *in-situ* cell. However, subsequently Paolucci et al [40] reported that in fact, transient copper dimers are formed during SCR mechanism over Cu-SSZ-14, but they appear after NH_3 assisted migration of $Cu^{1+}(NH_3)_2$ species. In spite of this recently reported mechanism, it was still possible to use our O_2 activation experiments, not as a way of understanding changes in SCR mechanism, but to link the presence (or absence) of copper dimers with changes in the coordination of Cu-SSZ-13 active sites due to the presence of sulfur.

O_2 activation have been used in Cu supported zeolites as Cu-SSZ-13, Cu-beta and Cu-ZSM-5 with the aim of causing the disappearance of water signals in the NIR region and increasing the intensity of bands from d-d transitions and ligand-to-metal charge transfer (LMCT) regions in UV-Vis-NIR spectra. Which is possible by a stronger interaction of Cu^{2+} species with framework oxygen atoms [88] after the removal of water molecules from

the sample. Figure 2.25 illustrates how O_2 activation enhances UV-Vis-NIR spectra for unsulfated samples.
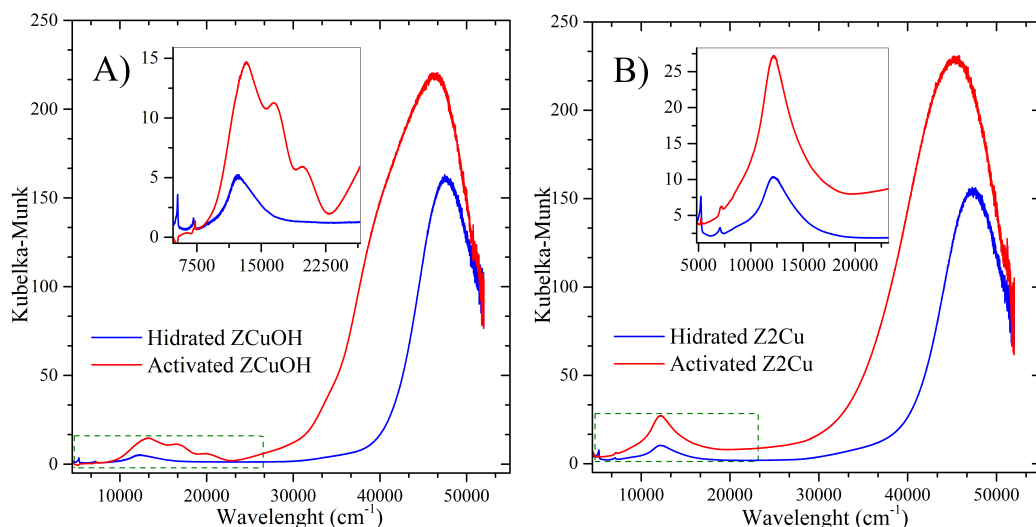
Figure 2.25: UV-Vis-NIR results for unsulfated ZCuOH (A) and Z2Cu (B) before and after O_2 activation

Our interest now consist in assigning the bands in UV-Vis-NIR spectra of ZCuOH and Z2Cu formed after O_2 activation, and to identify which of them are related to the formation of Cu dimers. In Figure 2.25 A) and B), a feature at 5260 cm^{-1} ascribed to physisorbed water [89], was nearly dissipated after O_2 activation for both Z2Cu and ZCuOH. Even though this indicates that the catalysts were not fully dehydrated, we considered inadequate to increase the activation temperature until obtaining their fully dehydration, because this could had caused the desorption of sulfur species in sulfated samples. A small band observed at 7150 cm^{-1} corresponds to an overtone of Brönsted acidity related hydroxyl groups [68], which intensity reasonably did not change after O_2 activation. A broad band centered at 12000 cm^{-1}, observed in hydrated samples, is reported to be associated to d-d transitions occurring in octahedral H_2O-Cu complexes [88].

A particular behavior was observed in O_2 activated ZCuOH UV-Vis-NIR espectrum, Figure 2.25 A). 12000 cm^{-1} d-d transitions band was decomposed in three different bands (13230, 16500 and 19700 cm^{-1}). This is caused possibly because 12000 cm^{-1} band corresponds to the Jahn-Teller deformation of several d-d transitions [88]. Giordanino *et al* [88] and Albarracín-Caballero *et al* [87] observed these three bands along with a fourth one at 11100 cm^{-1}, while Ipek *et al* [90] obtained the same results of this work. The absence of 11100 cm^{-1} band in our case can be attributed to the lack of total dehydration after O_2 activation at 300°C. As a matter of fact, Ipek *et al* [90] studied the effect of O_2 activation temperature in DR-UV-Vis and were able to identify new bands at 22000, 29500 and 35000 cm^{-1} after activation at 450°C. Bands at 16500 and 19700 cm^{-1} observed in Figure 2.25 A) can be related to the formation of divalent copper complexes charge compensated by a nearby aluminum [88, 90]. Giordanino *et al* [88] assigned bent $\mu(\eta^2:\eta^2)$ peroxo-dicopper divalent

41

dimers to features in the range of 17000-19700 cm^{-1}, while Ipek *et al* [90] and Woertink *et al* [91] estimated by DFT calculations features from several trivalent and divalent Cu dimers, Table 2.8. Paolucci *et al* [40] calculated by DFT that the more stable copper dimers in Cu-SSZ-13 are, in decreasing order, bis(μ-oxo) dicopper, bent $\mu(\eta^2{:}\eta^2)$ peroxo dicopper and *trans-μ-1,2* peroxo dicopper, which indicates along with features observed in Figure 2.25 A) that O$_2$ activated ZCuOH most probably presented a mixture of the latter three Cu dimeric species.

Table 2.8: UV-Vis-NIR bands for copper dimers [90, 91]

Copper species	Structure	Bands [Wavenumber (cm^{-1})]
Trans-μ-1,2-peroxo dicopper (II)		22980 19803 16260
μ-($\eta^2{:}\eta^2$) peroxo dicopper (II) bent		18200 20400 - 23800 27800
μ-($\eta^2{:}\eta^2$) peroxo dicopper (II) planar		17100 -19800 27300 - 29600
Bis(μ-oxo) dicopper (III)		22300 - 25000 30800 - 32700
η^2-superoxo dicopper (II)		10200 14300 22100 26100

In Figure 2.25 B) it is observed that even though O$_2$ activation increases intensity in 12000 (cm^{-1}) band, Z2Cu sample did not present d-d transitions features related to formation of Cu dimers. This implies that in the absence of the mobility provided by NH$_3$, Cu dimers are only formed in sufficiently close [CuOH]$^{1+}$ active sites. Also, mobilization of Cu^{1+}(NH$_3$)$_2$ species in Z2Cu samples is a *sine qua non* condition for the formation of copper dimers from Cu^{2+} active sites [40].

Ligand-to-metal charge transfer (LMCT) region should present a band in the range of 27800 - 32700 cm^{-1} characteristic of the presence of bent $\mu(\eta^2{:}\eta^2)$ peroxo dicopper and Bis(μ-oxo) dicopper dimeric species, according to experimental and DFT calculations results from Ipek *et al* [90]. In Figure 2.25 it is observed that for Z2Cu, although LMCT region presented

higher intensity after O_2 activation, no evidences of new bands were observed. For the case of ZCuOH, is it visible a change in the shape of LMCT band but unfortunately the presence of small amounts of water did not allow a complete formation of bands.

2.4.3.2 *Ex-situ* UV-Vis-NIR on sulfated Cu-SSZ-13 after O_2 activation
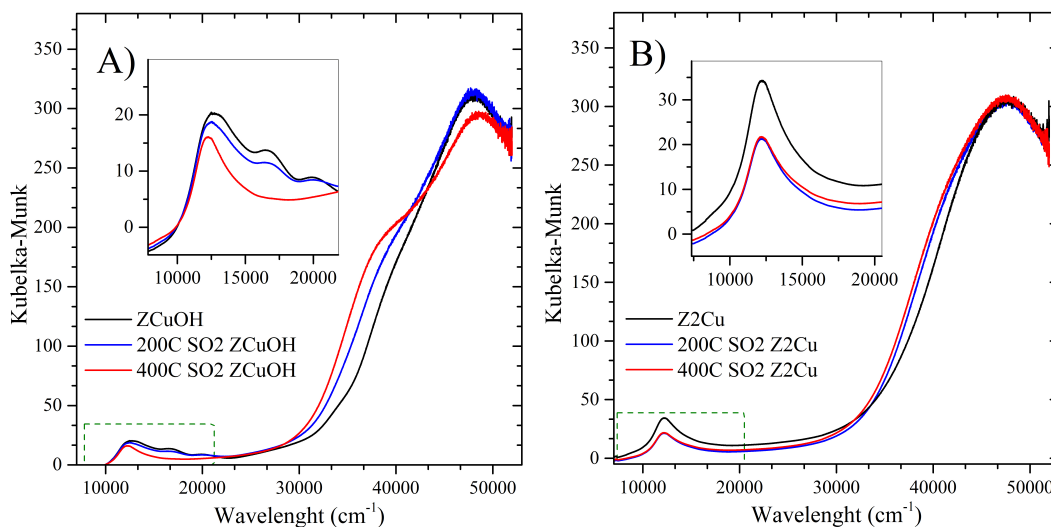
Figure 2.26: UV-Vis-NIR spectra of O_2 activated ZCuOH and Z2Cu

Ex-situ UV-Vis-NIR expectra for unsulfated and sulfated ZCuOH and Z2Cu samples were measured at ambient conditions after oxygen activation, for identifying changes in $[CuOH]^{1+}$ and Cu^{2+} active sites caused by the presence of sulfur. In Section 2.3.1 it was described that both Z2Cu and ZCuOH samples were sulfated at two different temperatures, 200 and 400°C, obtaining higher concentrations of sulfur in the samples at 400°C (see Table 2.2). As presented in Section 2.4.3.1, a first aspect to be studied is the effect of sulfur concentration on the formation of copper dimers. In Figure 2.26 A) it is observed that the presence of sulfur causes the dissipation of 16500 and 19700 cm^{-1} bands, implying that sulfur species bond to $[CuOH]^{1+}$ sites blocked the formation of copper dimers. This effect is more noticeable as the concentration of sulfur increases, Cu dimers d-d transitions bands were completely absent in spectrum from ZCuOH sample saturated with SO_2 at 400°C. Moreover, as discussed in Section 2.4.3.1, there are not evidences of Cu dimers formation in O_2 activated Z2Cu, hence no discussion can be made about this aspect from Figure 2.26 B). Furthermore, lower intensity of 12000 cm^{-1} d-d transitions band in both Z2Cu and ZCuOH after sulfation denote less Cu sites available for SCR reaction, which explains the decrease in reaction rates from kinetic experiments at higher concentrations of sulfur (Section 2.4.2.2).

In Figure 2.26 it is also noticeable a new LMCT band in sulfated ZCuOH (38000 cm^{-1}) and Z2Cu (39000 cm^{-1}), with considerable more prominence in ZCuOH, which may be related to sulfur-Cu bonds. Zhang *et al* [92] observed a similar sulfur-metal band at 35100 cm^{-1} during a study about the absorption of sulfur species from dibenzothiophene on Zn

and Zn-Cu supported Y zeolite. This new sulfur-related band suggests that sulfur showed a direct interaction with $[CuOH]^{1+}$ sites while it was slightly perceived by Cu^{2+} sites. In fact, the presence of 39000 cm^{-1} band on Z2Cu may be related to the presence of small amounts of $[CuOH]^{1+}$ sites that this sample presented. Linking these results with kinetics experiments (Tables 2.5 and 2.6), changes in apparent activation energies were observed in SCR over $[CuOH]^{1+}$ while sulfur-Cu interaction (from UV-Vis-NIR experiments) was so weak in Cu^{2+} sites that it did not cause measurable changes in $E_{a,app}$ during SCR over Cu^{2+} site.

Li *et al* [52] used density functional theory (DFT) calculations to identify intermediate sulfur-Cu species and *ab-initio* molecular dynamics (AIMD) to examine molecular configurations at finite temperatures. Then, obtained UV-Vis spectra for ZCuOH and Z2Cu by time-dependent DFT calculations, Figure 2.27. Though in terms of position and intensity of the features, these results are very different from our experimental results, presented in Figure 2.25; when comparing them qualitatively, spectra presented several similarities: a deformation of Cu-dimers related bands in ZCuOH, a decrease in the intensity of d-d transition band in Z2Cu and formation of a new band in the LMCT region for both ZCuOH and Z2Cu.
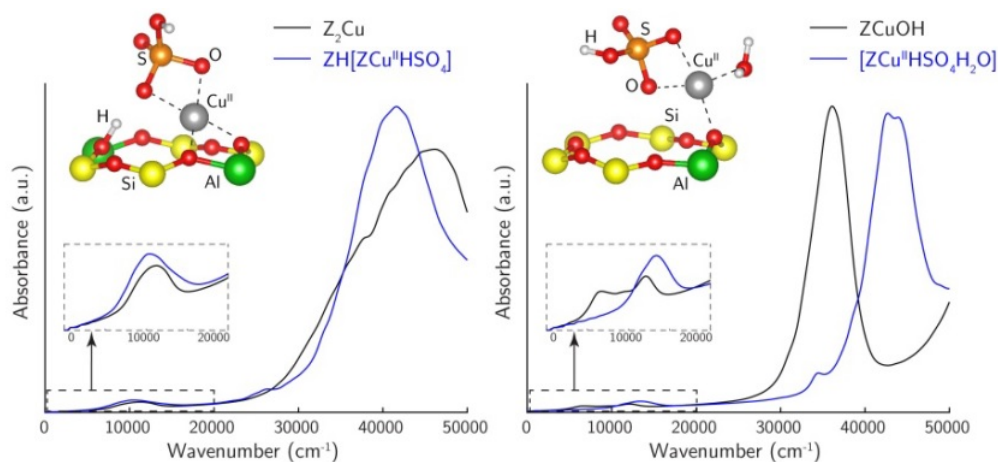
Figure 2.27: Simulated UV-Vis spectra of ZCuOH and Z2Cu obtained via DFT calculations by Li *et al* [52].

2.4.3.3 *In-situ* UV-Vis-NIR on sulfated Cu-SSZ-13 after NH$_3$ saturation

Up to this point, we have studied the formation of sulfur species in Cu-SSZ-13 only in the presence of O_2. However, the remaining SCR gases may also change the chemistry inside the catalyst, thus probably influencing the formation of other sulfur intermediate species. Ammonia is particularly significant as several authors have reported the formation of sulfur-NH$_3$ salts in Cu supported zeolites [38, 50, 93]. In this section, *in-situ* UV-Vis-NIR is used to study the effect of ammonia in the formation of sulfur species in ZCuOH and Z2Cu at 25 and 200°C.

In both ZCuOH and Z2Cu, the presence of sulfur and NH_3 (Figures 2.29 and 2.30) caused the formation of a shoulder at 17000 cm^{-1} from 12000 cm^{-1} d-d transitions band, which as discussed in Section 2.4.3.4, corresponded mainly to the formation of $Cu(NO_3)_4SO_4$. Since 17000 cm^{-1} feature is observed in both sulfated and unsulfated samples (Figures 2.28, 2.29 and 2.30), we propose that it is also related to the formation of Cu-NH_3 species. In Figure 2.28 A), it is observed that NH_3 adsorption caused a shift to higher wavenumbers in LMCT, in opposite to sulfation (Section 2.4.3.2), in which case a shift to lower wavenumbers was observed. This effect is more evident in 25°C NH_3 ZCuOH, indicating higher ammonia absorption in $[CuOH]^{1+}$ at lower temperatures.
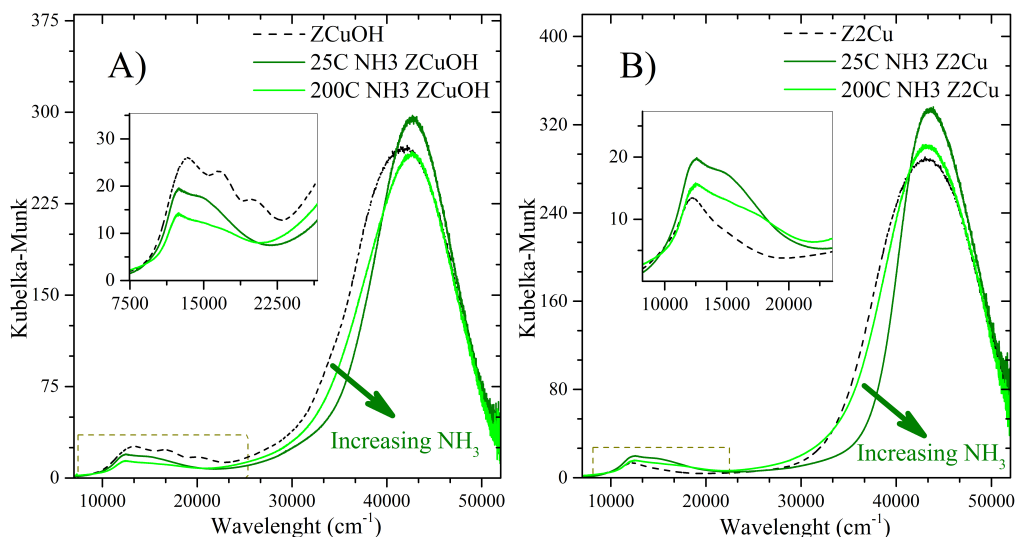
Figure 2.28: UV-Vis-NIR spectra of NH_3 saturated ZCuOH (A) and Z2Cu (B)

Interestingly, LMCT band centered at 43000 cm^{-1} in sulfated Z2Cu samples after NH_3 adsorption at 25°C (Figure 2.29 B)) presented a shift to higher wavenumber, as observed in unsulfated Z2Cu (Figure 2.28 B)), whereas in sulfated ZCuOH (Figure 2.28 A)) no shift was observed (or at least it was very small). This findings suggest that after sulfation, Cu^{2+} retained most of its capacity for absorbing NH_3, while adsorption of NH_3 ZCuOH was greatly reduced. This is corroborated by Jangjou *et al* [50] *in-situ* DRIFTS characterization of NH_3 + SO_2 + O_2 treated ZCuOH and Z2Cu. They found that ZCuOH presented lower NH_3 adsorption whilst Z2Cu maintained its NH_3 adsorption capacity. Nonetheless, they observed a high formation of $(NO_3)_4SO_4$ only on Z2Cu, while in our case, since d-d transitions band at 1700 cm^{-1} was very similar in ZCuOH and Z2Cu, we conclude that $(NO_3)_4SO_4$ is formed in both cases.
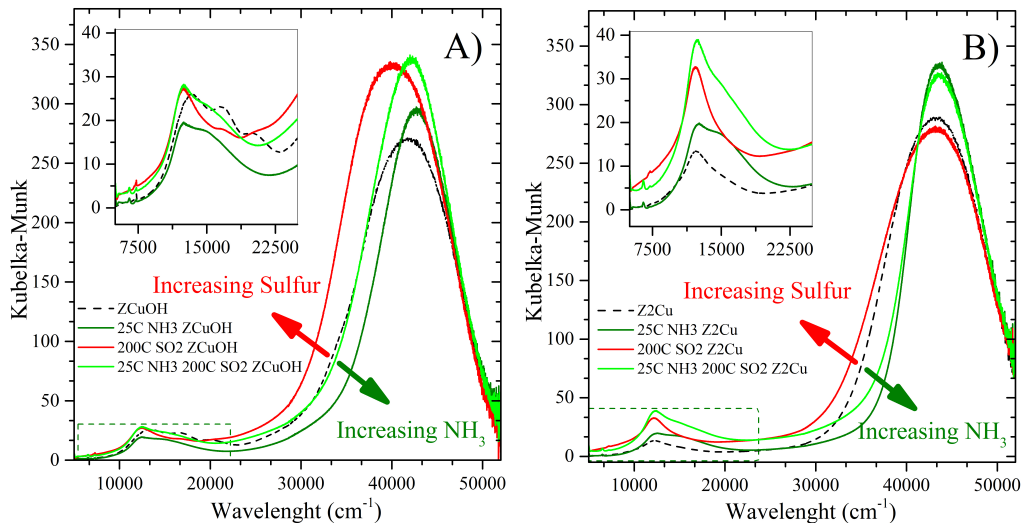
Figure 2.29: UV-Vis-NIR spectra of sulfated ZCuOH (A) and Z2Cu (B), after saturated with NH_3 at 25°C

Sulfated ZCuOH and Z2Cu after saturation with ammonia at 200°C (Figure 2.30) presented the same behavior in the d-d transitions region observed when saturated with ammonia at 25°C (Figure 2.29). A new feature was observed at 17000 cm^{-1}, as discussed previously, related to the formation of $Cu(NH_3)_4SO_4$ and $(NO_3)_4SO_4$ species. LMCT transition region presented conflicting results. LMCT band centered at 43000 cm^{-1} shifted to the left, which according to Figure 2.29 would indicate that there was not ammonia adsorption but the presence of 17000 cm^{-1} band indicates the opposite.
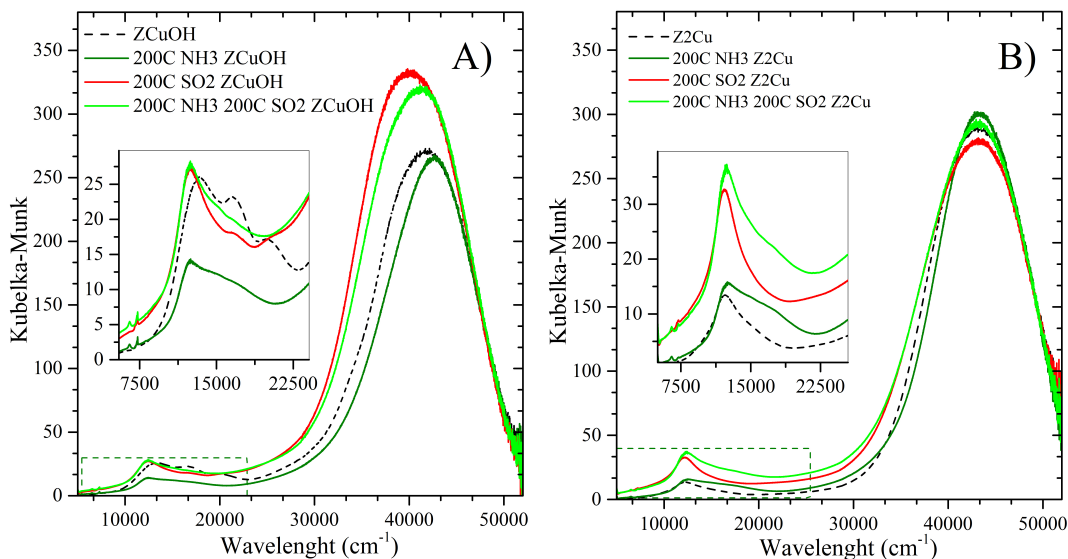
Figure 2.30: UV-Vis-NIR spectra of sulfated ZCuOH (A) and Z2Cu (B), after saturated with NH_3 at 200°C

2.4.3.4 *Ex-situ* UV-Vis-NIR on sulfur and ammonia containing Cu salts

Several NH_3, sulfur and copper containing salts were analyzed by UV-Vis-NIR to validate that the bands in d-d transitions for sulfated and ammonia saturated ZCuOH and Z2Cu samples (observed in Figures 2.28, 2.29 and 2.30), certainly correspond to sulfur-Cu and NH_3-Cu interactions. The salts studied are listed in Table 2.9. In Figure 2.31 it is observed that the d-d transitions band at 17000 cm^{-1} in $Cu(NH_3)_4SO_4$ salt was also observed in sulfated and NH_3 saturated ZCuOH and Z2Cu (Figures 2.29, 2.30), confirming that this band corresponds to Cu interactions with NH_3 and SO_4. Also, a band at 12000 cm^{-1} from $CuSO_4.5H_2O$ salt in Figure 2.31 was located in the same wavenumber as Cu-O_2 interactions observed in dehydrated ZCuOH and Z2Cu (Figure 2.26). As consequence of this, the identification of evidences from sulfur-Cu interactions could be hindered. It should be mentioned that LMCT band in Cu-SSZ-13 includes the interaction between Cu sites and the CHA structure, therefore, is not adequate to make comparison with Cu salts as carried out for the d-d transitions bands previously.

Table 2.9: Copper salts analyzed by UV-Vis-NIR

Salt	Purity (%)	Brand
$Cu(NH_3)_4SO_4.H_2O$	98.00	Sigma-Aldrich
$CuSO_4.5H_2O$	99.99	Sigma-Aldrich
$(NH_4)_2SO_4$	99.99	Sigma-Aldrich
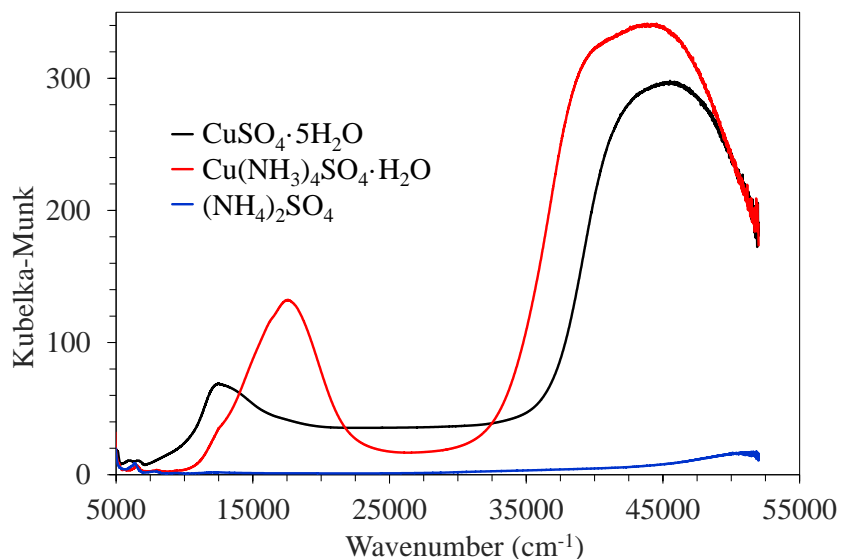
Figure 2.31: UV-Vis-NIR spectra for Cu salts

2.4.4 *Operando* XAS

2.4.4.1 *Operando* Cu K-edge XAS on Cu-SSZ-13

The use of XAS for identifying the oxidation state and the local environment of copper during operando SCR have been reported by several authors [35, 73, 86, 94]. According to previous results, Cu K-edge XANES spectrum is expected to have two features, one at 8.9806 keV related to the presence of Cu^{1+} species and other from 8.9837 to 8.9885 keV due to the presence of Cu^{2+} species. The ratio between oxidation states in the copper species depends on the reducing or oxidating condition of its environment. In item (A) from Figures 2.32 and 2.33 is observed that unsulfated ZCuOH and Z2Cu at operando SCR conditions presented a mixture of Cu^{1+} and Cu^{2+} species, typical of the redox nature of SCR reported previously [42, 40, 41]. Also, the oxidation environment in O_2 samples caused that all Cu species presented an oxidation state of 2+, evidenced in the absence of 8.9806 keV feature. In item (C) from Figures 2.32 and 2.33 is observed that spectra from the reducing SCR half-cycle (simulated in this work by flowing NO and NH_3 through the sample), showed only Cu^{1+} species as expected from the reduction of copper. As the intensity of XANES peaks is proportional to the amount of the studied species, a decrease in the intensity of Cu^{1+} in sulfated ZCuOH and Z2Cu (~30% and ~50% for Z-CuOH and Cu^{2+}, respectively), can be related to a lower ability of copper active sites to be reduced, which in consequence implies that the species tha causes the reduction of Cu active sites (NH_3 and or NO), were not able to be adsorbed; explaining the lower NO consumption rates in sulfated samples observed in kinetic experiments, Section 2.4.2.2.

Operando SCR EXAFS spectra helps to corroborate that sulfur has a different interaction with the active sites in ZCuOH and Z2Cu. In item (B) from Figures 2.32 and 2.33, it is observed that the presence of sulfur caused changes in the first coordination shell in ZCuOH, while it changes the second coordination shell in Z2Cu, indicating that sulfur has a more direct interaction with $[CuOH]^{1+}$ active sites, as observed in *in-situ* UV-Vis-NIR results, Section 2.4.3. According to EXAFS from *in-situ* reducing SCR in item (D) from Figures 2.32 and 2.33, sulfur causes changes in the first coordination shell of both ZCuOH and Z2Cu. To explain this finding, we suggest that oxygen may had played a role in avoiding the interaction between sulfur and the copper sites observed in *operando* SCR (item (C) from Figures 2.32 and 2.33). First and second coordination shells where centered at 1.5Å and 2.5Å, respectively, which is consistent with previous reports [41].
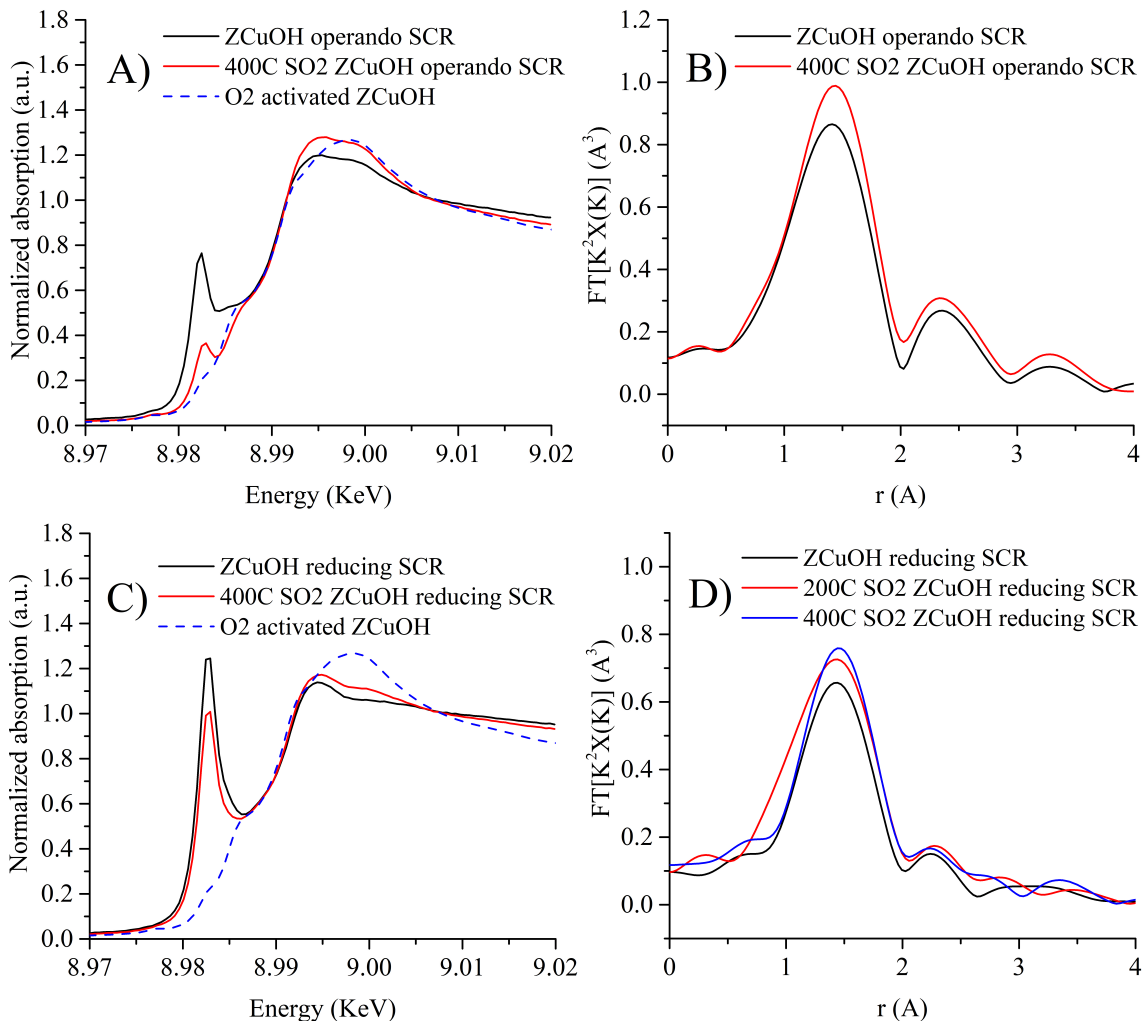
Figure 2.32: XAS results for Z-CuOH at *operando* standard SCR and at *in-situ* reducing SCR.
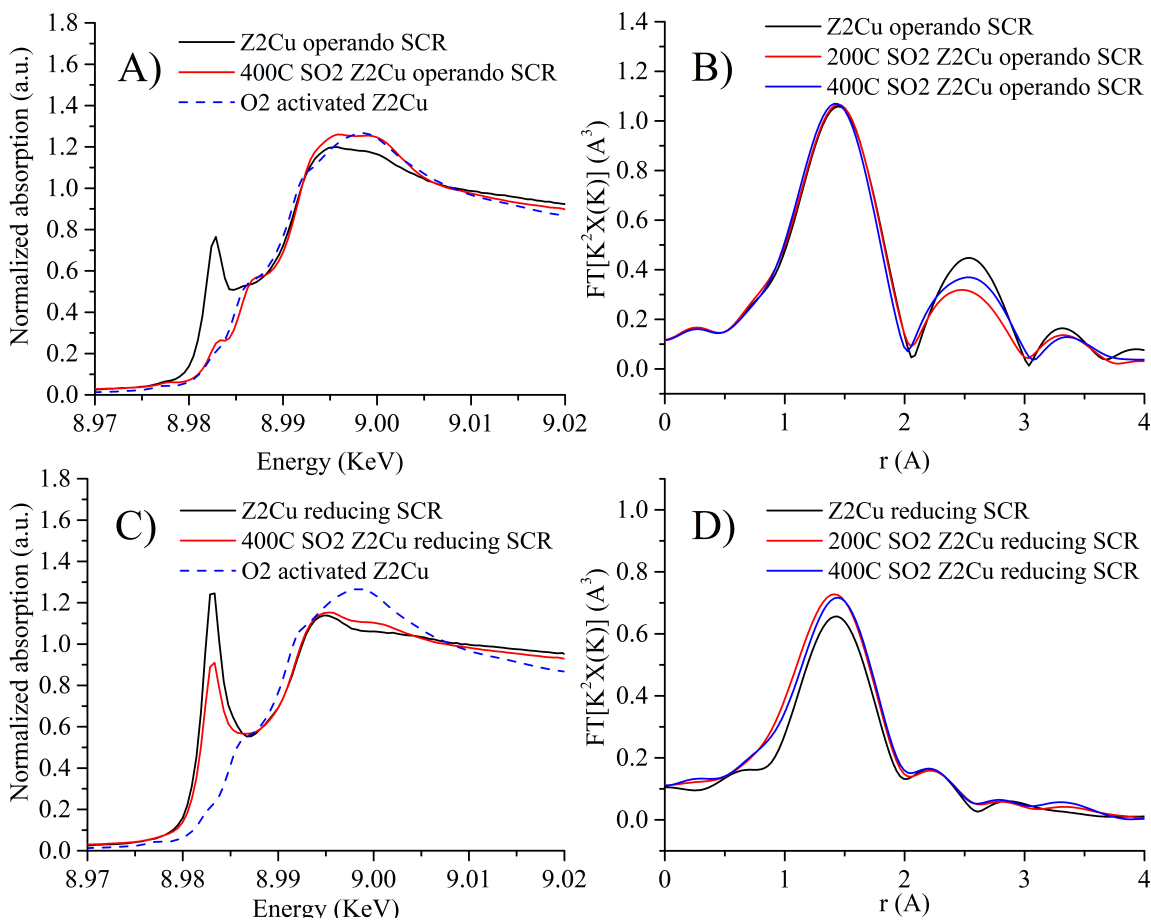
Figure 2.33: XAS results for Z2Cu at *operando* standard SCR and at *in-situ* reducing SCR.

Finally, gas compositions collected during SCR *operando* XAS caracterizations were used to calculate NO consumption rate normalized by the number of active sites. These results were compared to those obtained previously during SCR kinetic experiments (Section 2.4.2.2), Figure 2.34 shows the results from ZCuOH. It is observed that SCR reaction rates from *operando* XAS and from kinetics experiments, even though they were obtained at different laboratories and using different reaction setups, presented similar results. This confirmed that XAS caracterizations were carried out under kinetically-limited conditions, therefore free from mass and heat transfer artifacts.
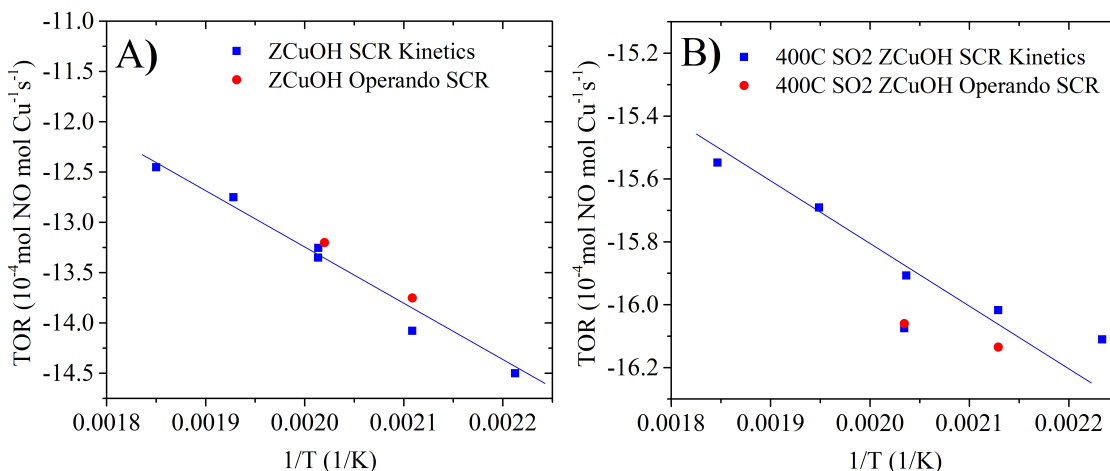
Figure 2.34: Arrhenius plot for ZCuOH, including data collected during SCR kinetics (Section 2.4.2.2) and during *operando* XAS.

2.4.4.2 *Ex-situ* Sulfur K-edge XAS on sulfated Cu-SSZ-13 and several copper and sulfur salts
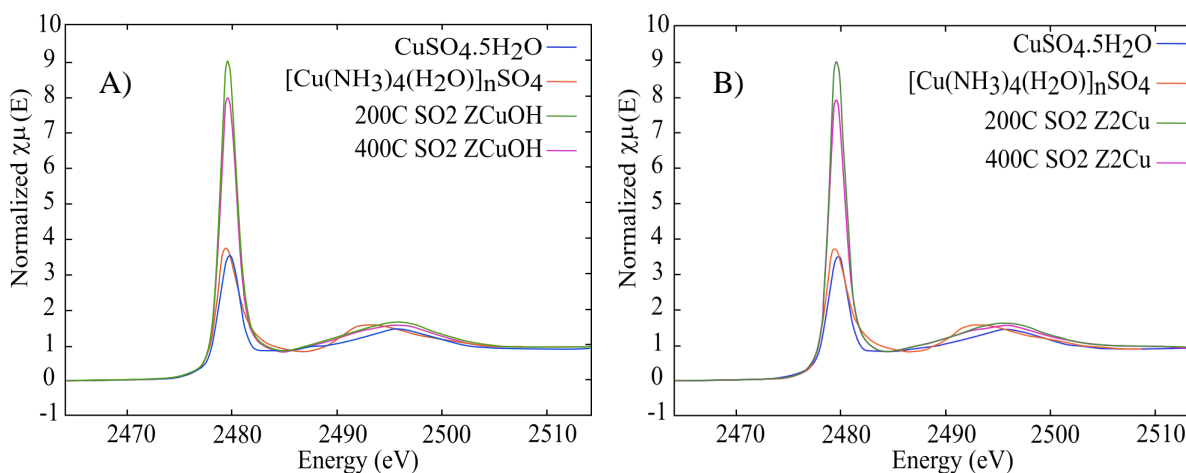
Figure 2.35: *Ex-situ* sulfur K-edge results for ZCuOH, Z2Cu and several salts

Ex-situ Sulfur K-edge XAS was performed to identify the oxidation state of the adsorbed sulfur species on sulfated Cu-SSZ-13. For comparison purposes, ammonium and SO_2 containing copper salts ($Cu(NH_3)_4SO_4 \cdot H_2O$ and $CuSO_4 \cdot 5H_2O$) were also analyzed. In Figure 2.35 it is observed that all samples presented a peak at 2.48 keV that corresponds to a sulfur oxidation state of 6+. This result indicates that sulfur oxides in ZCuOH and Z2Cu are adsorbed only in the form of SO_4^{2-}. Kim *et al* [95] found the same results in sulfated Cu-MOR, examined by XPS and Raman.

2.4.5 Sulfation mechanism

Summarizing the analysis of experimental results and considering reported information, in this section, sulfation mechanisms for ZCuOH and Z2Cu are proposed, starting from their dehidrated (O_2 activated) form, Figures 2.36 and 2.37.

2.4.5.1 Sulfation mechanism in ZCuOH

Given the nomenclature used in Figure 2.36, the sulfation mechanism of $[CuOH]^{1+}$ is presented as follows:

(A) NH_3 is adsorbed in $[CuOH]^{1+}$ sites from O_2 activated ZCuOH, forming mobile $Cu(OH)(NH_4^+)_3$ complexes [40].

(B) SCR redox cycle occurs as proposed by Paolucci *et al* [40]. This mechanism was further explained in Section 1.1.6.

(C) O_2 activated ZCuOH was saturated with dry SO_2 at 200°C and 400°C, as explained in Section 2.3.1. This caused the adsorption of sulfur oxides with an oxidation state of +6, as observed in sulfur K-edge XAS experiments in Section 2.4.4.2, and resulting in the formation of SO_4^{2+} species binded to $[CuOH]^{1+}$ sites, as observed in EXAFS experiments, Section 2.4.4. Sulfur-Cu complex formed in ZCuOH after dry SO_2 was proposed by Li *et al* [52] and corresponds to the most stable species obtained by DFT calculations.

(D) UV-Vis-NIR experiments in Section 2.4.3.3 showed that the adsorption of NH_3 (feature at 17000 cm^{-1}) in $[CuOH]^{1+}$ sites was not limited by the presence of sulfur. Also, $Cu(NH_3)_4SO_4.H_2O$ salt analyzed by UV-Vis-NIR in Section 2.3.4.2, presented the same feature at 17000 cm^{-1} observed in ZCuOH samples saturated with NH_3 and SO_2. Considering these results and the fact that sulfur was adsorbed as SO_4^{2+} (Section 2.4.4.2), we propose that a $Cu(NH_3)_3SO_4$ complex was formed in sulfated ZCuOH when NH_3 was adsorbed. Such complexes interrupted the formation of copper dimers, as evidenced in the UV-Vis-NIR analysis of sulfated ZCuOH after O_2 activation (Section 2.4.3.1). Subsequently, the absence of Cu dimers affected SCR redox-cycle, being manifested in a reduction in NO SCR rate during kinetic experiments (Section 2.3.3) and also identified in a decrease in the amount of Cu sites available for reacting, observed in XANES results (Section 2.4.4.1).
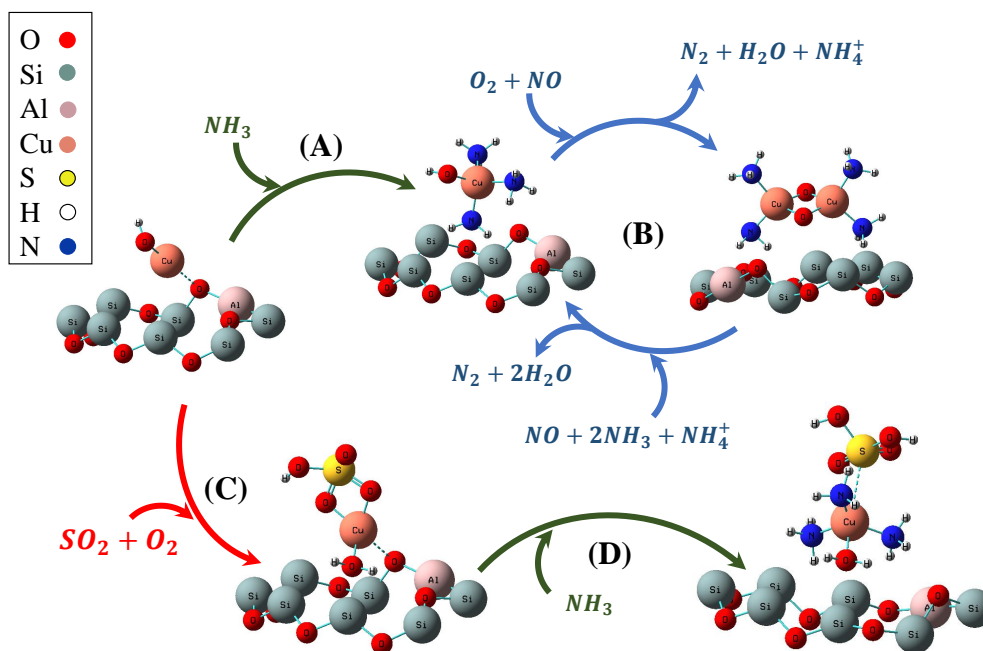
Figure 2.36: Proposed effect of sulfur on SCR mechanism over ZCuOH

2.4.5.2 Sulfation mechanism in Z2Cu

Given the nomenclature used in Figure 2.37, the sulfation mechanism of Cu^{2+} is presented as follows:

(A) NH_3 is adsorbed on Cu^{2+} sites from O_2 activated Z2Cu, forming mobile $Cu(NH_3^+)_4$ complexes [40].

(B) SCR redox cycle occurs as proposed by Paolucci *et al* [40]. This mechanism was further explained in Section 1.1.6.

(C) O_2 activated Z2Cu was saturated with dry SO_2 at 200°C and 400°C, as explained in Section 2.3.1. Then, Sulfur K-edge XAS experiments performed in Section 2.4.4.2, revealed that sulfur oxide species adsorbed in Z2Cu presented an oxidation state of +8 (SO_4^{2+}), but unlike ZCuOH, they were not binded directly to Cu^{2+} sites, as observed in UV-Vis-NIR experiments in Section 2.4.3 and EXAFS experiments in Section 2.4.4.1.

(D) For the decrease in NO SCR rate observed in sulfated Z2Cu during kinetic experiments (Section 2.3.3), we propose that sulfur species adsorbed nearby the active sites, made them less available for reacting. This suggestion is supported in a decrease of the number of Cu sites, observed in XANES results at *operando* SCR (Section 2.4.4.1). This can be corroborated with UV-Vis-NIR experiments on sulfated Z2Cu after O_2 activation (Section 2.4.3.1), since the lower intensity observed in the Cu d-d transitions band (at 12000 cm^{-1}) after sulfur saturation can be also related to a lower amount of Cu sites available for reaction. Although we were not able to corroborate by a surface area study the presence of adsorbed sulfur species near Cu sites, authors have reported evidences of site-blocking effect caused by such species in Cu-SSZ-13. Wijayanti *et al* [47]

observed a decrease in BET surface area and pore volume of Cu-SSZ-13 after exposing it to SO_2. Finally, it is important to mention that our kinetics results suggest that sulfur is not directly bonded to Cu^{2+} sites dissent from Li *et al* [52] DFT calculations that propose a direct interaction between Cu^{2+} sites and sulfur, Figure 2.27.
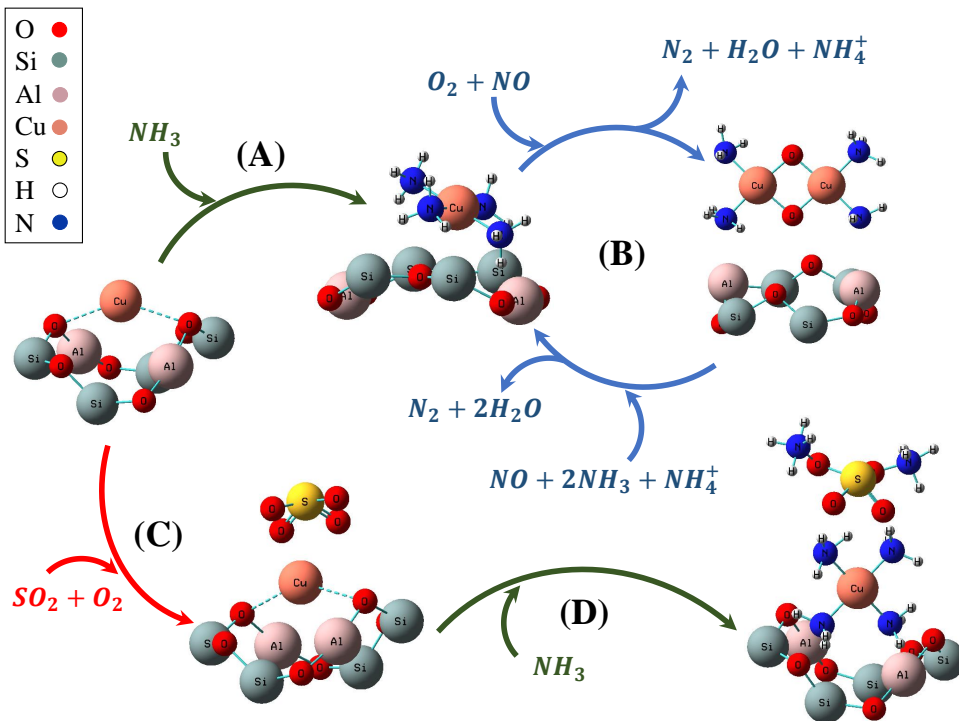
Figure 2.37: Proposed effect of sulfur on SCR mechanism over Z2Cu

2.5   Conclusions

Cu-SSZ-13 catalysts, differentiated in their type of active sites for SCR of NOx, were synthesized and saturated with sulfur. First, two parent H-SSZ-13 supports were synthesized with Si:Al molar ratios of 25 and 4.5 using a hydrothermal method. Subsequently, H-SSZ-13 materials were ion exchanged with solution of $Cu(NO_3)_2$, obtaining samples with ~100% $[CuOH]^{1+}$ (named ZCuOH) and ~80% Cu^{2+} (named Z2Cu), for Si:Al = 25 and 4.5, respectively. ZCuOH and Z2Cu were then saturated with dry SO_2 at 200°C and 400°C until obtaining a cumulative molar exposure of S:Cu = 5. The catalysts were characterized by AAS, ICP-OES, SEM, powder XRD and NH_3-TPD. AAS and ICP-OES were used to obtain molar compositions for Si, Al, Cu and S (ICP-OES). Powder XRD and SEM results indicated that no changes in the chabazite SSZ-13 structure occurred after sulfation at 200°C and 400°C. And, NH_3-TPD experiments confirmed that aluminum was mostly within SSZ-13 framework after synthesis.

Kinetic experiments were carried out to identify the effect of sulfur in the catalytic activity of Cu-SSZ-13 during standard SCR and oxidative (60% O_2) SCR conditions. It was observed that reaction rate normalized by the number of Cu active sites (TOR) for NO, decreased as the concentration of sulfur increased, in both standard and oxidative SCR, evidencing a poisoning effect. Furthermore, changes in the apparent activation energy ($E_{a,app}$) and in the reaction orders for NH_3, NO and O_2 in sulfated ZCuOH samples suggested that sulfur causes changes in SCR mechanism over $[CuOH]^{1+}$ sites. While in Z2Cu, the absence of changes in $E_{a,app}$ and reaction orders indicated that SCR mechanism for this active site did not present changes.

UV-Vis-NIR experiments were used to identify interactions between Cu active sites, NH_3 and sulfur species; and the implications of this interactions in SCR mechanism. First, UV-Vis-NIR spectrum collected on O_2 activated ZCuOH and Z2Cu showed that d-d transitions bands related to the formation of Cu dimers in ZCuOH (13230, 16500 and 19700 cm^{-1}) were dissipated in the presence of sulfur, indicating that $[CuOH]^{1+}$ sites lost their ability to form such dimers. Additionally, LMCT band centered at 43000 cm^{-1} presented sulfur-copper bonds related shoulders for sulfated ZCuOH (38000 cm^{-1}) and Z2Cu (39000 cm^{-1}), with considerable more prominence in ZCuOH. Moreover, *in-situ* UV-Vis-NIR spectrum collected while flowing NH_3 on ZCuOH and Z2Cu samples, showed that in both cases NH_3 adsorption ability was not lost due to the presence of sulfur. d-d transitions band at 17000 cm^{-1} observed in sulfur and ammonia containing copper salts, was also observed in unsulfated and sulfated ZCuOH and Z2Cu after NH_3 saturation, indicating that this band is related to Cu-NH_3 interactions.

XAS was used to determine sulfur-Cu interactions in ZCuOH and Z2Cu at reaction conditions and to identify the nature of adsorbed sulfur species. Cu K-edge XAS spectra were collected on ZCuOH and Z2Cu samples at *Operando* and reducing SCR conditions. XANES results showed that the number of reduced Cu species in ZCuOH and Z2Cu decreased ($\sim$30% and $\sim$50% in $[CuOH]^{1+}$ and Cu^{2+}, respectively) in the presence of sulfur. EXAFS characterizations at *Operando* SCR showed that ZCuOH fist coordination shell changed due to the presence of sulfur, while in Z2Cu this change was observed in the second coordination shell, indicating a more direct interaction of sulfur with $[CuOH]^{1+}$ sites. *Ex-situ* sulfur K-edge experiments performed on sulfated ZCuOH and Z2Cu and in several Cu salts containing NH_3 and sulfur. According to the results, sulfur was always adsorbed in ZCuOH and Z2Cu as SO_4^{2+}.

Finally, considering the most relevant findings from our experimental results and several reported information, sulfur poisoning mechanisms were proposed for $[CuOH]^{1+}$ and Cu^{2+} active sites during SCR. In $[CuOH]^{1+}$ mechanism sulfur formed a $Cu(SO_4)_2$ complex that in the presence of ammonia became $Cu(OH)(NH_3)_3SO_4$ intermediate species that, in turn, limited the adsorption of NO and the formation of Cu dimers, affecting SCR redox cycle. For the case of Cu^{2+}, sulfur did not have a direct interaction with the site, instead its adsorption in nearby places (such as Brönsted sites) limited the number of Cu^{2+} available for SCR reaction.

Chapter 3

Promoting effect of iron on high temperature Selective Catalytic Reduction of NOx over Cu-SSZ-13

Chapter 3 presents experimental results performed in the Environmental Catalysis research group at University of Antioquia, Colombia.

3.1 Introduction

A significant disadvantage of the current catalysts used for the selective catalytic reduction of NOx with ammonia consists in their low activity at high temperatures [20]. This characteristic, from a practical point of view, restrict their use during the periodical regeneration of soot filters in diesel exhaust systems that involves temperature increments [96]. Particularly, Cu-SSZ-13, one of the most promising catalyst for SCR reaction, have shown excellent NO conversion for SCR at temperatures as low as 200°C, but gradually loses activity as the temperature is raised over 300°C [20, 30]. Several authors have reported that as the temperature is increased above 300°C during SCR over Cu-SSZ-13, NH_3 conversion continues increasing due to a more relevancy of NH_3 oxidation side reaction. In consequence, the less availability of NH_3 causes a decline in NOx conversion [97, 20, 98].

In contrast to Cu-SSZ-13 catalyst, Fe supported zeolite catalysts have been reported to present high SCR activity when increasing the temperature above 400°C, but exhibiting poor SCR activity at temperatures below 300°C [99, 8]. Fe-ZSM-5, Fe-SAPO-34 and Fe-SSZ-13 have surpassed Cu-SSZ-13 performance during SCR, presenting NOx conversion near 100% in the range of 400 - 550°C [28, 29, 30]. Bad performance of Fe-zeolites observed at low temperatures is reported to be caused by a strong adsorption of NH_3 onto the active sites [30, 100, 101]. While at high temperatures, as in the case of Cu-SSZ-13, NH_3 oxidation have been observed to be an important factor in NOx loss of activity, but in a less extent [30].

In this work we propose the use of a bimetallic Cu-Fe-SSZ-13 catalyst to combine the good performance of Cu-SSZ-13 at low temperatures with the capabilities of Fe-SSZ-13 at high temperatures. The incorporation of Fe in Cu-zeolites for widening the working temperature of SCR catalysts is not new [28, 30, 29]. Nevertheless, cared must be taken since the followed procedure may change the nature of the active sites. Zhao *et al* [28] loaded Fe in a one-pot synthesized Cu-SAPO-34 catalyst by wetness impregnation with iron acetate solutions. The prepared Fe-Cu-SAPO-34 samples were tested for standard SCR to determine their catalytic activity, obtaining the best results with a sample presenting a Cu:Fe mass ratio of 2.87 (2.5 wt% Cu and 0.87 wt% Fe). Using EPR characterizations, the authors observed that Cu-SAPO-34 samples with additions of Fe, presented more isolated Cu species, which indicates that the incorporation procedure caused the migration of Cu species. Also, they observed that the number of Cu^{2+} active sites increased after Fe incorporation which they argued is caused by the migration of surface CuO clusters to inside pores and their transformation into Cu^{2+} species.

A way to avoid changes in the active species during the incorporation procedure consists in exchanging Fe and Cu separately in the same zeolite. Gao *et al* [30] prepared Cu-Fe-SSZ-13 by ion-exchanging Fe and Cu in separated samples of SSZ-13 zeolite, then a mechanical incorporation was performed by pressing, crushing and sieving. By this way, there is less probability of occurring inhibition effects in the formation of Cu and Fe active sites, since they are generated separately. A 1:1 mixture of Cu-SSZ-13 and Fe-SSZ-13 was tested for the standard SCR and it was observed an improvement in NO conversion in the 200-500°C

range, when compared with SCR over Cu-SSZ-13 and Fe-SSZ-13 at the same conditions.

During this study, the procedure for incorporating Fe and Cu in SSZ-13 reported by Gao *et al* [30] was followed. The contribution of this work comes from the fact that we were able to prepare two Cu-SSZ-13 catalysts with isolated Cu^{2+} and $[CuOH]^{1+}$ active sites, respectively (as presented in Section 2.3.1), by varying their Si:Al ratio [35]. Therefore, we could analyze separately the behavior of Cu sites in the presence of iron during SCR. The results are presented in the form of rate "light-off" curves for Cu-SSZ-13, Fe-SSZ-13 and Fe-Cu-SSZ-13 samples, to identify the activity of these materials toward SCR at temperatures between 200 and 600°C.

Consumption rates for NO and NH_3 measured in this study were obtained at the standard SCR conditions and as close as possible to a kinetically valid regime by changing GHSV and the catalyst amount. As discussed previously by Paolucci *et al* [20] to achieve differential conditions (NO conversion below 20%) at high temperatures is a difficult task, since at those conditions NOx conversion tend to rise near 100%, even at high GHSV. To have a better understanding of the reaction mechanism, NH_3 and NO oxidations were also studied.

3.2   Theoretical framework

3.2.1   SCR side reactions

As the temperature is increased above 300°C during SCR over Cu and Fe exchanged zeolites, several side reactions attain significance. Some of the most relevant are NO oxidation to NO_2 and ammonia oxidation to N_2 and NO, presented as follows [23].

3.2.1.1 NH_3 oxidation

Ammonia oxidation competes directly with SCR reaction at high temperatures, owing to a less availability of NH_3 that causes a drastic decrease in NO conversion [20, 102, 98]. The oxidation of ammonia at high temperatures generates N_2, NO and N_2O according to Equations (3.1) to (3.3). NO_2 is also formed by the reversible oxidation of NO after NO generation, Equation (3.4)[23, 103, 104]. It has been observed that NH_3 oxidation in Cu and Fe exchanged zeolites, at temperatures below 450 °C, proceeds by Equation (3.2), thus generating mostly N_2. At temperatures above 450 °C, NO, N_2O and NO_2 can be formed, Figure 3.1 [23].

$$4NH_3 + 5O_2 \rightarrow 4NO + 6H_2O \tag{3.1}$$

$$4NH_3 + 3O_2 \rightarrow 2N_2 + 6H_2O \tag{3.2}$$

$$2NH_3 + 2O_2 \rightarrow N_2O + 3H_2O \tag{3.3}$$

$$2NO + O_2 \leftrightarrow 2NO_2 \tag{3.4}$$
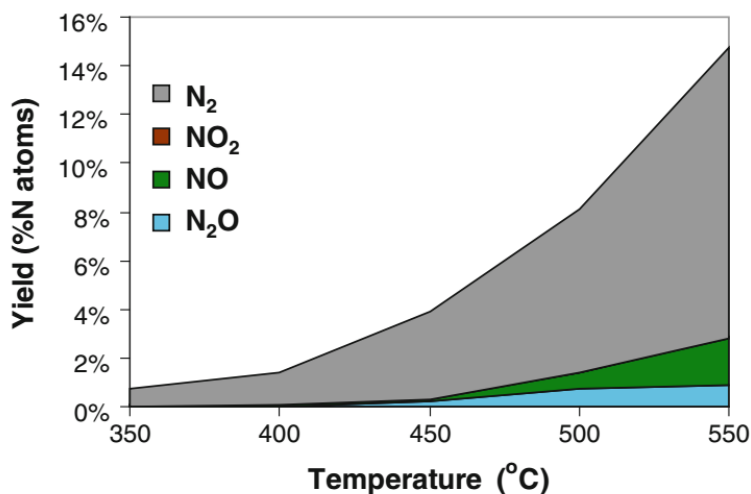
Figure 3.1: Ammonia oxidation over a Fe-zeolite catalyst at a GHSV of 90,000 h^{-1} and a feed of 300 ppm NH_3, 10 % O_2, 5 % CO_2, 5 %H_2O [23]

.

Gao *et al* [98] considering only Equation (3.2), reported ammonia oxidation kinetics, measured over Cu-SSZ-13 samples with Si:Al = 6 and 35 (relatively similar to our Si:Al = 4.5 and 25 samples, respectively), and Cu < 1%wt, in a high temperature range (400 - 550°C). Si:Al = 6 presented an $E_{a,app}$ = 70.8 kJmol^{-1}, while Si:Al = 35 presented two behavior with $E_{a,app}$ =61.9 (400 - 470°C) and 150 kJmol^{-1} (470 - 550°C). Even though these results must be interpreted cautiously since only Equation (3.2) was considered, the observed differences on $E_{a,app}$ may indicate a dependency of NH_3 oxidation reaction mechanism above 400°C with the type of Cu sites presented on the zeolite.

In the case of Cu-SSZ-13, the formation of $(NH_3)_2$-Cu-Cu-$(NH_3)_2$ dimers is a relevant step during SCR mechanism, (see Equation (3.4)). At temperatures above 350°C these dimers become unstable and dissociate to monomeric centers.

3.2.1.2 NO oxidation

NO reversible oxidation, Equation (3.4), have been used to study the oxidation half-cycle from low temperature SCR redox mechanism, explained in Section 1.1.6 [42, 41, 40]. According to a kinetic and computational study about Cu-SSZ-13 catalyst, carried out by Verma *et al* [86], isolated Cu^{2+} species were not active for NO dry oxidation, while extraframework Cu_xO_y clusters did present activity at 300°C. These copper oxide cluster were observed to be formed in a Cu-SSZ-13 sample with molar Si:Al = 4.5 (with mostly Cu^{2+} sites [105]), when the concentration of Cu in the sample exceeded Cu:Al mol ratio of 0.2 after ion-exchange. Gao *et al* [30] have also observed a near absence of NO oxidation activity in a Cu-SSZ-13 sample with Si:Al = 12 up to 550 °C (In a reactant feed containing 350 ppm NO, 14% O_2, 2.5% H_2O balanced with N_2 at a GHSV of 200,000 h^{-1}), consistent with an absence

of extraframework Cu oxide species. At the same conditions, Gao *et al* [30] observed that Fe-SSZ-13 presented 25% conversion for NO oxidation. However, until now Fe-SSZ-13 active species for NO oxidation are unknown.

3.2.2 Cu and Fe active sites in SSZ-13 and their involvement in high temperature SCR

3.2.2.1 Cu-SSZ-13 active sites

It is known that low temperature activity for SCR in Cu-SSZ-13 catalyst comes from dimeric Cu^{2+} species exchanged in two proximal Brönsted acid sites (BA) and from $[CuOH]^{1+}$ species exchanged in isolated BA, as discussed in Section 1.1.6 [35]. Synthesis of Cu-SSZ-13 samples differentiated in their type of active site can be achieved by controlling their Si/Al ratio, that limits the number of paired and isolated BA, and the copper content during ion-exchange, Figure 3.2 [34, 41].
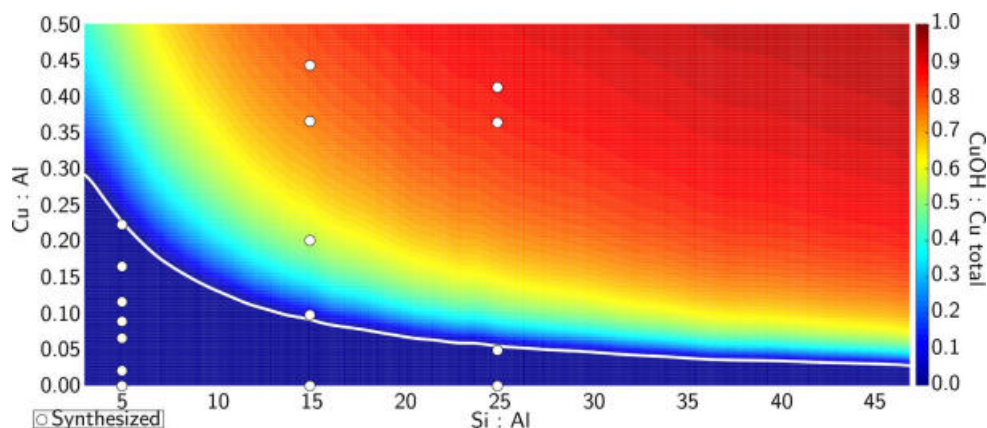
Figure 3.2: Cu site composition phase diagram, predicted by density functional theory calculations and obtained experimentally. Red color indicates predilection for $[CuOH]^{1+}$. White line demarcates transition from Cu^{2+}-only region to mixed Cu^{2+}-$[CuOH]^{1+}$ region. White circles indicate compositions of experimental Cu-SSZ-13 samples [41].

Quantification of Cu species in Cu-SSZ-13 is performed by measuring the number of paired (where only Cu^{2+} sites are formed) and isolated (where only $[CuOH]^{1+}$ sites are formed) BA. This procedure, developed by Di iorio *et al* [34], consists in exchanging cobalt in the H-SSZ-13 form, that as divalent cation will be selectively exchanged only on paired BA. Later, the remaining BA are quantified of by NH_3-TPD titration.

Cu sites behaviour during SCR changes with temperature rises. SCR activity is reported to decrease due to a more relevancy of side reactions (explained in Section 3.2.1) and because of a less NH_3 solvation of Cu sites [41]. Kinetics experiments performed near 350 °C showed that the apparent activation energy increased to 140 kJ mol^{-1}, indicating a change in SCR

reaction mechanism [102, 20].

3.2.2.2 Fe-SSZ-13 active sites

Depending on its loading, Fe can be incorporated in zeolites as several extraframework Fe^{3+} species: (1) mononuclear $[Fe(OH_2)]^{1+}$ and dimeric $[HO-Fe-O-Fe-OH]^{1+}$ ions, (2) oligomeric Fe_xO_y species and (3) poorly crystallized Fe oxide particles [106]. Quantification of these Fe species in zeolites is still under research because their simultaneously occurrence and interconversion (such as aglomerations) during their use, make difficult to develop a quantification method [106]. However, it is possible to generate, to certain extent, samples with partially isolated species. According to Gao *et al* [106] UV-vis and H_2 TPR results, it is expected that low Fe loading would generate monomeric Fe species while high Fe loading would tend to form poorly crystallized Fe oxide clusters.

Regarding SCR activity, Gao *et al* [106] and Brandemberger *et al* [107] suggest, from rate measurements in Fe-SSZ-13 and Fe-ZSM-5, respectively (and using different iron loading), that isolated Fe^{3+} species are responsible for SCR activity at low temperatures, while dimeric sites gives most of the activity at high temperatures. Also, NH_3 oxidation is reported to be catalyzed by Fe oligomers (larger than dimers) and by Fe_2O_3 particles, while monomeric Fe species are inactive for NH_3 activation up to $500°C$ [107, 106].

3.3 Experimental methods

3.3.1 Catalyst preparation

SSZ-13 zeolites were prepared with Si/Al ratios of 4.5 and 25 via the hydrothermal synthesis described in Section 2.3.1. These materials were intended to present paired BA and isolated BA, respectively, to later facilitate the formation, in an isolate manner, of copper active sites in Cu-exchanged SSZ-13 for SCR reaction (Cu^{2+} and $[CuOH]^{1+}$) [35]. Following the synthesis, copper and iron were ion exchanged in different samples of the parent SSZ-13 zeolites.

H-SSZ-13 samples with Si/Al = 4.5 and 25 were copper exchanged using 100 mL of $Cu(NO_3)_2$ solutions per gram of catalyst ($Cu(NO_3)_2.3H_2O$, 99% Aldrich). 1 g of H-SSZ-13 was dissolved in 100 mL deionized water and then heated at $80°C$ under constant stirring. Then, amounts of $Cu(NO_3)_2.2H_2O$ (98% Aldrich) were added to achieve 0.23 and 0.14 Cu molar concentration, for SSZ-13 Si:Al = 4.5 and 25, respectively. The exchange was led to proceed during 8 h under vapor recirculation, via a condenser, to avoid water evaporation. The samples were then rinsed in deionized water, centrifuged and let dry overnight at $105°C$. Calcination was performed at $550°C$ ($2°C\ min^{-1}$) during 8 h.

Iron was exchanged in H-SSZ-13 samples with Si/Al = 4.5 and 25, using solutions of $Fe(SO_3)_2$. Typically, 1 g of H-SSZ-13 was dissolved on 100 mL deionized water under mag-

netic stirring. Then, the pH was adjusted to 3 by adding drops of HNO_3 0.1 M and the temperature was increased to 80°C without further pH adjustment. An inert ambient was maintained by bubbling ~100 mL min^{-1} N_2 to avoid oxidation of Fe^{2+} to bulky Fe^{3+} moieties that may have problems diffusing into the zeolite [108, 106]. 1.1 g $Fe(SO_3)_2.7H_2O$ (98%, ITW Reagents) was added to the dissolved SSZ-13 and the exchange was performed during 1 h. The samples were then rinsed in deionized water, centrifuged and let dry overnight at 120°C in an inert N_2 ambient. Calcination was performed at 550°C (2°C min^{-1}) during 8 h. Fe-Cu-SSZ-13 samples were prepared by mechanical mixing Cu-SSZ-13 and Fe-SSZ-13 using mortar and pestle for ~ 15 min.

3.3.2   Catalyst characterization

The Chabazite structure of the synthesized SSZ-13 materials was confirmed by powder X-ray diffraction on a Rigaku Smart Lab® X-ray diffractometer with Cu K(α) radiation source operated at 1.76 kW. The diffraction patterns were measured from 4-40° 2θ at a scan rate of 2.4° min^{-1}. Silicon, aluminum, iron and copper composition was determined by atomic absorption using a Perkin-elmer AAnalyst® 300 atomic absorption spectrometer.

3.3.3   Reaction rate measurements

Reaction rate measurements for standard SCR reaction, NH_3 oxidation and NO oxidation over Cu-SSZ-13, Fe-SSZ-13 and their mixtures were performed on a 13 mm ID bench top tubular glass reactor, with a quartz frit located in the middle to hold a catalyst bed. The catalyst (sieved to a nominal size of 250 - 425 μm) was placed between two layers of quartz wool. A thermocouple was placed just above the catalyst bed to guarantee constant temperature and quartz beads were placed above the catalyst to ensure a proper gas mixing. Complete reaction rig is presented in Figure 3.3

The reaction conditions corresponded to the standard NH_3-SCR reaction (5000 ppm NO (3000 ppm in He, Airgas), 300 ppm NH_3 (3000 ppm in He, Airgas), 10% O_2 (99.99%, Cryogas) and 3% H_2O at 200°C. Argon (99.99%, Linde) was used as balance gas to obtain an overall flowrate of ~150 mL min^{-1}). Water was added to mixture of Ar, NO and O_2 by flowing balance argon through a gas bubbler in a water bath at 50°C. NH_3 (3000 ppm in He, Matheson Tri-gas) was added just at the reactor inlet to avoid formation of NH_4NO_3. For studying NH_3 and NO oxidation, the flow of either gas was stopped depending on the case, completing the total flow with more Ar flow. Effluent gases were analyzed by a Thermo-Scientific Antaris® IGS FTIR gas analyzer.
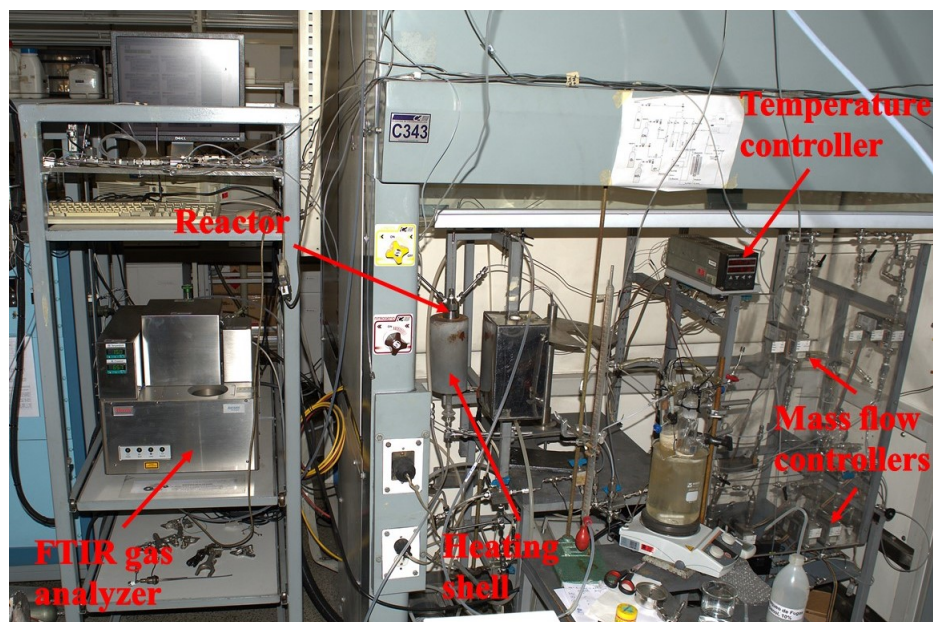
Figure 3.3: Reaction rig at University of Antioquia for measuring standard SCR reaction on Cu-SSZ-13 catalyst

The total flowrate of $\sim$150 mL min^{-1} used in this Chapter (instead of 1000 mL min^{-1} used in Chapter 2), was defined considering pressure limitations of the reaction rig presented in Figure 3.3. Higher flowrates would cause leaks in the reactor fittings and the possible breaking of a glass bubbler used to add water to the reaction gases.

3.4 Results and discussion

3.4.1 Catalyst characterizations

H-SSZ-13 Si:Al = 4.5 and 25 correspond to the same samples used in Chapter 2, which where sufficiently characterized in Section 2.4.1. Cu and Fe elemental composition in Cu-SSZ-13 and Fe-SSZ-13 samples is presented in Table 3.1. Composition of Cu-Fe-SSZ-13 samples obtained by mechanical mixtures of Cu-SSZ-13 and Fe-SSZ-13 with different ratios is also presented in Table 3.1. From now on, Fe-Cu-SSZ-13 with Si:Al ratio of 4.5 and 25 are named FeZ2Cu and FeCuOH, respectively. Also, note that Cu-SSZ-13 Si:Al = 25 and 4.5 are named ZCuOH and Z2Cu as in Chapter 2, but in this case the copper concentration are different (see Figure 3.4).

Conditions for ion-exchanging Cu in SSZ-13 Si/Al 4.5 and 25 were selected to avoid the presence of copper oxides. Table 3.1 shows that Cu weight concentration did not exceed 4% in both ZCuOH and Z2Cu. Therefore, and considering Figure 2.21, it is expected that samples with Cu does not present CuxOy clusters, inactive species for SCR [20]. Regarding Fe species in Fe-ZZS-13, it has been reported that in those materials, monomeric species are responsible for SCR activity at temperatures up to 300°C, while dimeric species, oligomeric

63

species and Fe_2O_3 particles are the active species at higher temperatures. Although we did not characterize iron species in our Fe-SSZ-13 and Fe-Cu-SSZ-13 samples, we expect them to present mostly dimeric and oligomeric species, because their Fe composition is similar to Fe-SSZ-13 samples reported in the literature and characterized by UV-vis, EPR, and and Mössbauer spectroscopic methods [106].

Table 3.1: Fe and Cu weight composition in Cu-SSZ-13, Fe-SSZ-13 and Fe-Cu-SSZ-13 samples, obtained by atomic absorption

Sample	Sample name	Si/Al (mol)	Fe%wt (%)	Cu%wt (%)	Fe/Cu (mol)
Cu-SSZ-13	Z2Cu	4.5	-	2.1600	-
Cu-SSZ-13	ZCuOH	25	-	1.3000	-
Fe-SSZ-13	-	4.5	0.6600	-	-
Fe-SSZ-13	-	25	1.1000	-	-
Fe-Cu-SSZ-13	FeZ2Cu 1:1	4.5	1.3868	0.3758	1.00/1.00
Fe-Cu-SSZ-13	FeZCuOH 0.25:0.75	25	0.4750	0.4190	0.25/0.75
Fe-Cu-SSZ-13	FeZCuOH 0.25:0.75	25	0.8458	0.2306	0.25/0.75

3.4.2 Testing diffusional limitations

Figure 3.4 shows external and internal mass transfer limitations tests, performed by measuring NO conversions during SCR over ZCuOH at different total flows and particle size, respectively, according to experiments proposed by Perego and Peratello [109]. In Figure 3.4 (A) it is observed that differences in NO conversion after changing the total flow between 100 and 200 mL min^{-1}, was negligible, evidencing a lack of external diffusion limitations. Due to limitations in the experiment setup it was not possible to study a broader range of flows. In addition, Figure 3.4 (B) shows the effect of using different catalyst particle size on NO conversion over ZCuOH. The selected particle sizes did not present evident changes in NO conversion at different temperatures, presumably by the relatively low total flow (150 mL min^{-1}) used in this study.

To further ensure the absence of diffusional artifacts, the Madon-Boudart (MB) criterion (described in Section 2.4.2.1) was tested in SCR over ZCuOH and Z2Cu at 200°C. In Figure 3.5 it is observed that, with slight deviations, both samples presented the tendency usually observed in SCR rates over Cu-SSZ-13 as a function of copper content. In consequence, and according to MB, rate measurements over ZCuOH and Z2Cu were free from heat and mass transfer limitations [84].
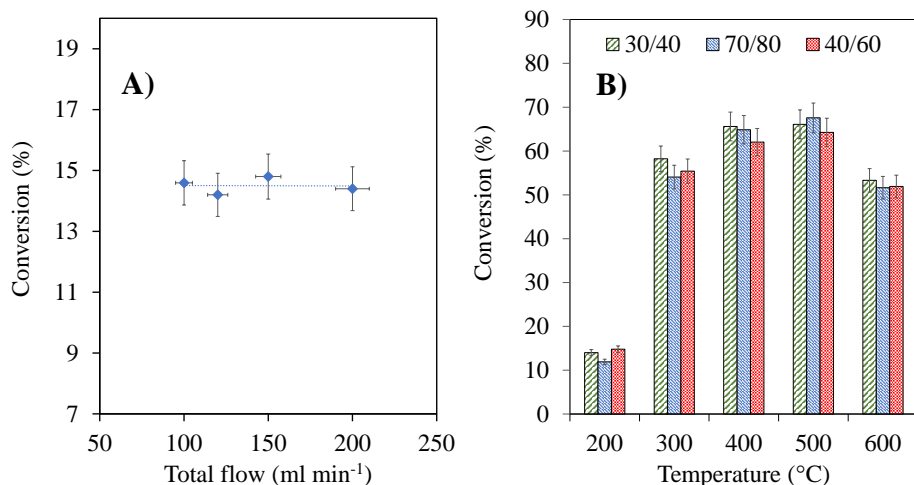
Figure 3.4: Effect of (A) total flow and (B) particle size (sieve sizes) on NO conversion during SCR over ZCuOH
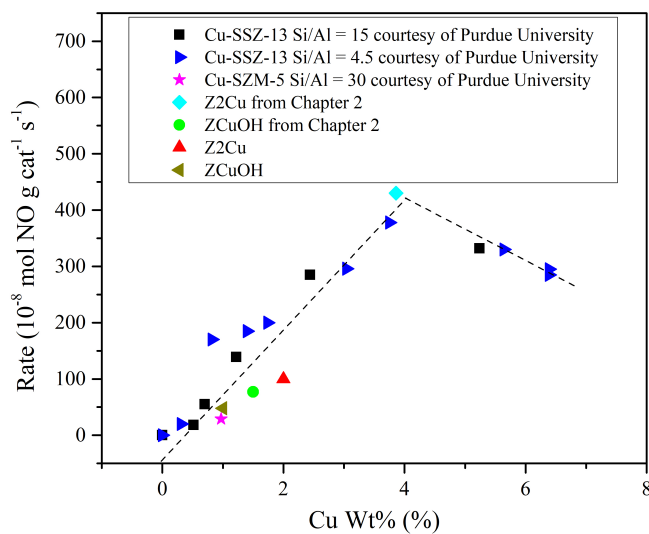
Figure 3.5: Standard SCR rates as function of copper content, obtained in this work and courtesy of Ribeiro research group from Purdue University, USA.

3.4.3 SCR and NH$_3$ oxidation over Z2Cu and ZCuOH at high temperatures

The "Light-off" curves depicting high conversions vs temperature usually presented in catalytic activity studies may hide reaction features that can help to elucidate particularities of a chemical reaction mechanism. Here we tried to avoid this problem by lowering NO conversion during SCR experiments (GHSV from 400000h^{-1} usually reported to 750000h^{-1}), as presented in Figure 3.6 SCR reaction rates for NO and NH$_3$ [30]. A first aspect that can

65

be seen is the so-called "seagull" behavior, which is presented in both ZCuOH and Z2Cu curves at 350°C. This phenomenon was also observed by Gao *et al* [30] in a Cu-SSZ-13 Si:Al = 12 sample at standard SCR conditions and is related to higher relevancy of side reactions and to changes in the reaction mechanism [20].

Aditionally, it has been reported that ZCuOH and Z2Cu present similar SCR rates at temperatures near 200°C during SCR [20]. However, in Figure 3.6 it was observed that, as the temperature was increased, changes in the performance of Z2Cu and ZCuOH became evident. Above 300°C, both ZCuOH and Z2Cu started to lose their ability to reduce NOx, but this behavior was more pronounced in ZCuOH.

NH$_3$ rate increased rapidly at temperatures above 350°C, as side reactions gain importance. Again, this is more pronounced in ZCuOH sample. Results from the "wet" oxidation of NH$_3$ (in the presence of 5% water), Figure 3.7, presents a similar tendency as SCR at high temperatures, suggesting that a less availability of NH$_3$ due to its own oxidation, plays an important role in the loss of NO rate during SCR.

Figure 3.6: High temperature SCR over (A) ZCuOH and (B) Z2Cu. SCR experiments were performed over ZCuOH and Z2Cu with similar metal loading and at the same GHSV of 600000 h^{-1}

As discussed in Section 3.2.1, the oxidation of NH$_3$ generates mainly harmless N$_2$, but as the reaction temperature rises, NOx generation becomes more relevant. Figure 3.7 shows that, from 400°C onwards, there is an increment in NO generation.

NO oxidation was also performed over ZCuOH and Z2Cu at 350 - 400 °C. But at these conditions, we did not detected any change in NO initial concentration. This would indicate the absence of Cu$_x$O$_y$ clusters which are reported to be the active species for NO oxidation in Cu-CHA zeolites and are inactive for NO reduction during SCR [86].
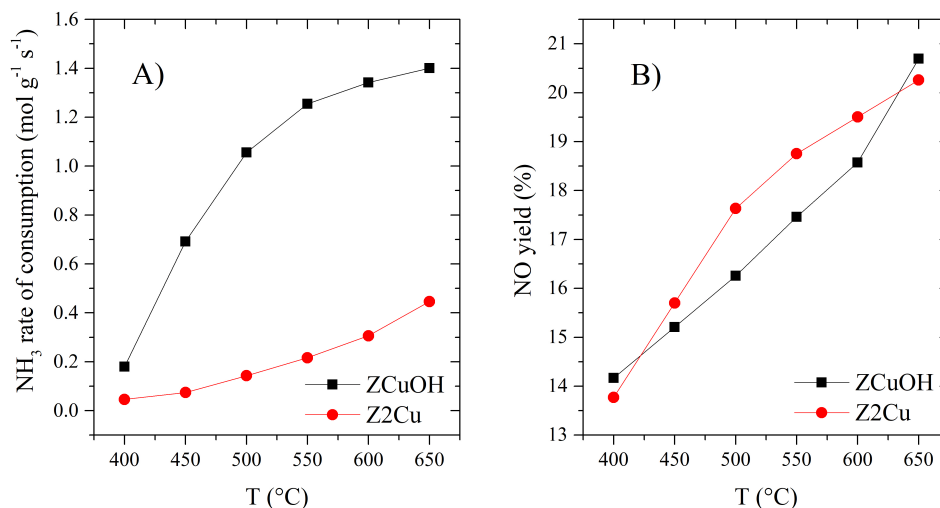
Figure 3.7: NH_3 oxidation over Z2Cu and ZCuOH. (A) NH_3 rate and (B) NO yield. NH_3 oxidation experiments were performed over ZCuOH and Z2Cu with similar metal loading and at the same GHSV of 600000 h^{-1}

3.4.4   SCR, NH_3 oxidation and NO oxidation over FeZ2Cu and FeZCuOH at high temperatures

3.4.4.1   SCR over FeZ2Cu and FeZCuOH at high temperatures

Figure 3.8 shows the effect of combining Fe and Cu in a chabazite zeolite on NO consumption rate during SCR. Including Fe on the catalyst improves NO rate at high temperature in both ZCuOH and Z2Cu, but its concentration may also affect the catalyst performance at low temperature by competing with Cu sites. This is evident in Figure 3.8 (A), where using Fe-Cu-SSZ-13 with a Fe:Cu ratio of 1:1 caused a reduction in ∼50% of NO rate compared with Cu-SSZ-13 in the 250 - 350°C range. We found that using a Fe:Cu molar ratio of 0.25:0.75 in the catalyst is an optimum between reactivity at low temperature and improvement in SCR activity at high temperature.

Fe-SSZ-13 SCR results for Si:Al = 4.5 and 25 in Figure 3.8 (A) and (B) showed the expected tendency on an increase in NO rates at high temperatures. However, Fe-SSZ-13 Si:Al = 25 presented a much lower NO rate which would indicate that Fe sites formed in this material are less active for SCR than those formed in the sample with Si:Al = 4.5. Similar results were observed for NH_3 rates in Figure 3.8 (C) and (D), where Fe-SSZ-13 Si:Al = 4.5 exhibited an increase in NH_3 rate after 500°C and Fe-SSZ-13 Si:Al = 25 presented a tendency more consistent with its own oxidation (presented in Figure 3.9) due to the lack of activity for NO presented previously.
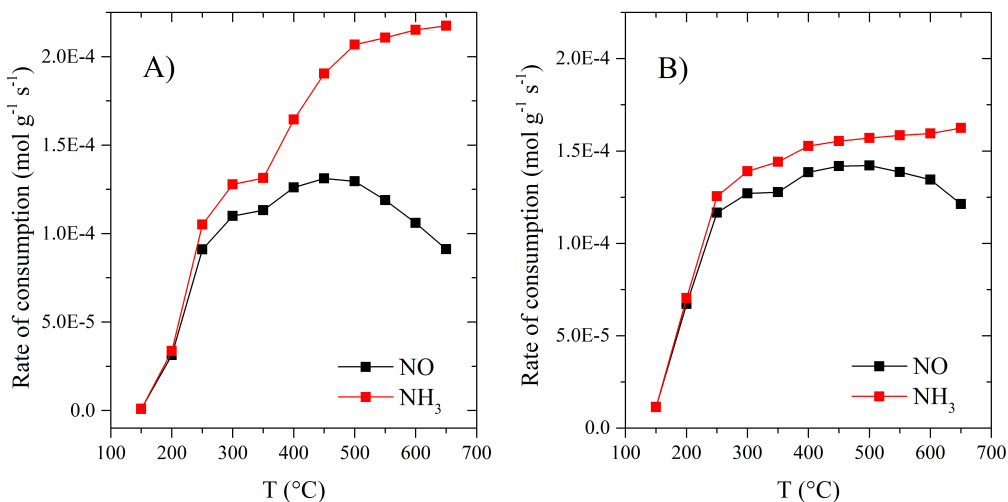
67
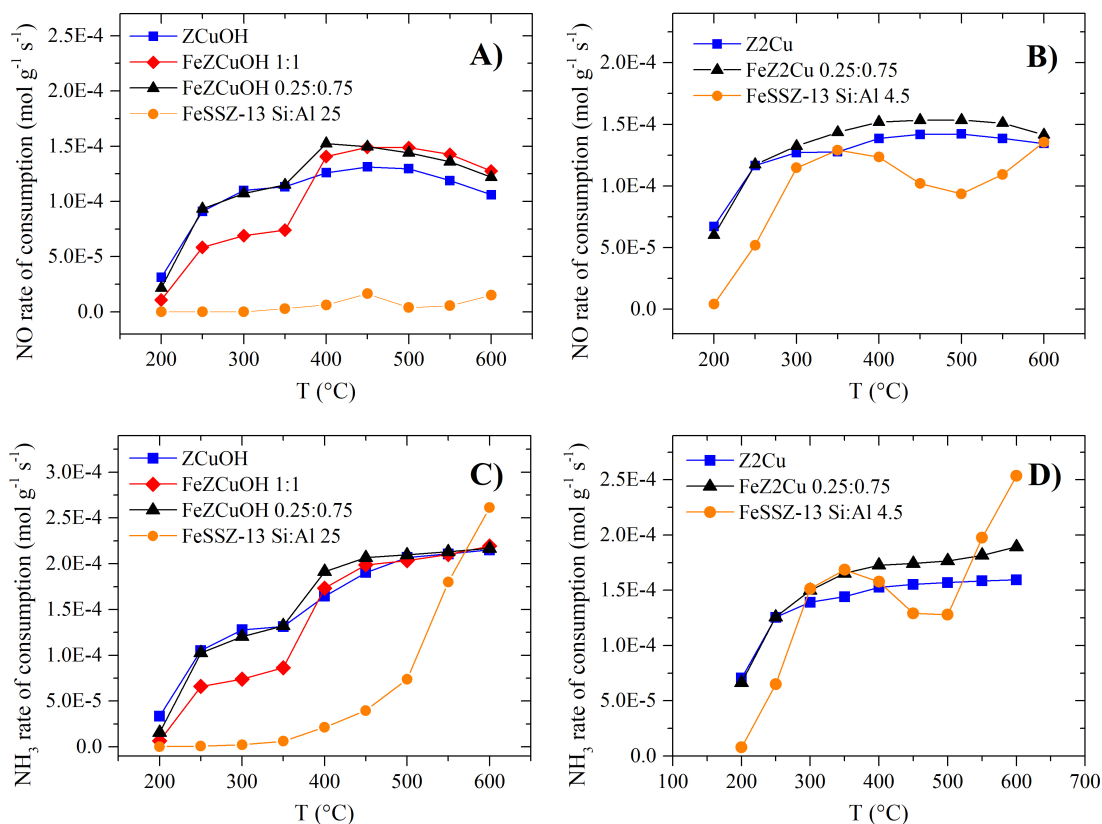
Figure 3.8: High temperature SCR rates over (A,C) FeZCuOH and (B,D) FeZ2Cu. SCR experiments were performed over ZCuOH and Z2Cu with similar metal loading and at the same GHSV of 600000 h^{-1}

3.4.4.2 NH$_3$ oxidation over FeZ2Cu and FeZCuOH at high temperatures

At temperatures higher than 400°C the oxidation of NH$_3$ is much more relevant than SCR. Comparing results from SCR and NH$_3$ oxidation over ZCuOH and Z2Cu in Figure 3.8 and Figure 3.9, the reaction rates for NH$_3$ are four orders of magnitude higher for NH$_3$ oxidation in both cases. In practical applications this would imply that at high temperatures most NH$_3$ is consumed in its own oxidation instead of reducing NO.

Figure 3.9 shows that the oxidation of NH$_3$ occurs in less extent in Z2Cu, consistent with the better NO SCR rates observed in Section 3.4.3. Between 10 - 20% NH$_3$ is converted into NO, similarly in ZCuOH and Z2Cu. In Figure 3.9 it is also observed that Fe causes an increase in NH$_3$ oxidation in both ZCuOH and Z2Cu.
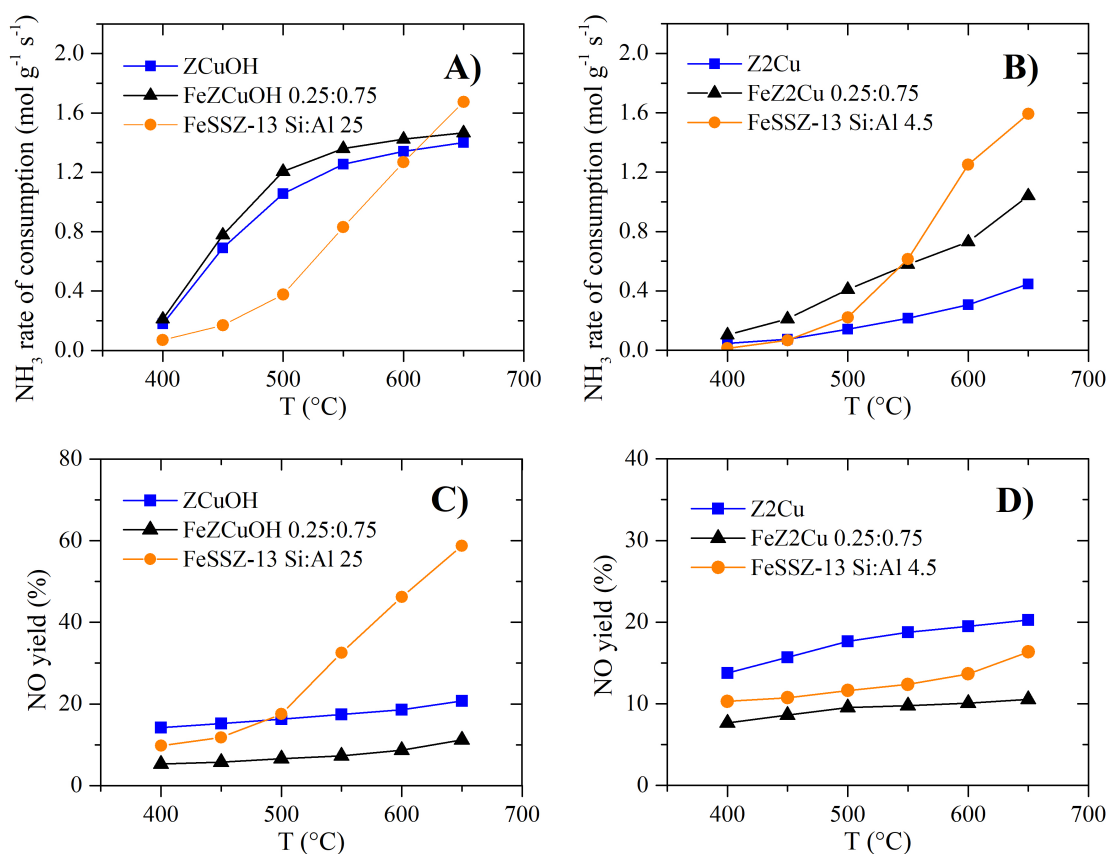
Figure 3.9: High temperature NH_3 oxidation over (A) FeZCuOH and (B) FeZ2Cu. SCR experiments were performed over ZCuOH and Z2Cu with similar metal loading and at the same GHSV of 600000 h^{-1}

3.4.4.3 NO oxidation over FeZ2Cu and FeZCuOH at high temperatures

We performed NO oxidation experiments to study the generation of nitrogen oxides, others than NO, that may be masked during SCR experiments. This is, higher NO rates observed in SCR experiments over Fe-Cu-SSZ-13, when compared with Cu-SSZ-13 samples, is not necessarily related to a reduction of NO to N_2. Instead, NO may have been oxidized to species such as NO_2 and N_2O.

Although we were not able to quantify the formation of N_2O and NO_2 by FTIR due to operational drawbacks, the consumption of NO in the presence of O_2 and H_2O can be used to establish how NO oxidation competes with SCR at high temperatures. In other words, if the catalyst does not present activity for NO oxidation at the most advantageous oxidative conditions (in the presence of NO and O_2 at high temperatures), then it is not likely to present activity at SCR conditions, in which a reducing agent (NH_3) is present.

While Cu-SSZ-13 did not present activity for NO oxidation due to the absence of Cu oxide clusters, as discussed in Section 3.4.3, results presented in Figure 3.10 show that Fe

caused up to 7% conversion of NO toward others NO oxides in Fe-Cu-SSZ-13 samples.

Figure 3.10 also shows that Fe-SSZ-13 Si/Al = 4.5 and Fe-Z2Cu catalysts presented a decrease in NO oxidation conversion at temperatures above 350°C. these results would imply that the low NO SCR conversion over Fe-SSZ-13 catalyst at temperatures under 350°C, reported elsewhere [30, 23, 101], is caused by a higher relevancy of NO oxidation reaction than SCR at those conditions.
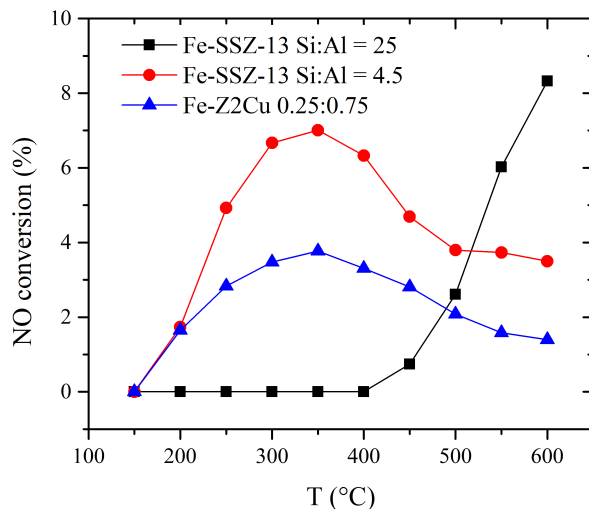
Figure 3.10: High temperature NO oxidation over Fe-SSZ-13 samples. Cu-SSZ-13 and Fe-Cu-SSZ-13 samples did not present NO conversion. Experiments were performed at a GHSV of 600000 h^{-1}

3.5   Conclusions

Cu-SSZ-13 and Fe-SSZ-13 catalysts were synthesized with Si:A = 4.5 and 25, then mixed mechanically to obtain Fe-Cu-SSZ-13 samples. Cu and Fe elemental composition was determined by atomic absorption. Reaction rates were obtained for the selective catalytic reduction, NH_3 oxidation and NO oxidation reactions for all catalysts at temperatures from 200 to 600°C. The absence of external and internal diffusional limitations was tested using a set of experiments proposed by Perego and Peratello and by employing Koros-Nowak criterion modified by Madon-Boudart.

NO and NH_3 rates obtained for SCR and NH_3 oxidation over ZCuOH and Z2Cu indicate that Z2Cu (Cu^{2+} active sites) has a better performance than ZCuOH ([CuOH]$^{1+}$ active sites) when the reaction temperature is raised over 350°C. This was evidenced in a slightly higher NO conversion and a much lower NH_3 oxidation. NO oxidation was not active for both ZCuOH and Z2Cu, which is consistent with the absence of Cu oxide clusters.

Fe-Cu-SSZ-13 presented higher SCR rates than Cu-SSZ-13 in the 350 - 600°C range as reported by several authors. However this can not be understood as an improve in NO reduction, since Fe also caused higher NH_3 oxidation rates and, unlike Cu, showed activity for NO oxidation at temperatures as low a 200°C (up to $\sim 7\%$ NO conversion in Fe-Cu-SSZ-13 samples).

A decrease in NO oxidation conversion at temperatures above 350°C, would imply that the low NO SCR conversion at temperatures bellow 350°C observed elsewhere for Fe-SSZ-13 catalyst is possibly caused by a higher relevancy of NO oxidation reaction than SCR at those conditions.

Chapter 4

Simultaneous effect of silicon content and structure directing agent in Brönsted acidity of SAPO-34

Chapter 4 presents experimental results performed in the research group of Professor Rajamani Gounder at Purdue University, USA.

4.1 Introduction

Silicoaluminophosphates (SAPO) are crystalline microporous materials with basic structures composed by alternating aluminum (Al^{3+}) and phosphorous (P^{5+}) species (ALPO) and topologically equivalent to zeolites [110, 19]. The catalytic activity of these materials is defined mainly by their density of Brönsted acid sites (BA), which occur when silicon (Si^{4+}) substitution in ALPO framework, during the synthesis, generates anionic unbalances that are compensated with protons, equivalently to Al^{3+} substitution for Si^{4+} in zeolites [19, 20]. SAPO-34 presents the same chabazite (CHA) structure of SSZ-13 zeolite, being used in similar applications such as the methanol-to-olefin synthesis (MTO) and the selective catalytic reduction of NOx when supported with copper or iron, presenting conversions near 100% in all cases [111, 112, 113, 114, 20].

SAPO-34 is typically obtained by a hydrothermal synthesis of a gel consisting of reactive phosphorous, silicon and aluminum compounds, and an organic structure directing agent (SDA) [19]. Multiple factors are determinant in the formation of BA in SAPO-34. In consequence, abundant reports can be found in literature, for instance, exploring the use of different sources of Si, Al, P, severals SDAs and the effect of their ratio [115, 116, 117, 118]. Silicic acid, tetraethyl orthosilicate, silica sol an colloidal silica have been used as sources of silicon [119, 120]. Also, aluminum isopropoxide and pseudobohemite have been used as aluminum precursors [121]. And several organic molecules (and mixtures of them) have been used as SDA: triethylamine (TEA), tetraethylammonium hydroxide (TEAOH), morpholine (MO), piperidine, diethylamine (DEA) [122, 123, 117, 121].

BA in SAPO materials occurs depending on the type of silicon species formed during the synthesis, in accordance with several mechanisms that not necessarily would end up in the generation of acid sites. A first silicon substitution mechanism in SAPO-34 consists in a silicon for aluminum replacement (denoted SM1) and would lead to the formation of Si-O-P bridges, which are energetically unfavorable and have not been observed experimentally so far. A second mechanism (SM2) involves a silicon for phosphorus substitution with a subsequent formation of Brönsted acid sites. And a third mechanism (SM3), in which a simultaneous substitution of neighboring Al^{3+} and P^{5+} by two silicon atoms occurs, causing the formation of neutral (and therefore catalytically inactive) silicon islands [19, 7, 36, 37].

The distribution of silicon atoms in SAPO-34 during the synthesis is highly influenced by the concentration of silicon and the structure directing agent. Excessive amounts of Si in the synthesis gel increases the occurrence of silicon islands and causes a loss in crystallinity [124, 125]. Xu *et al* [116] observed in samples prepared with triethylamine as SDA, that low concentration of silicon in the starting gel (smaller than a threshold ($Si/(Al + P + Si) = 0.031$)), all Si atoms take part in the SAPO-34 crystal nucleuses and only Si surrounded by Al atoms (SM2) were formed.

Furthermore, the SDA in SAPO-34 not only plays a structure-directing and space-filling role, as in the case of zeolites, but also provides the charge compensation that allows Si

to be incorporated into SAPO lattice [126, 115, 123]. Pastore *et al* [36] proposed that Si distribution depends on the number of framework charges, that in turn depends o the number of SDA molecules inside SAPO-34 structure. For instance, when comparing the SDAs morpholine (MO) and tetramethylammonium hydroxide (TEAOH), theoretically it would be more isolated silicon species when MO is used since chabazite cages may host up to two molecules of MO, whereas only one molecule of TEAOH. On the other hand, SAPO-34 is reported of being susceptible to desilication in the presence of water at room temperature [32]. Fortunately authors have observed that the selection of the SDA may improve the structural stability of SAPO-34 in such conditions.

Since the catalytic activity of SAPO-34 for SCR is controlled by its number of BA, that defines the amount of active species (Cu or Fe) that can be ion-exchanged into its framework, the synthesis conditions that promote the formation of BA (SM2 silicon substitution mechanism) were evaluated in this research. SAPO-34 was synthesized varying the composition of silicon in the synthesis gel and using triethylamine hydroxide (TEAOH) and morpholine (MO) as structure directing agents. The procedure consisted in a hydrothermal synthesis based on literature reports. Elemental composition was determined by atomic absorption and ICP-MS. The chabazite structure was confirmed via X-ray diffraction and SEM. Finally Brönsted acidity was quantified by NH_3-TPD.

4.2 Theoretical framework

4.2.1 SAPO-34

Silicoaluminophosphates (SAPOs) are a class of crystalline microporous molecular sieves formed by PO_4, AlO_4 and SiO_4 tetrahedrons. Some of these materials have intracrystalline pore volumes and pore diameters comparable to those known for zeolites and silica molecular sieves, hence they can be employed in applications where zeolites are used; with the advantage that most of SAPOs retain their structures at up to 1000 °C in air and at 600°C under 20% steam [19]. SAPO-34 presents a structure analogous to chabazite (CHA) zeolite, containing 8-member ring pore, wherein the orifice size is 0.38 nm x 0.38 nm [127].

4.2.2 Effect of Si composition in SAPO-34 synthesis

During the hydrothermal synthesis of zeolites, it is possible to predict the amount of formed Brönsted acid sites (BA) by changing the composition of silicon and aluminum in the initial gel. However, for the case of SAPO materials, due to the variety of silicon species presented, usually there is no correlation between the initial silicon content and the number of BA on the obtained SAPO-34 [111]. Several authors have studied the effect of silicon composition in the synthesis of SAPO-34, and it has generally been observed that low Si content produces less Si islands. Xu *et al* [116] reported that low silicon content (less than Si/(Al + P + Si) = 0.031) and using triethylamine as structure directing agent (SDA), causes that all Si atoms take part in the SAPO-34 crystal nucleuses and only isolated Si (S2) species are

formed. High silicon content, conversely, causes the formation of Si island that, besides being inactive for MTO and SCR reaction, changes particle formation [124, 125]. Izadbakhsh *et al* [125] observed by X-ray difraction and SEM experiments that higher amount of Si causes a loss in SAPO-34 cristallinity. Also, Wang *et al* [128] observed that increasing Si content also generates smaller crystal size in SAPO-34 . Finally, after the formation of silicon islands, excess Si would form an amorphous silica phase [37].

4.2.3   Effect of SDA in SAPO-34 synthesis

It has been proposed that the number of cations from the SDA that can be trapped inside SAPO-34 chabazite (CHA) cages, controls the way silicon is distributed in the lattice and therefore is a determining factor in the density of acid sites [115, 124]. In consequence, the nature of the SDA besides working as template and space filler during the syntesis of in SAPO-34, also plays a role in the distribution of silicon species by a phenomenon not well understood yet [20]. Zhao *et al* [124] classified several molecules that have been used as SDA in the synthesis of SAPO-34, by the type of cation charge that can be trapped in CHA cages, as R^+ (tetraethyl-ammonium hydroxide, triethylamine), $2R^+$ (diethylamine, morpholine) and $2R^{2+}$ (piperazine), Figure 4.1. Where R represents the SDA molecule inside the cage. Theoretically, morpholine and diethylamine will present the highest amount of isolated Si species per cage, and piperazine has a greater tendency of producing silicon islands.
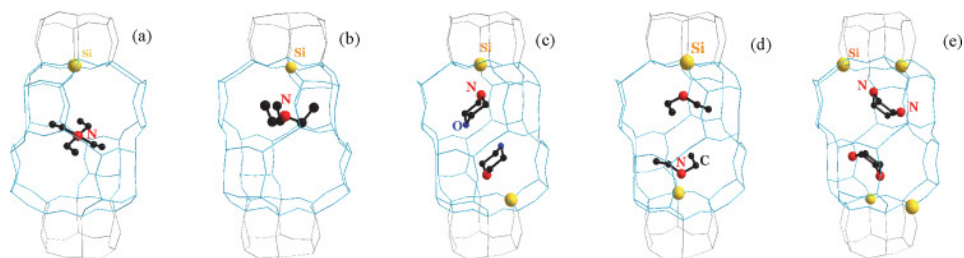
Figure 4.1: Organic template ions encapsulated in the CHA cage of SAPO-34 with their positive charge compensated by isolated Si atoms in the framework. (a) TEAOH (b) TEA (c) MOR (d) DEA (e) Piperazine [124].

It is important to mention that the selection of SDA may also change particle properties in SAPO-34. Alvaro-Munoz *et al* [121] used four different SDAs to obtain SAPO-34 (triethyl amine (TEA), tetraethyl ammonium hydroxide (TEAOH), methylamine (MO) and dipropyl amine (DPR)) while keeping constant the initial $Si/(Al + P + Si)$ content; observing changes in their physicochemical properties such as external surface and crystal size. These characteristics may be important in reactions as MTO in which low particle size is desired to avoid the formation of coke and the subsequent catalyst deactivation [129].

4.2.4 Mobility of silicon species in SAPO-34

The formation of silicon islands in SAPO-34 is not limited to the synthesis step. After removal of the structure directing agent, SAPO-34 is susceptible of Si-O-Al bond opening by hydrolysis in the presence of water at ambient temperature [31, 130]. This phenomenon causes the mobility and reordering of Si atoms leading to the formation of new silicon islands and an inherent reduction in the number of Brönsted acid sites, Figure 4.2 [32]. Silicon mobility is more severe when SAPO-34 is dispersed into liquid water at ambient temperature, in common processes such as aqueous ion-exchange of metals [31].
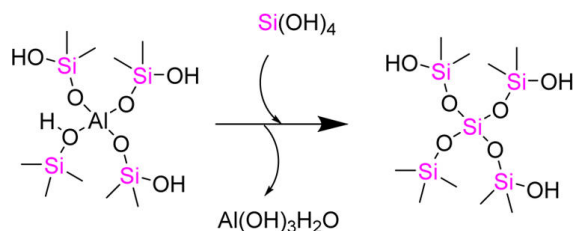

Figure 4.2: Schematic representation of the Si/Al exchange leading to the Si island within the SAPO structure [131].

4.3 Experimental methods

4.3.1 Synthesis of SAPO-34

SAPO-34 was obtained following a hydrothermal synthesis based on procedures reported elsewhere [132]. Phosphoric acid (85% in water, Aldrich), colloidal silica (40% Ludox, (99.9 wt %, Sigma-Aldrich)) and aluminum isopropoxide (Al(o – i – pr)$_3$, 98%, Aldrich) were used as phosphorous, silicon and aluminum source, respectively. Two different structural directing agents, morpholine (MO) (99%, Sigma-Aldrich) and triethylamine hydroxide (TEAOH) (35% in water, Aldrich) were used.

Synthesis gels were prepared by mixing the reactants with different molar ratio (presented in Table 4.1) in teflon jars. Typically, H_3PO_4 and Al(o – i – pr)$_3$ were diluted in deionized water and colloidal silica was dissolved in the SDA (morpholine or TEAOH). Both mixtures were stirred for 15 min, then the solution containing silica and SDA was added to the solution containing Al and P. The resulting slurry was stirred aged for 8 h at room temperature, then poured into 75 mL teflon liners inside autoclaves, where the crystallinization occurred at 200°C for 3 days.

To study the desilication of SAPO-34 during aqueous-phase ion exchange, approximately 200 mg of all SAPO-34 samples were converted to their ammonium form by ion exchange with 0.1 M NH_4NO_3 (>99%, Aldrich) (100 g solution per gram of catalyst) at 80°C for 10 h, followed by washing with deionized water, centrifuging and drying at 110°C for 12 h. Both

a-synthesized and NH_3-exchanged SAPO-34 samples were calcined in air at 550 °C (1°C min^{-1} ramp) for 6 h.

Table 4.1: Molar ratio of reactants used for SAPO-34 synthesis

Sample name	$Al(o-i-pr)_3$	H_3PO_4	SiO_2	Morpholine	TEAOH	Water
0.3Si MO	2	2	0.3	2	0	60
0.6Si MO	2	2	0.6	2	0	60
1.0Si MO	2	2	1.0	2	0	60
0.3Si TEAOH	2	2	0.3	0	2	60
1.0Si TEAOH	2	2	1.0	0	2	60

4.3.2 Catalyst characterization

4.3.2.1 AAS and ICP

Silicon and aluminum weight composition in all SAPO-34 samples were measured by atomic absorption on a Thermo Scientific iCE® Series 3000 spectrometer, as described in Section 2.3.2.1. Also, phosphorous content was measured by inductively coupled plasma - optical emission spectrometry (ICP-OES) on a Thermo Scientific iCAP® 7400 analyzer, following the procedures described in Section 2.3.2.3.

4.3.2.2 Powder X-Ray diffraction and SEM

Chabazite crystal structure of synthesized and ion exchanged SAPO-34 samples was confirmed via XRD pattern measurement on a Rigaku SmartLab® X-ray diffractometer with Cu K(α) radiation source operated at 1.76 kW. SAPO-34 samples of $\sim$100 mg were placed on an ASC-6® rotating sampler holder. Then, the diffraction patterns were measured from 4-40° 2θ at a scan rate of 2.4° min^{-1}. Crystal morphology of the different samples was compared using the latter XRD experiments and using Scanning electron images, collected on a FEI Quanta 3D FEG® scanning electron microscope.

4.3.2.3 NH_3-TPD

NH_3-TPD measurements were performed on a Micromeritics® Autochem II 2920 Chemisorption analyzer equipped with an Agilent® 5975C mass selective detector (MSD). Typically, $\sim$50 mg of sample was supported between two quartz wool plugs inside an U-shaped quartz flow-thru sample tube, that was later installed in the chemisorption unit. A flow of NH_3 was settled (3% NH_3 in argon, Praxair), diluted to 500 ppm with ultrahigh purity He (UHP, 99.99 %) at 160°C for 2 h and a total flow rate of 350 cm^3 min^{-1}. Next, 50 cm^3 min^{-1} helium (UHP, Praxair) flew through the sample at ambient temperature for 1 h to eliminate excess NH_3. Then, a temperature ramp was settled from 24 to 1000°C at a rate of 0.167°C s^{-1}. The effluent stream from the quartz cell was sent to the MSD for quantification. After each TPD

experiment, an injection of argon was used as a reference standard to correct instrument drift between TPD experiments. Typically, a 0.5 cm^3 sample loop was filled with argon (UHP, Praxair) and injected into a 50 cm^3 min^{-1} flow of UHP helium heading toward the MSD [65].

4.4 Results and discussion

4.4.1 Elementary composition by AAS and ICP

Compositions for Si, Al and P in synthesized SAPO-34 samples are presented in Table 4.2. Phosphorous to aluminum ratio presented in Figure 4.3 shows that the composition of Al and P in all samples are roughly 1:1, consistent with the initial gel composition (in which Si:Al ratio was also 1:1). This also confirms the strict Al-P alternating structure of SAPO-34. Regarding silicon content, Table 4.2 shows higher silicon incorporation with larger Si amounts in the initial gel, independently of the SDA.

Table 4.2: Composition of SAPO-34 samples

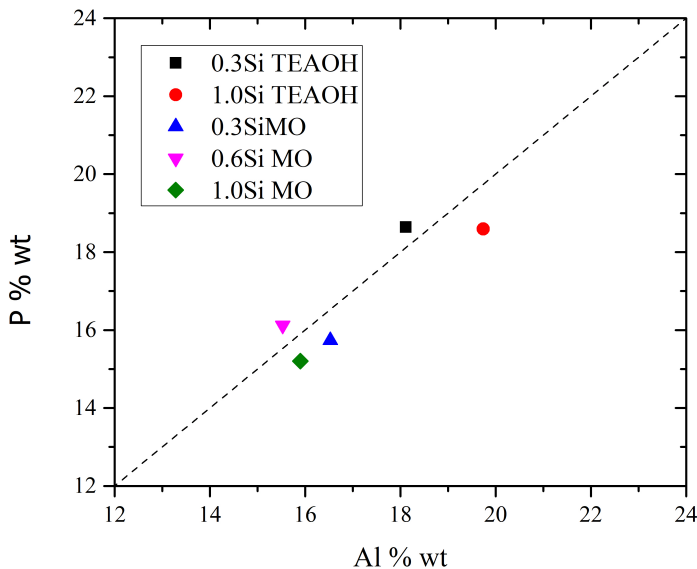| Sample name	Al	P	Si
0.3Si MO	16.529	15.733	4.748
0.6Si MO	15.529	16.120	6.999
1.0Si MO	15.900	15.206	7.588
0.3Si TEAOH	18.117	18.638	2.968
1.0Si TEAOH	19.742	18.795	7.509

Figure 4.3: P:Al weigth ratio in SAPO-34 samples

78

4.4.2 Morphological and crystalline properties of SAPO-34 by XRD and SEM

XRD pattern was measured in all synthesized SAPO-34 materials to corroborate that they presented a chabazite structure by comparison with a commercial sample, Figure 4.4. According to the results, all but 0.3Si MO sample presented chabazite structure. This suggests that if the silicon content in the initial synthesis gel is too small, morpholine would tend to form structures different from chabazite. In addition, crystallinity in SAPO-34 can be related to the intensity of diffraction peaks in X-ray diffractograms [121]. In this regard, in Figure 4.4 it is observed that sample 0.6Si MO presented the higher crystallinity from all synthesized SAPO-34 samples.

In order to have a better comparison between the crystallinity in SAPO-34 samples, relative X-ray diffraction intensities (% XRD intensity), that is the ratio between portions of the XRD pattern from the sample to the corresponding portion of the pattern of a reference zeolite. % XRD intensity was calculated for four arbitrary peaks (at 9.53, 12.98, 17.94 and 20.74° 2θ) and presented in Figure 4.5. Note that S_x and S_r in Equation (4.1) correspond to the sum of integral areas from the selected peaks in the sample and in the reference material, respectively. But Figure 4.5 instead shows the % XRD intensity from individual peaks, in order to have an easier analysis. It is evident in Figure 4.5 that sample 0.6Si MO presented the higher intensity which can be related to a higher crystallinity. When comparing between samples synthesized with the same SDA it is observed a tendency of having higher crystallinity for lower content of silicon. Izadbakhsh *et al* [125]. reported a similar result for SAPO-34 samples synthesized with TEAOH. They observed that as silicon content decreased to a 0.26 molar ratio, XRD patterns showed higher intensities.

$$\%\text{XRD intensity} = \frac{S_x}{S_r} * 100 \tag{4.1}$$

Where:
S_x = sum of integral peak intensities for the sample.
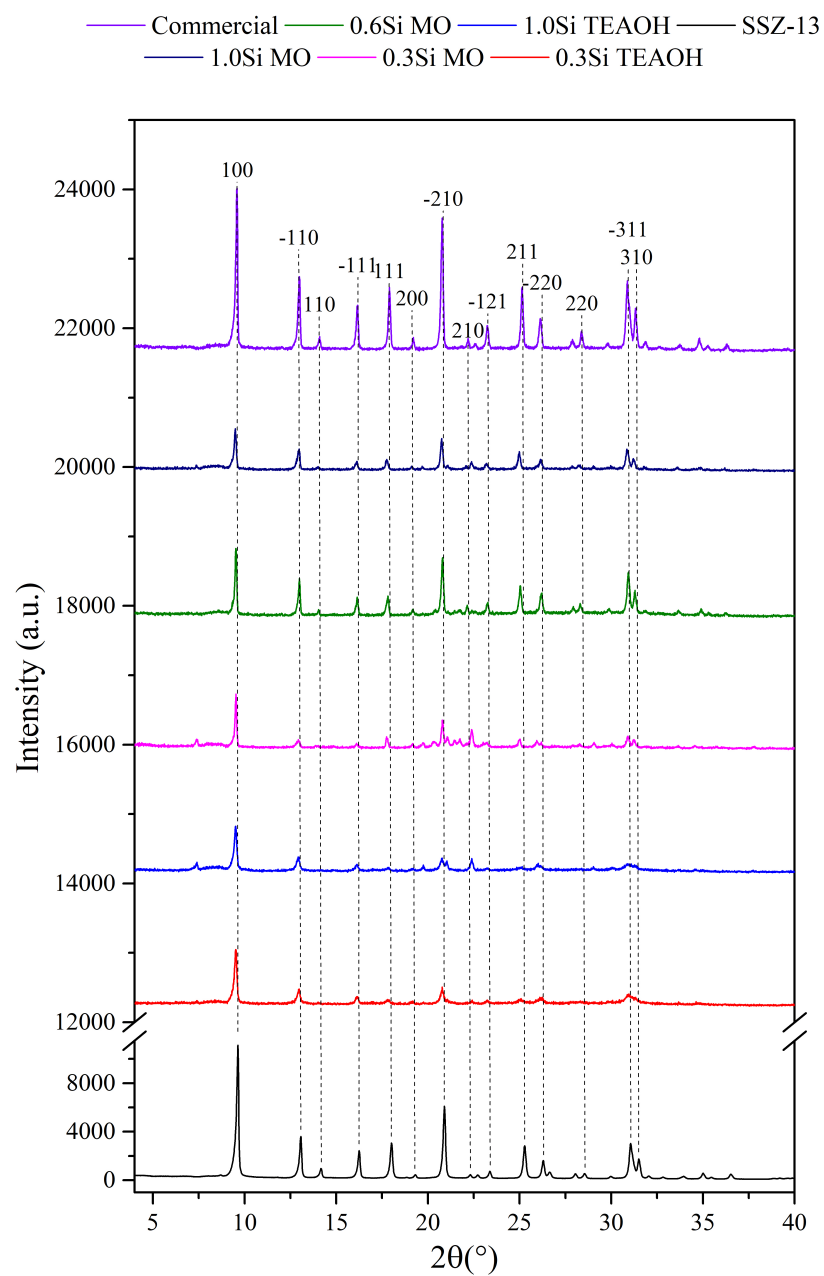S_r = sum of integral peak intensities for the reference compound.

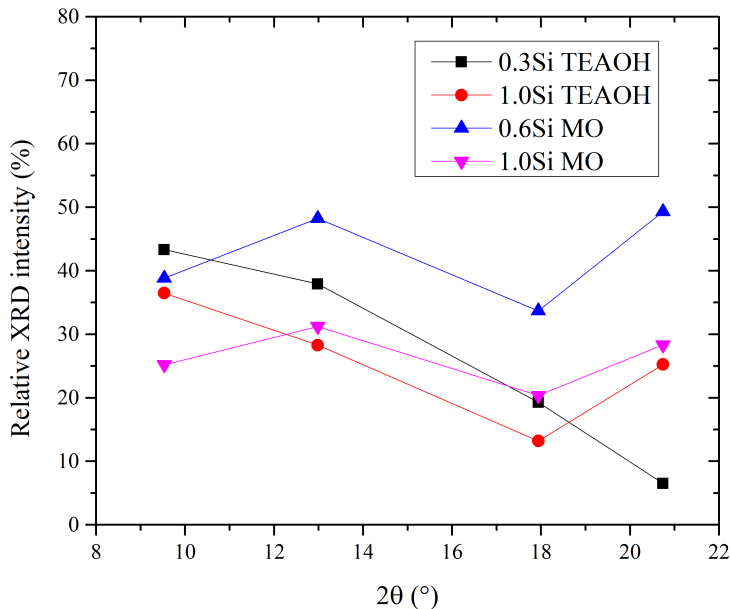Figure 4.4: XRD pattern for SAPO-34 samples

Figure 4.5: Relative XRD intensity for SAPO-34 samples. Commercial SAPO-34 used as reference

Table 4.3 shows crystallite size for SAPO-34 samples, calculated with Scherrer equation (Equation (2.10)) and using the most intense XRD band in Figure 4.4. It is observed a very similar cristallite size for all SAPO-34 samples, which indicates a similar grow of particles. This can be explained by the fact that we used the same time of aging, crystallization temperature and crystallization time for all SAPO-34 samples [133].

Table 4.3: Crystallite size of SAPO-34 synthesis

Sample name	2θ (°)	FWHM	τ (Å)
0.3Si TEAOH	0.08297	0.18969	0.16259
1.0Si TEAOH	0.08289	0.20269	0.16274
0.3Si MO	0.08310	0.12079	0.16235
0.6Si MO	0.08310	0.12278	0.16235
1.0Si MO	0.08278	0.15913	0.16296
Commercial	0.08348	0.13679	0.16161

SEM images in Figure 4.6 show that all samples presented mostly the typical cubic morphology of SAPO-34 [119, 37, 134], and a variety of crystal sizes. Samples synthesized using TEAOH presented small amounts of amorphous structures and crystal sizes ranging 2 - 8 μm. When morpholine was used as SDA, the samples presented more homogeneous and bigger crystals (10 - 45 μm). As Xu *et al* [116] suggest that a lower crystallinity in SAPO-34 is caused by the formation of silicon islands. it is expected (and studied in Section 4.4.3) that SAPO-34 samples synthesized with morpholine during this study, presented less silicon islands and therefore more density of Brönsted acid sites.
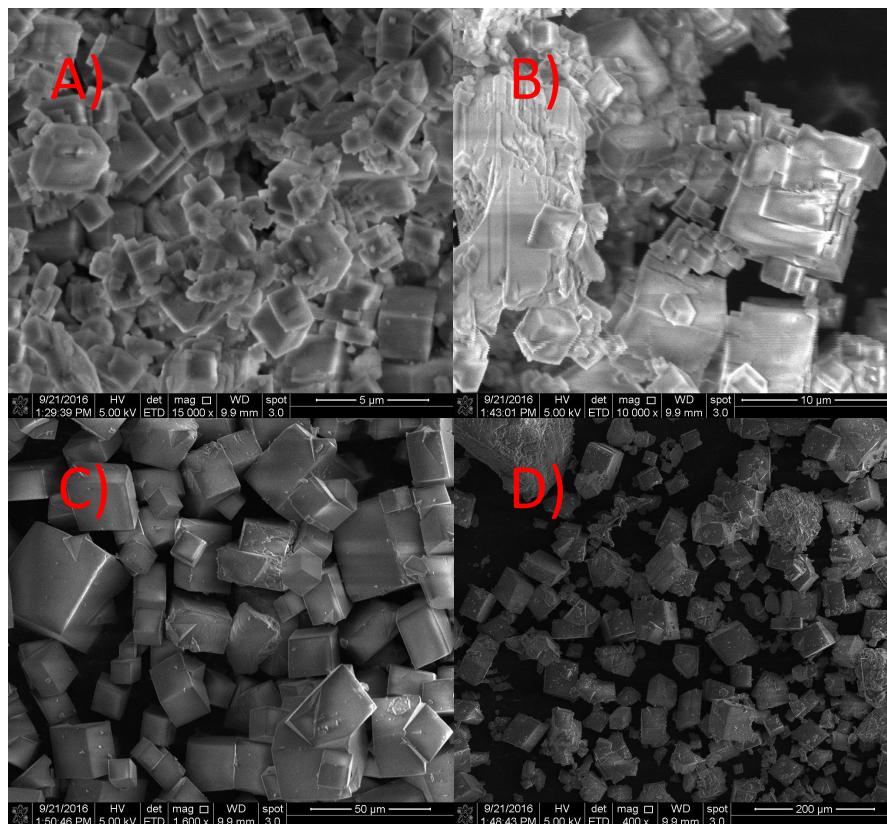
Figure 4.6: SEM results for SAPO-34 samples: (A) 0.3Si TEAOH (B) 1.0Si TEAOH (C) 0.6Si MO (D) 1.0Si MO

4.4.3 Acidity in SAPO-34 by NH$_3$-TPD

NH$_3$-TPD was used to determine the effect of silicon content and different SDA in SAPO-34 acidity. In general a low temperature desorption peak was observed at 280 - 400°C range and a high temperature peak at 400 - 700°C range, Figure 4.7. The low temperature peak has been reported to be related to weak Brönsted acidity and/or Lewis acidity while the high temperature peak has been assigned to strong Brönsted acidity from bridging hydroxyl groups, formed by replacement of P by Si (SM2 silicon substitution mechanism) [120, 125].

Integral area of NH$_3$ adsorption peaks in SAPO-34 samples were obtained after deconvolution and normalization over sample weight and area of a standard argon pulse (explained in Section 4.3.2.3). Results in Figure 4.7 show that samples synthesized using MO presented ~70% more Brönsted acid sites than those prepared with TEAOH as SDA. There is a tendency of acidity increase as the concentration of Si decreases, independently of the SDA. Zhao *et al* [124] suggest that high content of silicon promote the formation of Si islands. However, this tendency in MO samples changed for Si/SDA = 0.3. Unfortunately, we were not able to prepare samples at lower Si concentration, for having a better understanding of the acidity at those conditions.

Table 4.4: NH$_3$ peak intensity for SAPO-34 samples

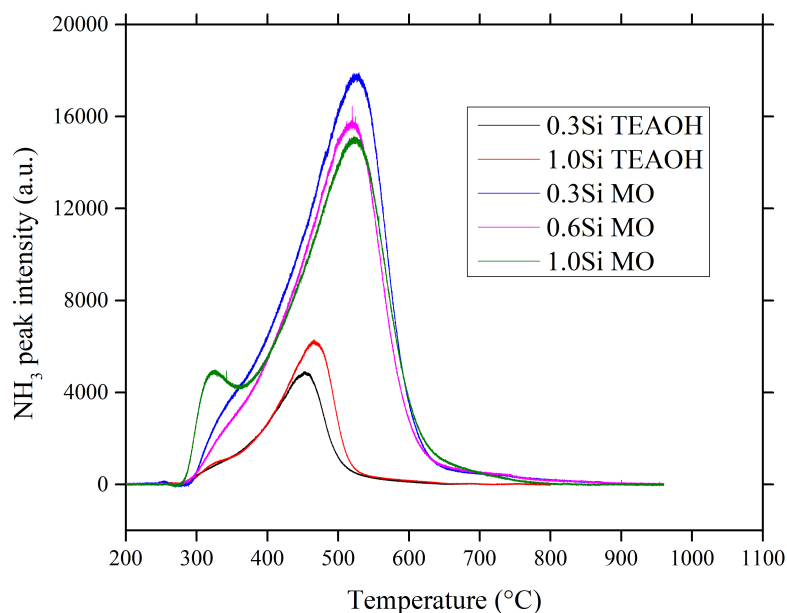| Sample | NH$_3$ peak intensity/g of catalyst (g^{-1}) | | BA/g of catalyst (mol/g) |
	Area at 280 - 400°C	Area at 400 - 700°C	
0.3Si TEAOH	20.41	65.38	0.0021
1.0Si TEAOH	22.11	86.91	0.0028
0.3Si MO	106.55	390.66	0.0126
0.6Si MO	77.04	342.35	0.0110
1.0Si MO	97.41	355.14	0.0114

Figure 4.7: NH$_3$-TPD in SAPO-34 synthesized with morpholine (MO) and tetraethylammonium hydroxide (TEAOH) as SDA

An ammonium form of SAPO-34 is usually obtained prior incorporating active species, using aqueous phase ion-exchange with solution of NH$_4$NO$_3$. We used this procedure to identify the lost of activity due to desilication of our samples, when they are put in contact with aqueous solutions. After performing NH$_3$-TPD experiments on as-synthesized and NH$_4$-exchanged SAPO-34 samples (Figure 4.8), it was observed that expose SAPO-34 to an aqueous ammonia solution does not increase the amount of Bronsted acid sites as occurs in SSZ-13; instead, roughly 85% of acid sites are lost due to desilication.
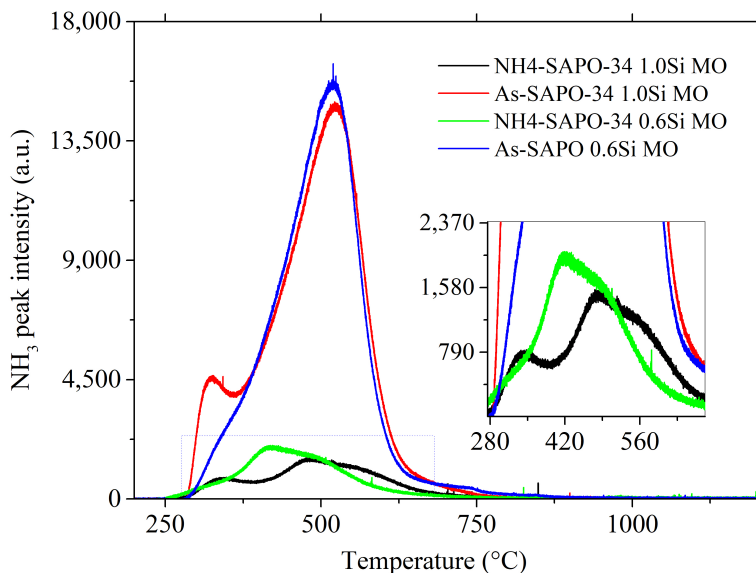
Figure 4.8: NH$_3$-TPD in as-synthesized and NH$_3$-exchanged SAPO-34

4.5 Conclusions

The effect of silicon content and the use of different structure directing agents (SDA) in the morphological and acidity properties of SAPO-34 was studied. Several SAPO-34 samples were prepared using morpholine (MO) and triethylamine hydroxide (TEAOH) as SDA and varing their silicon content in the synthesis gel from 1.0 to 0.3 Si molar composition in a mixture composed by 2Al(0–i–pr)$_3$ - 2H$_3$PO$_4$ - xSiO$_2$ - 2SDA - 60H$_2$O in molar composition.

Al:P molar ratio of 1 allowed us to estimate that all samples presented the basic Al-P alternating SAPO-34. Also, silicon content was proportional to the amount of silicon in the initial gel. Powder X-ray diffraction and SEM images were used to study the morphology of SAPO-34 samples. It was observed that using morpholine as SDA generated SAPO-34 with more homogeneous and bigger crystals. Also, while all samples synthesized using TEAOH as SDA presented CHA structure, a sample synthesized using morpholine and a 0.3 molar content of Si presented a structure different from CHA.

NH$_3$-TPD experiments showed that morpholine generates ∼70% more Brönsted acidity in SAPO-34 than TEAOH. Suggesting that morpholine causes a better Si distribution in SAPO-34 by generating more isolated Si species, while TEAOH produced more silicon islands. According to the results of this work, SAPO-34 prepared with morpholine and 0.6 mol silicon represents an equilibrium point between avoiding the formation of silicon islands while maintaining a chabazite structure.

Finally, NH$_3$-TPD experiments confirmed that aqueous ion exchange in SAPO-34 causes a decrease in its number of BA sites by disilication. After exchanging SAPO-34 with aqueous solutions of NH$_4$NO$_3$ it was observed a reduction in ∼85% of Bronsted acidity in calcined

NH$_4$-SAPO-34 samples.

General conclusions

5.1 Kinetic and Spectroscopic study of Selective Catalytic Reduction of NOx on SO$_2$ exposed Cu-SSZ-13

Kinetic experiments were carried out to identify the effect of sulfur in the catalytic activity of Cu-SSZ-13 during standard SCR and oxidative (60% O$_2$) SCR conditions. It was observed that NO consumption rate normalized by the number of Cu active sites (TOR) decreased as the concentration of sulfur increased, in both standard and oxidative SCR, evidencing a poisoning effect. Furthermore, changes in the apparent activation energy (E$_{a,app}$) and in the reaction orders for NH$_3$, NO and O$_2$ in sulfated ZCuOH samples suggested that sulfur causes changes in SCR mechanism over [CuOH]$^{1+}$ sites. While in Z2Cu, the absence of changes in E$_{a,app}$ and reaction orders indicated that SCR mechanism for this active site did not present changes.

UV-Vis-NIR spectrum collected on O$_2$ activated ZCuOH and Z2Cu showed that d-d transitions bands related to the formation of Cu dimers in ZCuOH (13230, 16500 and 19700 cm^{-1}) where dissipated in the presence of sulfur, indicating that [CuOH]$^{1+}$ sites lost their ability to form such dimers. Additionally, LMCT band centered at 43000 cm^{-1} presented sulfur-copper bonds related shoulders for sulfated ZCuOH (38000 cm^{-1}) and Z2Cu (39000 cm^{-1}), with considerable more prominence in ZCuOH. Moreover, *in-situ* UV-Vis-NIR spectrum collected while flowing NH$_3$ on ZCuOH and Z2Cu samples, showed that in both cases NH$_3$ adsorption ability was not lost due to the presence of sulfur. d-d transitions band at 17000 cm^{-1} observed in sulfur and ammonia containing copper salts, was also observed in unsulfated and sulfated ZCuOH and Z2Cu after NH$_3$ saturation, indicating that this band is related to Cu-NH$_3$ interactions.

Cu K-edge XAS spectra were collected on ZCuOH and Z2Cu samples at *Operando* and reducing SCR conditions. XANES results showed that the number of reduced Cu species in ZCuOH and Z2Cu decreased (∼30% and ∼50% in [CuOH]$^{1+}$ and Cu^{2+}, respectively) in the presence of sulfur. EXAFS characterizations at *Operando* SCR showed that ZCuOH fist coordination shell changed due to the presence of sulfur, while in Z2Cu this change was observed in the second coordination shell, indicating a more direct interaction of sulfur with [CuOH]$^{1+}$ sites. *Ex-situ* sulfur K-edge experiments performed on sulfated ZCuOH and

Z2Cu and in several Cu salts containing NH_3 and sulfur. According to the results, sulfur was always adsorbed in ZCuOH and Z2Cu as SO_4^{2+}.

5.2 Promoting effect of iron on high temperature Selective Catalytic Reduction of NOx over Cu-SSZ-13

NO and NH_3 rates obtained for SCR and NH_3 oxidation over ZCuOH and Z2Cu indicate that Z2Cu (Cu^{2+} active sites) has a better performance than ZCuOH ($[CuOH]^{1+}$ active sites) when the reaction temperature is raised over 350°C. This was evidenced in a slightly higher NO conversion and a much lower NH_3 oxidation. NO oxidation was not active for both ZCuOH and Z2Cu, which is consistent with the absence of Cu oxide clusters.

Fe-Cu-SSZ-13 presented higher SCR rates than Cu-SSZ-13 in the 350 - 600°C range as reported by several authors. However this can not be understood as an improve in NO reduction, since Fe also caused higher NH_3 oxidation rates and, unlike Cu, showed activity for NO oxidation at temperatures as low a 200°C (up to $\sim 4\%$ NO conversion in Fe-Cu-SSZ-13 samples).

5.3 Simultaneous effect of silicon content and the structure directing agent in improving Brönsted acidity of SAPO-34

Powder X-ray diffraction and SEM images were used to study the morphology of SAPO-34 samples. It was observed that using morpholine as SDA generated SAPO-34 with more homogeneous and bigger crystals. Also, while all samples synthesized using TEAOH as SDA presented CHA structure, a sample synthesized using morpholine and a 0.3 molar content of Si presented a structure different from CHA.

NH_3-TPD experiments showed that morpholine generates $\sim 70\%$ more Brönsted acidity in SAPO-34 than TEAOH. Suggesting that morpholine causes a better Si distribution in SAPO-34 by generating more isolated Si species, while TEAOH produced more silicon islands. According to the results of this work, SAPO-34 prepared with morpholine and 0.6 mol silicon represents an equilibrium point between avoiding the formation of silicon islands while maintaining a chabazite structure.

Publications

6.1 Papers

6.1.1 Spectroscopic and Kinetic Responses of Cu-SSZ-13 to SO_2 Exposure and Implications for NOx Selective Catalytic Reduction

Authors:
Arthur J. Shih[1], Ishant Khurana[1], Hui Li[2], Juan González[1,4], Ashok Kumar[3], Christopher Paolucci[2], Trevor M. Lardinois[1], Casey B. Jones[1], Jonatan D. Albarracin-Caballero[1], Krishna Kamasamudram[3], Aleksey Yezerets[3], W. Nicholas Delgass[1], Jeffrey T. Miller[1], Aída Luz Villa[4], William F. Schneider[2], Rajamani Gounder[1], Fabio H. Ribeiro[1]

Affiliations:
1. Charles D. Davidson School of Chemical Engineering, Purdue University, 480 Stadium Mall Drive, West Lafayette, IN 47907, USA.
2. Department of Chemical and Biomolecular Engineering, University of Notre Dame, Notre Dame, IN 46556, USA.
3. Cummins Inc., 1900 McKinley Avenue, MC 50183, Columbus, IN 47201, USA.
4. Environmental Catalysis Research Group, Chemical Engineering Department, Engineering Faculty, Universidad de Antioquia, Calle 70, No. 52-21, Medellín, Colombia.

6.1.2 Synthesis of Cu-SSZ-13 Materials With and Without Extraframework Cu_xO_y Species and its implications for NH_3 SCR of NO, dry NO oxidation, and NH_3 oxidation

Authors: Arthur J. Shih[1], Juan M. González[1,2], Lucía Pérez Ramírez[1], Andres Pena[1], Ishant Khurana[1], Aleksey Yezerets[3], Rajamani Gounder[1], Aída Luz Villa[2], and Fabio H. Ribeiro[1]

Affiliation:
1. Charles D. Davidson School of Chemical Engineering, Purdue University, 480 Stadium Mall Drive, West Lafayette, IN 47907, USA.
2. Environmental Catalysis Research Group, Chemical Engineering Department, Engineering Faculty, Universidad de Antioquia, Calle 70, No. 52-21, Medellín, Colombia.
3. Cummins Inc., 1900 McKinley Avenue, MC 50183, Columbus, IN 47201, USA.

Status: draft

6.1.3 High temperature SCR over Cu-SSZ-13 and Fe-Cu-SSZ-13

Authors: Juan González and Aída Luz Villa

Affiliation: Environmental Catalysis Research Group, Chemical Engineering Department, Engineering Faculty, Universidad de Antioquia, Calle 70, No. 52-21, Medellín, Colombia.

Status: draft

6.1.4 Synthesis of SAPO-34 with high content of Brönsted acid sites

Authors: Juan González[1,2], Arthur Shih[2] and Aída Luz Villa[1]

Affiliation:
1. Environmental Catalysis Research Group, Chemical Engineering Department, Engineering Faculty, Universidad de Antioquia, Calle 70, No. 52-21, Medellín, Colombia.
2. Charles D. Davidson School of Chemical Engineering, Purdue University, 480 Stadium Mall Drive, West Lafayette, IN 47907, USA.

Status: draft

6.1.5 UV-Vis-NIR evidences of SO_2 affecting NH_3 absorption onto Cu-SSZ-13 active sites and implications for SCR of NOx

Authors: Juan González[1,2], Arthur Shih[2] and Aída Luz Villa[1]

Affiliation:
1. Environmental Catalysis Research Group, Chemical Engineering Department, Engineering Faculty, Universidad de Antioquia, Calle 70, No. 52-21, Medellín, Colombia.
2. Charles D. Davidson School of Chemical Engineering, Purdue University, 480 Stadium

Mall Drive, West Lafayette, IN 47907, USA.
Status: draft

6.2   Events

6.2.1   Reducción catalítica selectiva de NOx a altas temperaturas (200 - 600°C) sobre Cu-SSZ-13 y Fe-Cu-SSZ-13

Authors: J.M. González and A.L. Villa
Affiliation: Environmental Catalysis Research Group, Chemical Engineering Department, Engineering Faculty, Universidad de Antioquia, Calle 70, No. 52-21, Medellín, Colombia.
Event: XI Simposio Colombiano de catálisis, Popayán, Colombia 2019.
Type of event: simposium
Type of presentation: oral

6.2.2   Estudio cinético y espectroscópico de la reducción catalítica selectiva de NOx con el catalizador Cu-SSZ-13 expuesto a azufre

Authors:
J.M. González[1,2], A.J. Shih[2], Hui Li[3], Ashok Kumar[4], Ishant Khurana[2], F.H. Ribeiro[2], Rajamani Gounder[2], A.L. Villa[1]
Affiliation:
1. Environmental Catalysis Research Group, Chemical Engineering Department, Engineering Faculty, Universidad de Antioquia, Calle 70, No. 52-21, Medellín, Colombia.
2. Charles D. Davidson School of Chemical Engineering, Purdue University, 480 Stadium Mall Drive, West Lafayette, IN 47907, USA.
3. Department of Chemical and Biomolecular Engineering, University of Notre Dame, Notre Dame, IN 46556, USA.
4. Cummins Inc., 1900 McKinley Avenue, MC 50183, Columbus, IN 47201, USA.
Event: XXVI Congreso Iberoamericano de catálisis, Coimbra, Portugal 2018.
Type of event: congress
Type of presentation: poster

6.2.3   Spectroscopic and Kinetic Responses of Cu-SSZ-13 to SO_2 Exposure and Implications for NOx Selective Catalytic Reduction

Authors:
Arthur J. Shih[1], Ishant Khurana[1], Hui Li[2], Juan González[1,4], Ashok Kumar[3], Christopher

Paolucci[2], Trevor M. Lardinois[1], Casey B. Jones[1], Jonatan D. Albarracin-Caballero[1], Krishna Kamasamudram[3], Aleksey Yezerets[3], W. Nicholas Delgass[1], Jeffrey T. Miller[1], Aída Luz Villa[4], William F. Schneider[2], Rajamani Gounder[1], Fabio H. Ribeiro[1]

Affiliations:
1. Charles D. Davidson School of Chemical Engineering, Purdue University, 480 Stadium Mall Drive, West Lafayette, IN 47907, USA.
2. Department of Chemical and Biomolecular Engineering, University of Notre Dame, Notre Dame, IN 46556, USA.
3. Cummins Inc., 1900 McKinley Avenue, MC 50183, Columbus, IN 47201, USA.
4. Environmental Catalysis Research Group, Chemical Engineering Department, Engineering Faculty, Universidad de Antioquia, Calle 70, No. 52-21, Medellín, Colombia.
Event: Aiche 2019.
Type of event: meeting
Type of presentation: oral

6.2.4 Speciation of Liquid Ion-Exchanged Cu into SSZ-13, ZSM-5, and Beta Zeolites

Authors: Arthur J. Shih[1], Juan M. González[1,2], Lucía Pérez Ramírez[1], Andres Peña[1], Ishant Khurana[1], Aleksey Yezerets[3], Rajamani Gounder[1], Aída Luz Villa[2], and Fabio H. Ribeiro[1]

Affiliation:
1. Charles D. Davidson School of Chemical Engineering, Purdue University, 480 Stadium Mall Drive, West Lafayette, IN 47907, USA.
2. Environmental Catalysis Research Group, Chemical Engineering Department, Engineering Faculty, Universidad de Antioquia, Calle 70, No. 52-21, Medellín, Colombia.
3. Cummins Inc., 1900 McKinley Avenue, MC 50183, Columbus, IN 47201, USA.
Event: Aiche 2018.
Type of event: meeting
Type of presentation: oral

6.2.5 Sulfur Deactivation Pathways in Cu-SSZ-13 Determined through First-Principle Modeling and X-Ray Spectroscopy

Authors:
Hui Li[1], Arthur J. Shih[2], Juan González[2,4], Ishant Khurana[2], Christopher Paolucci[2], Jeffrey Miller2, Tianpin Wu1, Aleksey Yezerets[3], Rajamani Gounder[2], Fabio H. Ribeiro[2], William F. Schneider[1]

Affiliations:
1. Department of Chemical and Biomolecular Engineering, University of Notre Dame, Notre Dame, IN 46556, USA.
2. Charles D. Davidson School of Chemical Engineering, Purdue University, 480 Stadium

Mall Drive, West Lafayette, IN 47907, USA.

3. Cummins Inc., 1900 McKinley Avenue, MC 50183, Columbus, IN 47201, USA.

4. Environmental Catalysis Research Group, Chemical Engineering Department, Engineering Faculty, Universidad de Antioquia, Calle 70, No. 52-21, Medellín, Colombia.

Event: Aiche 2017.

Type of event: meeting

Type of presentation: oral

6.2.6 Nature of SO$_2$ Poisoned Cu-SSZ-13 Catalysts Under Ammonia Selective Catalytic Reduction (NH$_3$-SCR) Conditions

Authors:

Arthur J. Shih[1], Hui Li[2], Ashok Kumar[3], Juan González[1,4], Ishant Khurana[1], Christopher Paolucci[2], Aída Luz Villa[4], W. Nicholas Delgass[1], Rajamani Gounder[1], Aleksey Yezerets[3], William F. Schneider[2], Jeffrey T. Miller[1], Fabio H. Ribeiro[1], Atish Parekh[1], Jonatan D. Albarracin-Caballero[1]

Affiliations:

1. Charles D. Davidson School of Chemical Engineering, Purdue University, 480 Stadium Mall Drive, West Lafayette, IN 47907, USA.

2. Department of Chemical and Biomolecular Engineering, University of Notre Dame, Notre Dame, IN 46556, USA.

3. Cummins Inc., 1900 McKinley Avenue, MC 50183, Columbus, IN 47201, USA.

4. Environmental Catalysis Research Group, Chemical Engineering Department, Engineering Faculty, Universidad de Antioquia, Calle 70, No. 52-21, Medellín, Colombia.

Event: Aiche 2017.

Type of event: meeting

Type of presentation: oral

Future work

SCR over Cu-SSZ-13 has multiple variables still to be studied. Some of the resulting research questions are listed:

- A diesel vehicle is constantly stopped in urban areas, which may reduce the exhaust gases temperature lower than 200°C. then, how is Cu-SSZ-13 performance at such conditions?

- In a diesel vehicle, soot from incomplete combustion usually oxidized in a step prior the SCR unit may generate NO_2. What is the effect of different NO_2 concentrations on SCR reaction mechanism over Cu-SSZ-13?

- In this work we studied the effect of SO_2 adsorbed in Cu-SSZ-13 at dry conditions. What effect may have adsorbing SO_2 in Cu-SSZ-13 in wet conditions (a more realistic scenario)?

- Sulfur species in diesel fuels are oxidized during the combustion in the engine mainly to SO_2. However, SO_3 can also be formed. What is the effect of SO_3 in SCR over Cu-SSZ-13?

- The presence of water in diesel exhaust gases at high temperatures, also called hydrothermal conditions may affect the performance of Cu-SSZ-13 catalyst. But the specific effect on $[CuOH]^{1+}$ and Cu^{2+} sites have not been studied so far. Therefore, how different behave the Cu active sites from Cu-SSZ-13 to hydrothermal aging?

Acknowledgments

I would like to sincerely thank to:

Bibliography

[1] Alan C. Lloyd and Thomas a. Cackette. "Diesel Engines: Environmental Impact and Control". In: *Journal of the Air & Waste Management Association* 51.6 (2011), pp. 809–847. ISSN: 1096-2247. DOI: 10.1080/10473289.2001.10464315.

[2] Joachim Lackner, Herbert Schumacher, and Hermann Grieshabe. "Areas of use for diesel engines". In: *Diesel Engine Management*. 2014, pp. 12–15. DOI: 10.1007/978-3-658-03981-3_2.

[3] Joseph Norbeck et al. *Evaluation of Factors That Affect Diesel Exhaust Toxicity*. Tech. rep. Sacramento: California Air Resources Board, 1998. URL: http://citeseerx.ist.psu.edu/viewdoc/download;jsessionid=AEF7E5361AF91993BB1C7695FD57DE9E?doi=10.1.1.621.250{\&}rep=rep1{\&}type=pdf.

[4] James Schauer et al. *Characterization and Control of organic compounds emitted from air pollution sources.pdf*. Tech. rep. California Inst. of Tech., Dept. of Environmental Engineering Science, 1998. URL: https://www.osti.gov/biblio/305765.

[5] İbrahim Aslan Reşitoğlu, Kemal Altinişik, and Ali Keskin. "The pollutant emissions from diesel-engine vehicles and exhaust aftertreatment systems". In: *Clean Technologies and Environmental Policy* 17.1 (2015), pp. 15–27. ISSN: 1618-954X. DOI: 10.1007/s10098-014-0793-9.

[6] Charles E Baukal and Wes Bussman. "NOx Emissions". In: *The John Zink Hamworthy Combustion Handbook*. 2012, pp. 417–477. ISBN: 978-1-4398-3962-1. DOI: 10.1201/b12975-16.

[7] Guido Busca. "Zeolites and Other Structurally Microporous Solids as Acid-Base Materials". In: *Heterogeneous Catalytic Materials*. Vol. 1. 2014, pp. 197–249. ISBN: 9780444595249. DOI: 10.1016/B978-0-444-59524-9.00007-9.

[8] Xingxing Cheng and Xiaotao T. Bi. "A review of recent advances in selective catalytic NOx reduction reactor technologies". In: *Particuology* 16 (2014), pp. 1–18. ISSN: 16742001. DOI: 10.1016/j.partic.2014.01.006.

[9] Bin Guan et al. "Review of state of the art technologies of selective catalytic reduction of NOx from diesel engine exhaust". In: *Applied Thermal Engineering* 66.1-2 (2014), pp. 395–414. ISSN: 13594311. DOI: 10.1016/j.applthermaleng.2014.02.021.

[10] Teresa Curtin. "Selective Catalytic Reduction of NOx". In: *Environmental Catalysis*. Ed. by V Grassian. Taylor and Francis, 2005. Chap. 8, pp. 197–210.

[11] M. Koebel, M. Elsener, and G. Madia. "Reaction Pathways in the Selective Catalytic Reduction Process with NO and NO2 at Low Temperatures". In: *Industrial & Engineering Chemistry Research* 40.1 (2001), pp. 52–59. ISSN: 0888-5885. DOI: 10.1021/ie000551y.

[12] Gerard Tuenter, Wim F Van Leeuwen, and Leo J M Snepvangers. "Kinetics and Mechanism of the NOx Reduction with NH3 on V205-W03-Ti02 Catalyst". In: *Industrial & Engineering Chemistry Product Research and Development* 25 (1986), pp. 633–636.

[13] Giuseppe Madia et al. "Side Reactions in the Selective Catalytic Reduction of NOx with Various NO2 Fractions". In: *Industrial & Engineering Chemistry Research* 41.16 (2002), pp. 4008–4015. ISSN: 0888-5885. DOI: 10.1021/ie020054c.

[14] Raúl Lobo. "Introduction to the Structural Chemistry of Zeolites". In: *Handbook of Zeolite Science and Technology*. Ed. by Scott Auerbach, Kathleen Carrado, and Prabir Dutta. Tailor & Francis Group, 2003. Chap. 3. DOI: 10.1201/9780203911167.ch3.

[15] Jens Weitkamp and L. Puppe. *Catalysis and Zeolites Fundamentals and Applications*. Springer-Verlag Berlin Heidelberg, 1999. ISBN: 978-3-642-08347-1. DOI: 10.1007/978-3-662-03764-5.

[16] Ch. Baerlocher and L.B. McCusker. *Database of Zeolite Structures*. 2017. URL: http://www.iza-structure.org/databases/ (visited on 05/04/2019).

[17] W. Baur and R. Fischer. *Microporous and other Framework Materials with Zeolite-Type Structures*. Vol. 14. Springer-Verlag, 2000. ISBN: 3-540-67961-8.

[18] Stacey Zones. *Zeolite SSZ-13 and its method of preparation*. 1985. URL: https://patents.google.com/patent/US4544538.

[19] Brent M. Lok et al. "Silicoaluminiphosphate Molecular Sieves: Another New Class of Microporus Crysalline Inorganic Solids". In: *Journal of American Chemical Society* 106.8 (1984), pp. 6092–6093. ISSN: 0036-7702. DOI: 10.1017/CBO9781107415324.004. arXiv: arXiv:1011.1669v3.

[20] Christopher Paolucci et al. *Catalysis Science of NOx Selective Catalytic Reduction with Ammonia over Cu-SSZ-13 and Cu-SAPO-34*. 1st ed. Vol. 59. Elsevier Inc., 2016, pp. 1–107. DOI: 10.1016/bs.acat.2016.10.002.

[21] Dong Fan et al. "SAPO-34 templated by dipropylamine and diisopropylamine: Synthesis and catalytic performance in the methanol to olefin (MTO) reaction". In: *New Journal of Chemistry* 40.5 (2016), pp. 4236–4244. ISSN: 13699261. DOI: 10.1039/c5nj02351c.

[22] Andrew M. Beale et al. "Recent advances in automotive catalysis for NOx emission control by small-pore microporous materials". In: *Chemical Society Reviews* 44.20 (2015), pp. 7371–7405. ISSN: 14604744. DOI: 10.1039/c5cs00108k. URL: http://dx.doi.org/10.1039/C5CS00108K.

[23] Isabella Nova and Enrico Tronconi. *Urea-SCR Technology for deNOx After Treatment of Diesel Exhausts*. Springer, 2014. ISBN: 978-1-4899-8070-0. DOI: 10.1007/978-1-4899-8071-7.

[24] Sandro Brandenberger et al. *The State of the Art in Selective Catalytic Reduction of NOx by Ammonia Using Metal-Exchanged Zeolite Catalysts*. Vol. 50. 4. 2008, pp. 492–531. ISBN: 0161494080. DOI: 10.1080/01614940802480122.

[25] Masakazu Iwamoto et al. "Copper(II) Ion-exchanged ZSM-5 zeolites as highly active catalysts for direct and continuous decomposition of nitrogen monoxide". In: *Journal of the Chemical Society - Series Chemical Communications* 16 (1986), pp. 1272–1273. ISSN: 00224936. DOI: 10.1039/C39860001272.

[26] Jonatan D. Albarracin-Caballero et al. "Structural and kinetic changes to small-pore Cu-zeolites after hydrothermal aging treatments and selective catalytic reduction of NO: X with ammonia". In: *Reaction Chemistry and Engineering* 2.2 (2017), pp. 168–179. ISSN: 20589883. DOI: 10.1039/c6re00198j. URL: http://dx.doi.org/10.1039/C6RE00198J.

[27] Ja Hun Kwak et al. "Excellent activity and selectivity of Cu-SSZ-13 in the selective catalytic reduction of NOx with NH3". In: *Journal of Catalysis* 275.2 (2010), pp. 187–190. ISSN: 00219517. DOI: 10.1016/j.jcat.2010.07.031.

[28] Huawang Zhao et al. "The promotion effect of Fe to Cu-SAPO-34 for selective catalytic reduction of NOx with NH3". In: *Catalysis Today* 297.May (2017), pp. 84–91. ISSN: 09205861. DOI: 10.1016/j.cattod.2017.05.060.

[29] Aiyong Wang et al. "NH3-SCR on Cu, Fe and Cu+Fe exchanged beta and SSZ-13 catalysts: Hydrothermal aging and propylene poisoning effects". In: *Catalysis Today* 320 (2019), pp. 91–99. ISSN: 09205861. DOI: 10.1016/j.cattod.2017.09.061.

[30] Feng Gao et al. "A comparative kinetics study between Cu/SSZ-13 and Fe/SSZ-13 SCR catalysts". In: *Catalysis Today* (2015), pp. 1–12. ISSN: 09205861. DOI: 10.1016/j.cattod.2015.01.025.

[31] Feng Gao et al. "Synthesis and Evaluation of Cu-SAPO-34 Catalysts for NH3-SCR I: Aqueous Solution Ion Exchange". In: *Acs Catalysis* 3 (2013), pp. 2083–2093. DOI: 10.1021/cs4004672.

[32] Torstein Fjermestad, Stian Svelle, and Ole Swang. "Desilication of SAPO-34: Reaction mechanisms from periodic DFT calculations". In: *Journal of Physical Chemistry C* 119.4 (2015), pp. 2073–2085. ISSN: 19327455. DOI: 10.1021/jp510844v.

[33] Jirí Cejka, Avelino Corma, and Stacey Zones. *Zeolites and Catalysis: Synthesis, Reactions and Applicatons*. Wiley-VCH, 2014. ISBN: 9783527324897.

[34] John R. Di Iorio and Rajamani Gounder. "Controlling the Isolation and Pairing of Aluminum in Chabazite Zeolites Using Mixtures of Organic and Inorganic Structure-Directing Agents". In: *Chemistry of Materials* 28.7 (2016), pp. 2236–2247. ISSN: 0897-4756. DOI: 10.1021/acs.chemmater.6b00181.

[35] Shane A. Bates et al. "Identification of the active Cu site in standard selective catalytic reduction with ammonia on Cu-SSZ-13". In: *Journal of Catalysis* 312 (2014), pp. 87–97. ISSN: 00219517. DOI: 10.1016/j.jcat.2014.01.004.

[36] H.O. Pastore, S. Coluccia, and L. Marchese. "Porous Aluminophosphates: From Molecular Sieves to Designed Acid Catalysts". In: *Annual Review of Materials Research* 35.1 (2005), pp. 351–395. ISSN: 1531-7331. DOI: 10.1146/annurev.matsci.35.103103.120732.

[37] Sunil Ashtekar, Satyanarayana V. V. Chilukuri, and Dipak K. Chakrabarty. "Small-Pore Molecular Sieves SAPO-34 and SAPO-44 with Chabazite Structure: A Study of Silicon Incorporation". In: *The Journal of Physical Chemistry* 98.18 (1994), pp. 4878–4883. ISSN: 0022-3654. DOI: 10.1021/j100069a018.

[38] Yasser Jangjou et al. "SO2 poisoning of the NH3 -SCR reaction over Cu-SAPO-34: Impact of ammonium sulfate versus other S-containing species". In: *ACS Catalysis* 6 (2016), 6612-6622. ISSN: 2155-5435. DOI: 10.1021/acscatal.6b01656.

[39] Lei Wang et al. "Location and nature of Cu species in Cu/SAPO-34 for selective catalytic reduction of NO with NH 3". In: *Journal of Catalysis* 289 (2012), pp. 21–29. ISSN: 00219517. DOI: 10.1016/j.jcat.2012.01.012. URL: http://dx.doi.org/10.1016/j.jcat.2012.01.012.

[40] Christopher Paolucci et al. "SI-Dynamic multinuclear sites formed by mobilized copper ions in NO x selective catalytic reduction". In: *Science* 357.6354 (2017), pp. 898–903. ISSN: 0036-8075. DOI: 10.1126/science.aan5630.

[41] Christopher Paolucci et al. "Catalysis in a cage: Condition-dependent speciation and dynamics of exchanged cu cations in ssz-13 zeolites". In: *Journal of the American Chemical Society* 138.18 (2016), pp. 6028–6048. ISSN: 15205126. DOI: 10.1021/jacs.6b02651.

[42] Christopher Paolucci et al. "Isolation of the copper redox steps in the standard selective catalytic reduction on Cu-SSZ-13". In: *Angewandte Chemie - International Edition* 53.44 (2014), pp. 11828–11833. ISSN: 15213773. DOI: 10.1002/anie.201407030.

[43] Ton V. W. Janssens et al. "A Consistent Reaction Scheme for the Selective Catalytic Reduction of Nitrogen Oxides with Ammonia". In: *ACS Catalysis* 5.5 (2015), pp. 2832–2845. ISSN: 2155-5435. DOI: 10.1021/cs501673g.

[44] William S. Epling et al. "Overview of the Fundamental Reactions and Degradation Mechanisms of NOx Storage/Reduction Catalysts". In: *Catalysis Reviews* 46.2 (2004), pp. 163–245. ISSN: 0161-4940. DOI: 10.1081/CR-200031932.

[45] Meiqing Shen et al. "Deactivation Mechanism of SO2 on Cu/SAPO-34 NH3-SCR catalysts: structure and active Cu2+". In: *Catal. Sci. Technol.* 5 (2015), pp. 1741–1749. DOI: 10.1039/c4cy01129e.

[46] Jinyong Luo et al. "Identification of two types of Cu sites in Cu/SSZ-13 and their unique responses to hydrothermal aging and sulfur poisoning". In: *Catalysis Today* 267 (2016), pp. 3–9. ISSN: 09205861. DOI: 10.1016/j.cattod.2015.12.002.

[47] Kurnia Wijayanti et al. "Deactivation of Cu-SSZ-13 by SO2 exposure under SCR conditions". In: *Catalysis Science & Technology* (2015). ISSN: 2044-4753. DOI: 10.1039/C5CY01288K.

[48] Ashok Kumar et al. "Impact of different forms of feed sulfur on small-pore Cu-zeolite SCR catalyst". In: *Catalysis Today* 231 (2014), pp. 75–82. ISSN: 0920-5861. DOI: 10.1016/j.cattod.2013.12.038.

[49] Sung-Won Ham et al. "Effect of Copper Contents on Sulfur Poisoning of Copper Ion-Exchanged Mordenite for NO Reduction by NH3". In: *Ind. Eng. Chem. Res.* 34 (1995), pp. 1616–1623. ISSN: 08885885.

[50] Yasser Jangjou et al. "Nature of Cu Active Centers in Cu-SSZ-13 and Their Responses to SO2Exposure". In: *ACS Catalysis* 8.2 (2018), pp. 1325–1337. ISSN: 21555435. DOI: 10.1021/acscatal.7b03095.

[51] Hue Li, Christopher Paolucci, and William F. Schneider. "First-principle modeling of SOx poisoning in SSZ-13". In: *First-principle modeling of SOx poisoning in SSZ-13*. 2015.

[52] Hui Li et al. "Determination of Sulfur Deactivation Pathways across Cu sites in Cu-SSZ-13". In: *25th North American Catalysis Society Meeting*. 2017.

[53] Michel Boudart. *Kinetics of chemical processes*. Ed. by Howard Brenner. Butterworth-Heinemann series in chemical engineering, 2001.

[54] Albert Vannice and William Joyce. *Kinetics of Catalytic Reactions*. Springer Science+Business Media, 2005. ISBN: 978-0-387-25972-7.

[55] Michel Boudart and Gerald Djega-Mariadassou. *Kinetics of heterogeneous catalytic reactions*. Princeton University Press, 1984. ISBN: 0-691-08347-9.

[56] John Sibilia. *A guide to materials characterization and chemical analysis*. 2nd ed. Wiley-VCH, 1996. ISBN: 0471186333.

[57] Gerhard Hübschen et al. *Materials characterization using nondestructive evaluation (NDE) methods*. 2016. ISBN: 9780857092359. DOI: 10.1016/B978-0-08-100040-3.01001-4. arXiv: arXiv:1011.1669v3.

[58] W. Bragg. *The diffraction of short electromagnetic waves by a crystal*. Vol. 17. 1913, pp. 43–57.

[59] John Van Loon. *Analytical Atomic Absorption Spectroscopy Selected Methods*. Academic Press, 1980. ISBN: 0-12-714050-6.

[60] Gerhard Ertl et al. *Handbook of Heterogeneous Catalysis*. Vol. 1. Wiley-VCH, 2008. DOI: 10.1002/9783527610044.hetcat0162.

[61] Xiandeng Hou and Bradley Jones. "Inductively Coupled Plasma/Optical Emission Spectrometry". In: *Encyclopedia of analytical chemistry* 11 (2000), pp. 9468–9485. DOI: 10.1080/00387010802375065. arXiv: arXiv:1011.1669v3.

[62] John W Olesik. "Elemental analysis using ICP-OES and ICP-MS". In: *Ana* 63.1 (1991), 12A –21A.

[63] Shane a. Bates et al. "Methods for NH3 titration of Bronsted acid sites in Cu-zeolites that catalyze the selective catalytic reduction of NOx with NH3". In: *Journal of Catalysis* 312 (2014), pp. 26–36. ISSN: 00219517. DOI: 10.1016/j.jcat.2013.12.020.

[64]   Luís Ernesto Sandoval-Díaz, Jhon Alex González-Amaya, and Carlos Alexander Trujillo. "General aspects of zeolite acidity characterization". In: *Microporous and Mesoporous Materials* 215 (2015), pp. 229–243. ISSN: 13871811. DOI: 10.1016/j.micromeso.2015.04.038.

[65]   John R. Di Iorio et al. "The Dynamic Nature of Brønsted Acid Sites in Cu-Zeolites During NOx Selective Catalytic Reduction: Quantification by Gas-Phase Ammonia Titration". In: *Topics in Catalysis* 58.7-9 (2015), pp. 424–434. ISSN: 10225528. DOI: 10.1007/s11244-015-0387-8.

[66]   Richard Nyquist. "Chapter 1 – Theory of Vibrational Spectroscopy". In: *Interpreting Infrared, Raman, and Nuclear Magnetic Resonance Spectra*. 5. 2001, pp. 1–24. ISBN: 9780125234757. DOI: 10.1016/B978-012523475-7/50165-0.

[67]   Peter Griffiths and James Haseth. *Fourier Transform Infrared Spectrometry*. Vol. 171. John Wiley and Sons, 2011, pp. 1–11. ISBN: 978-81-317-2325-8.

[68]   Robert a Schoonheydt. "UV-VIS-NIR spectroscopy and microscopy of heterogeneous catalysts". In: *Chemical Society reviews* 39.12 (2010), pp. 5051–66. ISSN: 1460-4744. DOI: 10.1039/c0cs00080a.

[69]   Bert M Weckhuysen. "Ultraviolet-Visible Spectroscopy". In: *In-situ Spectroscopy of Catalysts*. 2004. Chap. 12, pp. 255–270. ISBN: 1588830268.

[70]   Farideh Jalilehvand. *X-ray Absorption Spectroscopy (XAS)*. 2017. URL: http://www.chem.ucalgary.ca/research/groups/faridehj/xas.pdf (visited on 10/25/2018).

[71]   B. Ravel. *Introduction to x-ray absorption spectroscopy*. 2015. URL: https://www.bnl.gov/ps/userguide/lectures/Lecture-4-Ravel.pdf (visited on 10/25/2018).

[72]   Simon R. Bare and Thorsten Ressler. "Chapter 6 Characterization of Catalysts in Reactive Atmospheres by X-ray Absorption Spectroscopy". In: *Advances in Catalysis*. 1st ed. Vol. 52. C. Elsevier Inc., 2009, pp. 339–465. ISBN: 0360-0564\r978-0-12-374336-7. DOI: 10.1016/S0360-0564(08)00006-0. URL: http://dx.doi.org/10.1016/S0360-0564(08)00006-0.

[73]   J.-S. McEwen et al. "Integrated operando X-ray absorption and DFT characterization of Cu–SSZ-13 exchange sites during the selective catalytic reduction of NOx with NH3". In: *Catalysis Today* 184.1 (2012), pp. 129–144. ISSN: 09205861. DOI: 10.1016/j.cattod.2011.11.037.

[74]   T. Ressler. *WinXAS*. 2018. URL: http://www.winxas.de/.

[75]   B. Ravel and M. Newville. "ATHENA, ARTEMIS, HEPHAESTUS: data analysis for X-ray absorption spectroscopy using IFEFFIT". In: *J. Synchrotron Rad.* 12 (2005), pp. 537–541. URL: https://www.ncbi.nlm.nih.gov/pubmed/15968136.

[76]   José Rodriguez, Jonathan Hanson, and Peter Chupas. *Characterization of Heterogeneous Catalysts*. 2013. ISBN: 9781574444810. DOI: 10.1201/9781420015751.ch1.

[77]   Bert M Weckhuysen. "Operando spectroscopy: fundamental and technical aspects of spectroscopy of catalysts under working conditions". In: *Phys. Chem. Chem. Phys.* 5 (2003). DOI: 10.1039/b309654h.

[78] Dustin W. Fickel and Raul F. Lobo. "Copper coordination in Cu-SSZ-13 and Cu-SSZ-16 investigated by variable-temperature XRD". In: *Journal of Physical Chemistry C* 114 (2010), pp. 1633–1640. ISSN: 19327447. DOI: 10.1021/jp9105025.

[79] Ashok Kumar et al. "Chemical deSOx: An effective way to recover Cu-zeolite SCR catalysts from sulfur poisoning". In: *Catalysis Today* 267 (2016), pp. 10–16. ISSN: 09205861. DOI: 10.1016/j.cattod.2016.01.033.

[80] Terris T. Yang, Hsiaotao T. Bi, and Xingxing Cheng. "Effects of O2, CO2 and H2O on NOx adsorption and selective catalytic reduction over Fe/ZSM-5". In: *Applied Catalysis B: Environmental* 102.1-2 (2011), pp. 163–171. ISSN: 09263373. DOI: 10.1016/j.apcatb.2010.11.038. URL: http://dx.doi.org/10.1016/j.apcatb.2010.11.038.

[81] Arthur J Shih et al. "Spectroscopic and kinetic responses of Cu-SSZ-13 to SO2 exposure and implications for NOx selective catalytic reduction". In: *Applied Catalysis A: General* 574.25 (2019), pp. 122 –131. DOI: https://doi.org/10.1016/j.apcata.2019.01.024.

[82] Alexander Shishkin et al. "Synthesis and functionalization of SSZ-13 as an NH3 -SCR catalyst". In: *Catal. Sci. Technol.* 4.11 (2014), pp. 3917–3926. ISSN: 2044-4753. DOI: 10.1039/C4CY00384E. URL: http://xlink.rsc.org/?DOI=C4CY00384E.

[83] C. Suryanarayana and M. Grant Norton. *X-ray diffraction a practical approach.* Springer Science+Business Media, 1998. ISBN: 978-1-4899-0148-4. DOI: 10.1007/978-1-4899-0148-4.

[84] Rostam J. Madon and Michel Boudart. "Experimental Criterion for the Absence of Artifacts in the Measurement of Rates of Heterogeneous Catalytic Reactions". In: *Ind. Eng. Chem. Fundam.* 21 (1982), pp. 438–447. ISSN: 0196-4313. DOI: 10.1021/i100008a022.

[85] R.M. Koros and E.J. Nowak. "A diagnostic test of the kinetic regime in a packed bed reactor". In: *Chemical Engineering Science* 22.3 (1967), p. 470. ISSN: 00092509. DOI: 10.1016/0009-2509(67)80134-9.

[86] Anuj A. Verma et al. "NO oxidation: A probe reaction on Cu-SSZ-13". In: *Journal of Catalysis* 312 (2014), pp. 179–190. ISSN: 00219517. DOI: 10.1016/j.jcat.2014.01.017.

[87] Jonatan D. Albarracín-Caballero. "Structure-Activity Relationships of SSZ-13 and other Small Pore Zeolites for Catalytic NOx Abatement". PhD thesis. Purdue, 2016.

[88] Filippo Giordanino et al. "Characterization of Cu-exchanged SSZ-13: a comparative FTIR, UV-Vis, and EPR study with Cu-ZSM-5 and Cu-β with similar Si/Al and Cu/Al ratios." In: *Dalton transactions (Cambridge, England : 2003)* 42.35 (2013), pp. 12741–61. ISSN: 1477-9234. DOI: 10.1039/c3dt50732g.

[89] Enrica Gianotti et al. "NH3 adsorption on MCM-41 and Ti-grafted MCM-41. FTIR, DR UV-Vis-NIR and photoluminescence studies". In: *Physical Chemistry Chemical Physics* 4.24 (2002), pp. 6109–6115. ISSN: 14639076. DOI: 10.1039/b207231a.

[90] Bahar Ipek et al. "Formation of [Cu2O2]2+ and [Cu2]2+ toward C–H Bond Activation in Cu-SSZ-13 and Cu-SSZ-39". In: *ACS Catalysis* 7.7 (2017), pp. 4291–4303. ISSN: 2155-5435. DOI: 10.1021/acscatal.6b03005.

[91]   J. S. Woertink et al. "A [Cu2O]2+ core in Cu-ZSM-5, the active site in the oxidation of methane to methanol". In: *Proceedings of the National Academy of Sciences* 106.45 (2009), pp. 18908–18913. ISSN: 0027-8424. DOI: 10.1073/pnas.0910461106. arXiv: arXiv:1408.1149.

[92]   Z. Y. Zhang et al. "Adsorptive removal of aromatic organosulfur compounds over the modified Na-Y zeolites". In: *Applied Catalysis B: Environmental* 82.1-2 (2008), pp. 1–10. ISSN: 09263373. DOI: 10.1016/j.apcatb.2008.01.006.

[93]   Kurnia Wijayanti et al. "Effect of gas compositions on SO2 poisoning over Cu-SSZ-13 used for NH3-SCR". In: *Applied Catalysis B: Environmental* 219.2 (2017), pp. 142–154. ISSN: 09263373. DOI: 10.1016/j.apcatb.2017.07.017.

[94]   Vincent F. Kispersky et al. "Low absorption vitreous carbon reactors for operando XAS: a case study on Cu/Zeolites for selective catalytic reduction of NOx by NH3". In: *Phys. Chem. Chem. Phys.* 14.7 (2012), pp. 2229–2238. ISSN: 1463-9076. DOI: 10.1039/C1CP22992C.

[95]   Moon Hyeon Kim, In Sik Nam, and Young Gul Kim. "Characteristics of mordenite-type zeolite catalysts deactivated by SO2 for the reduction of NO with hydrocarbons". In: *Journal of Catalysis* 179.2 (1998), pp. 350–360. ISSN: 00219517. DOI: 10.1006/jcat.1998.2230.

[96]   Stanislava Andonova et al. "The effect of iron loading and hydrothermal aging on one-pot synthesized Fe/SAPO-34 for ammonia SCR". In: *Applied Catalysis B: Environmental* 180.x (2015), pp. 775–787. ISSN: 09263373. DOI: 10.1016/j.apcatb.2015.07.007.

[97]   Ja Hun Kwak et al. "The effect of copper loading on the selective catalytic reduction of nitric oxide by ammonia over Cu-SSZ-13". In: *Catalysis Letters* 142.3 (2012), pp. 295–301. ISSN: 1011372X. DOI: 10.1007/s10562-012-0771-y.

[98]   Feng Gao et al. "Effects of Si/Al ratio on Cu/SSZ-13 NH3-SCR catalysts: Implications for the active Cu species and the roles of Brønsted acidity". In: *Journal of Catalysis* 331 (2015), pp. 25–38. ISSN: 10902694. DOI: 10.1016/j.jcat.2015.08.004.

[99]   James Girard et al. "Combined Fe-Cu SCR Systems with Optimized Ammonia to NOx Ratio for Diesel NOx Control". In: *SAE International Journal of Fuels and Lubricants* 1.1 (2008), pp. 603–610. ISSN: 1946-3960. DOI: 10.4271/2008-01-1185.

[100] I. Nova, M. Colombo, and E. Tronconi. "Kinetic Modeling of Dynamic Aspects of the Standard NH3-SCR Reaction Over V2O5-WO3/TiO2 and Fe-Zeolite Commercial Catalysts for the Aftertreatment of Diesel Engines Exhausts". In: *Oil & Gas Science and Technology – Revue d'IFP Energies nouvelles* 66.4 (2011), pp. 681–691. ISSN: 1294-4475. DOI: 10.2516/ogst/2011132.

[101] S. Malmberg et al. "Dynamic phenomena of SCR-catalysts containing Fe-exchanged zeolites - Experiments and computer simulations". In: *Topics in Catalysis* 42-43.1-4 (2007), pp. 33–36. ISSN: 10225528. DOI: 10.1007/s11244-007-0146-6.

[102] Feng Gao et al. "Understanding ammonia selective catalytic reduction kinetics over Cu/SSZ-13 from motion of the Cu ions". In: *Journal of Catalysis* 319 (2014), pp. 1–14. ISSN: 00219517. DOI: 10.1016/j.jcat.2014.08.010.

[103] Kenneth A. Kobe and Paul D. Hosman. "Catalytic Oxidation of Ammonia to Nitrous Oxide". In: *Industrial & Engineering Chemistry* 40.3 (1948), pp. 397–399. ISSN: 0019-7866. DOI: 10.1021/ie50459a008.

[104] Yongjin Jung et al. "NOx and N2O emissions over a Urea-SCR system containing both V2O5-WO3/TiO2 and Cu-zeolite catalysts in a diesel engine". In: *Psychological Bulletin* 126.1 (2019), p. 21. DOI: 10.1016/j.cej.2017.06.020.

[105] Shane A Bates. "Spectroscopic and Kinetic Study of Copper-Exchanged Zeolites for the Selective Catalytic Reduction of NOx With Ammonia". PhD thesis. Purdue, 2013. URL: http://docs.lib.purdue.edu/open{_}access{_}dissertations.

[106] Feng Gao et al. "Iron Loading Effects in Fe/SSZ-13 NH3-SCR Catalysts: Nature of the Fe Ions and Structure-Function Relationships". In: *ACS Catalysis* 6.5 (2016), pp. 2939–2954. ISSN: 21555435. DOI: 10.1021/acscatal.6b00647.

[107] Sandro Brandenberger et al. "The determination of the activities of different iron species in Fe-ZSM-5 for SCR of NO by NH3". In: *Applied Catalysis B: Environmental* 95.3-4 (2010), pp. 348–357. ISSN: 09263373. DOI: 10.1016/j.apcatb.2010.01.013.

[108] Feng Gao et al. "Fe/SSZ-13 as an NH3-SCR catalyst: A reaction kinetics and FTIR/Mössbauer spectroscopic study". In: *Applied Catalysis B: Environmental* 164 (2015), pp. 407–419. ISSN: 09263373. DOI: 10.1016/j.apcatb.2014.09.031.

[109] C Perego. "Experimental methods in catalytic kinetics". In: *Catalysis Today* 52 (1999), pp. 133–145. ISSN: 09205861. DOI: 10.1016/s0920-5861(99)00071-1.

[110] Rosemarie Szostak. *Molecular Sieves: Principles Of Synthesis And Identification*. New York: Springer Science+Business Media, 1989. ISBN: 978-0-7514-0480-7.

[111] Stephen Wilson and Paul Barger. "The characteristics of SAPO-34 which influence the conversion of methanol to light olefins". In: *Microporous and Mesoporous Materials* 29.1-2 (1999), pp. 117–126. ISSN: 13871811. DOI: 10.1016/S1387-1811(98)00325-4.

[112] Can Niu et al. "High hydrothermal stability of Cu-SAPO-34 catalysts for the NH3-SCR of NOx". In: *Chemical Engineering Journal* 294.x (2016), pp. 254–263. ISSN: 13858947. DOI: 10.1016/j.cej.2016.02.086.

[113] Saurabh Y. Joshi et al. "Combined experimental and kinetic modeling study of the bi-modal NOx conversion profile on commercial Cu-SAPO-34 catalyst under standard SCR conditions". In: *Applied Catalysis B: Environmental* 165 (2015), pp. 27–35. ISSN: 09263373. DOI: 10.1016/j.apcatb.2014.09.060.

[114] Feng Gao et al. "Current Understanding of Cu-Exchanged Chabazite Molecular Sieves for Use as Commercial Diesel Engine DeNOx Catalysts". In: *Topics in Catalysis* 56.15-17 (2013), pp. 1441–1459. ISSN: 1022-5528. DOI: 10.1007/s11244-013-0145-8.

[115] R Vomscheid, M J Peltre, and D Barthomeup. "The Role of the Template in Directing the Si Distribution in SAPO Zeolites". In: *J. Phys. Chem.* 98 (1994), pp. 9614–9618.

[116] Lei Xu et al. "Synthesis of SAPO-34 with only Si(4Al) species: Effect of Si contents on Si incorporation mechanism and Si coordination environment of SAPO-34". In: *Microporous and Mesoporous Materials* 115.3 (2008), pp. 332–337. ISSN: 13871811. DOI: 10.1016/j.micromeso.2008.02.001.

[117] Liping Ye et al. "Effect of different TEAOH/DEA combinations on SAPO-34's synthesis and catalytic performance". In: *Journal of Porous Materials* 18.2 (2011), pp. 225–232. ISSN: 13802224. DOI: 10.1007/s10934-010-9374-4.

[118] Tie Yu et al. "The effect of various templates on the NH3-SCR activities over Cu/SAPO-34 catalysts". In: *Chemical Engineering Journal* 243 (2014), pp. 159–168. ISSN: 13858947. DOI: 10.1016/j.cej.2014.01.008.

[119] Hussein Bahrami, Jafar Towfighi Darian, and Mehdi Sedighi. "Simultaneous effects of water, TEAOH and morpholine on SAPO-34 synthesis and its performance in MTO process". In: *Microporous and Mesoporous Materials* 261.October 2017 (2018), pp. 111–118. ISSN: 13871811. DOI: 10.1016/j.micromeso.2017.11.011.

[120] M. Popova, Ch Minchev, and V. Kanazirev. "Methanol conversion to light alkenes over SAPO-34 molecular sieves synthesized using various sources of silicon and aluminium". In: *Applied Catalysis A: General* 169.2 (1998), pp. 227–235. ISSN: 0926860X. DOI: 10.1016/S0926-860X(98)00003-9.

[121] Teresa Alvaro-Munoz, Carlos Marquez-Alvarez, and Enrique Sastre. "Use of different templates on SAPO-34 synthesis: Effect on the acidity and catalytic activity in the MTO reaction". In: *Catalysis Today* 179.1 (2012), pp. 27–34. ISSN: 09205861. DOI: 10.1016/j.cattod.2011.07.038.

[122] Emil Dumitriu et al. "Synthesis, characterization and catalytic activity of SAPO-34 obtained with piperidine as ternplating agent". In: *Microporous Materials* 10.96 (1997), pp. 1–12. ISSN: 09276513. DOI: 10.1016/S0927-6513(96)00107-1.

[123] Guangyu Liu et al. "Synthesis of SAPO-34 templated by diethylamine: Crystallization process and Si distribution in the crystals". In: *Microporous and Mesoporous Materials* 114.1-3 (2008), pp. 416–423. ISSN: 13871811. DOI: 10.1016/j.micromeso.2008.01.030.

[124] Huiru Zhao et al. "Charge compensation dominates the distribution of silica in SAPO-34". In: *Cuihua Xuebao/Chinese Journal of Catalysis* 37.2 (2016), pp. 227–233. ISSN: 02539837. DOI: 10.1016/S1872-2067(15)61025-7.

[125] Ali Izadbakhsh et al. "Effect of SAPO-34's composition on its physico-chemical properties and deactivation in MTO process". In: *Applied Catalysis A: General* 364.1-2 (2009), pp. 48–56. ISSN: 0926860X. DOI: 10.1016/j.apcata.2009.05.022.

[126] German Sastre et al. "Modeling of silicon substitution in SAPO-5 and SAPO-34 molecular sieves". In: *Journal of Physical Chemistry B* 101.27 (1997), pp. 5249–5262. ISSN: 10895647. DOI: 10.1021/jp963736k.

[127] Peng Tian et al. *SAPO-34 molecular sieve and method for preparing the same.* 2017. arXiv: arXiv:1208.5721.

[128] Jun Wang et al. "The influence of silicon on the catalytic properties of Cu/SAPO-34 for NOx reduction by ammonia-SCR". In: *Applied Catalysis B: Environmental* 127.x (2012), pp. 137–147. ISSN: 09263373. DOI: 10.1016/j.apcatb.2012.08.016.

[129] Qiming Sun, Zaiku Xie, and Jihong Yu. "The state-of-the-art synthetic strategies for SAPO-34 zeolite catalysts in methanol-to-olefin conversion". In: *National Science Review* 5.4 (2018), pp. 542–558. ISSN: 2053714X. DOI: 10.1093/nsr/nwx103.

[130] R. Vomscheid et al. "Reversible modification of the Si environment in template-free SAPO-34 structure upon hydration-dehydration cycles below ca. 400 K". In: *Journal of the Chemical Society, Chemical Communications* 6 (1993), p. 544. ISSN: 0022-4936. DOI: 10.1039/c39930000544.

[131] Torstein Fjermestad, Stian Svelle, and Ole Swang. "Mechanism of Si island formation in SAPO-34". In: *Journal of Physical Chemistry C* 119.4 (2015), pp. 2086–2095. ISSN: 19327455. DOI: 10.1021/jp510845z.

[132] Jungwon Woo et al. "Effect of various structure directing agents (SDAs) on low-temperature deactivation of Cu/SAPO-34 during NH3-SCR reaction". In: *Catalysis Science and Technology* 8.12 (2018), pp. 3090–3106. ISSN: 20444761. DOI: 10.1039/c8cy00147b.

[133] A.M. Prakash and S. Unnikrisnan. "Synthesis of SAPO-34: high silicon incorporation in the presence of morpholine as template". In: *Journal of the Chemical Society, Faraday Transactions* 90.15 (1994), pp. 2291 –2296. ISSN: 1098-6596.

[134] Carolina Petitto and Gerard Delahay. "Selective catalytic reduction of NOx by NH3 on Cu-SAPO-34 catalysts: Influence of silicium content on the activity of calcined and hydrotreated samples". In: *Chemical Engineering Journal* 264.x (2015), pp. 404–410. ISSN: 13858947. DOI: 10.1016/j.cej.2014.11.111. URL: http://dx.doi.org/10.1016/j.cej.2014.11.111.